Die approbierte Originalversion dieser Dissertation ist in der Hauptbibliothek der Technischen Universität Wien aufgestellt und zugänglich.
http://www.ub.tuwien.ac.at

The approved original version of this thesis is available at the main library of the Vienna University of Technology.
http://www.ub.tuwien.ac.at/eng

TECHNISCHE
UNIVERSITÄT
WIEN
Vienna University of Technology

Unterschrift der Begutachter:

....

....

DISSERTATION

Simulation of nanoscale electronic devices using the Schrödinger equation with open boundary conditions

ausgeführt zum Zwecke der Erlangung des akademischen Grades eines
Doktors der technischen Wissenschaften unter der Leitung von

Univ.-Prof. Dr. rer. nat. Ansgar Jüngel
E101
Institut für Analysis und Scientific Computing

eingereicht an der Technischen Universität Wien
Fakultät für Mathematik und Geoinformation

von

Dipl.-Math. Jan-Frederik Mennemann
Matrikelnummer: 0727573
Obermüllnerstraße 2c, Stiege 6, 1020 Wien

Wien, am 19. September 2013

Kurzfassung

Diese Arbeit behandelt die Simulation von Halbleiterbauteilen mit Hilfe der Schrödingergleichung beziehungsweise den Schrödinger-Poisson-Gleichungen. Einen besonderen Schwerpunkt bilden transiente Simulationen sowie offene Randbedingungen zur Beschreibung der Bauteilkontakte. Die Arbeit gliedert sich in drei Teile.

Im ersten Teil entwickeln wir eine einfache und zugleich schnelle Methode zur Lösung der zeitabhängigen Schrödingergleichung in zwei- und dreidimensionalen Wellenleitern mit offenen Randbedingungen. Als numerisches Verfahren zur Diskretisierung der Schrödingergleichung verwenden wir eine sogenannte *Time-Splitting Spektralmethode*. Die offenen Randbedingungen werden mit Hilfe künstlicher Potentiale realisiert, welche einen negativen Imaginärteil besitzen und dafür sorgen, dass auslaufende Elektronenwellen absorbiert werden. Weil sich Wellen niedriger Energie nur mit Hilfe ausgedehnter künstlicher Potentiale absorbieren lassen, ist ein sehr großes Simulationsgebiet erforderlich. Andererseits müssen pro Zeitschritt effektiv nur zwei schnelle Fourier-Transformationen ausgewertet werden, weshalb der numerische Aufwand insgesamt vergleichsweise klein bleibt. Um die Möglichkeiten der Methode zu demonstrieren, simulieren wir das zeitliche Verhalten der Wellenfunktion in einem dreidimensionalen Quantenwellenleiter.

Im zweiten Teil der Dissertation modellieren wir die Dynamik einer Resonanztunneldiode (RTD) mit Hilfe der Schrödinger-Poisson-Gleichungen. Zur Diskretisierung der zeitabhängigen Schrödingergleichungen wird das Crank-Nicolson-Verfahren mit diskreten transparenten Randbedingungen verwendet. Die Lösungen werden auf selbstkonsistente Weise mit der Poisson-Gleichung gekoppelt. Insbesondere wollen wir das zeitliche Verhalten einer RTD in einer Oszillatorschaltung studieren. Dazu müssen zahlreiche aus der Literatur bekannte Techniken verbessert oder weiterentwickelt werden. In bisherigen Simulationen wurden die Schrödinger-Poisson-Gleichungen in leicht abgewandelter Form betrachtet um numerische Konvergenzprobleme zu umgehen. Wir hingegen zeigen, dass es möglich ist, numerische Lösungen für die Gleichungen in ihrer ursprünglichen Form zu berechnen. Außerdem zeigen wir, wie sich numerische Störungen in der Stromdichte beseitigen lassen. Dazu müssen sowohl die Randbedingungen der stationären Schrödingergleichungen, deren Lösungen die Anfangszustände beschreiben, als auch die Randbedingungen der zeitabhängigen Schrödingergleichungen so diskretisiert werden, dass keine unphysikalischen Oszillationen auftreten. Da der numerische Aufwand zur Auswertung diskreter transparenter Randbedinungen für die zeitabhängige Schrödingergleichung quadratisch mit der Gesamtzahl der Zeitschritte wächst, sind Simulationen über größere Zeitskalen extrem kostspielig. Dieses Problem lösen wir mit einer erst kürzlich vorgestellten Approximation, die sehr viel schneller ausgewertet werden kann und nebenbei den Speicherverbrauch erheblich reduziert.

Im dritten Teil untersuchen wir, inwieweit sich sogenannte *Perfectly Matched Layers* (PML) eignen, um offene Randbedingungen in stationären und transienten Bauteilsimulationen zu realisieren. In einer Reihe numerischer Experimente vergleichen wir PML mit diskreten transparenten Randbedingungen. Anders als imaginäre Potentiale sind PML in der Lage Elektronenwellen von extrem kleiner, mittlerer und sehr großer Energie gleichzeitig zu absorbieren. Im Vergleich zu diskreten transparenten Randbedingungen besteht ein großer Vorteil darin, dass die Wellenfunktion in den Kontakten eines Quantenwellenleiters nicht in transversale Eigenzustände zerlegt werden muss. Dies erleichtert die Implementierung erheblich. Desweiteren sind PML nicht auf ein bestimmtes numerisches Schema zur Diskretisierung der Schrödingergleichung zugeschnitten. So zeigen unsere numerischen Experimente, dass das transiente Problem mit Hilfe finiter Differenzen höherer Ordnung, expliziter Zeitintegrationsmethoden und PML effizient gelöst werden kann. Schließlich verwenden wir die entwickelten Verfahren zur Simulations des *Aharonov-Bohm Effekts* in einem ringförmigen Quantenwellenleiter.

Contents

Kurzfassung **iii**

1 Introduction **1**
- 1.1 Physical models for nanoscale electronic device simulations 1
- 1.2 Open boundary conditions for the stationary and transient Schrödinger equation 2
- 1.3 Outline of the thesis 3
- 1.4 Declaration of authorship 8

2 Simulation of quantum waveguide devices using a time-splitting spectral method **9**
- 2.1 Numerical scheme 9
  - 2.1.1 Numerical discretization 9
  - 2.1.2 Absorbing boundary conditions 11
  - 2.1.3 Injection of plane waves 12
- 2.2 Numerical simulations 15
  - 2.2.1 Numerical experiments in one space dimension 15
  - 2.2.2 Simulation of two-dimensional quantum waveguide devices 17
  - 2.2.3 Simulation of a three-dimensional quantum interference transistor 24

3 Transient Schrödinger-Poisson simulations of a high-frequency resonant tunneling diode oscillator **29**
- 3.1 Stationary simulations 29
  - 3.1.1 Schrödinger-Poisson model 29
  - 3.1.2 Discrete transparent boundary conditions 31
  - 3.1.3 Solution of the Schrödinger-Poisson system 33
- 3.2 Transient simulations 37
  - 3.2.1 Inhomogeneous discrete transparent boundary conditions 37
  - 3.2.2 Fast evaluation of the discrete convolution terms 42
  - 3.2.3 The complete transient algorithm 44
  - 3.2.4 Discretization parameters 44

3.2.5 Details of the implementation 46
3.3 Numerical experiments 46
3.3.1 First experiment: Constant applied voltage 46
3.3.2 Second experiment: Time-dependent applied voltage 47
3.3.3 Third experiment: Convergence in Λ 53
3.4 Circuit simulations 53

4 Perfectly Matched Layers versus discrete transparent boundary conditions in quantum device simulations 59
4.1 One-dimensional simulations 59
4.1.1 Scattering states 59
4.1.2 Wave packets 69
4.1.3 Time-dependent incoming waves 73
4.1.4 Transient scattering states 75
4.2 Quantum waveguide device simulations 78
4.2.1 Scattering states in quantum waveguides 78
4.2.2 Transient scattering states in quantum waveguides 89
4.2.3 Details of the implementation 94
4.3 The Aharonov-Bohm effect 95

Bibliography 103

Acknowledgement

Curriculum vitae

Chapter 1

Introduction

This thesis is devoted to Schrödinger and Schrödinger-Poisson simulations of nanoscale electronic devices in the stationary and transient regime. The main focus is on different ways to implement open boundary conditions modeling the device contacts. We investigate several numerical methods to solve the Schrödinger equation on unbounded domains. Our simulations include simple numerical experiments, but also advanced quantum transport calculations utilizing thousands of wave functions coupled self-consistently to the Poisson equation.

1.1 Physical models for nanoscale electronic device simulations

There is a variety of physical models used to describe nanoscale electronic devices. The most prominent models rely on the non-equilibrium Green's function theory [79, 27, 74, 78], the Schrödinger equation [24, 54, 67], the Wigner function [19, 51, 69, 30, 76] or quantum hydrodynamic formulations [42, 35, 47]. Although the open boundary Schrödinger and non-equilibrium Green's function approaches can be considered to be formally equivalent, their numerical treatment is different [67]. Moreover, Schrödinger models are restricted to purely ballistic transport of electrons and holes [10], whereas inelastic scattering processes like electron-phonon interactions can be easily included in the non-equilibrium Green's function method [27, 65]. Scattering effects can also be included in the Wigner-function formalism. However, since the Wigner equation is formulated in phase-space its numerical solution is rather expensive. Fluid-type models represent a convenient alternative which is computationally less intensive and therefore used frequently [10].

In this thesis, the electron transport is modeled by the stationary and time-dependent Schrödinger equation. In more realistic simulations we consider the stationary and time-dependent system of Schrödinger-Poisson equations. In that case, the electrostatic interaction between the electrons in the semiconductor is taken into account at the Hartree level. Furthermore, the energy of the electrons is distributed according to the Fermi-Dirac statistics. Hence, one needs to solve a large number of linear Schrödinger equations, which are coupled self-consistently to the Poisson equation. The main difficulty of that approach is to prescribe appropriate open boundary conditions at the interfaces between the leads and the active domain of the device.

1.2 Open boundary conditions for the stationary and transient Schrödinger equation

In the literature, there exist several formulations of open boundary conditions for the stationary and transient Schrödinger equation. Open boundary condition are called transparent, if they yield solutions which coincide exactly with the solutions of the whole-space problem. In the context of stationary quantum device simulations we are interested in solutions to the stationary Schrödinger equation subject to the boundary condition that the beam of electrons entering the active device region is described by a plane wave. Additionally, the potential energy in the leads is assumed to be constant. Under these assumptions transparent boundary conditions (TBC) in one space dimension can be derived easily [6].

In two- and three-dimensional simulations the wave function in the leads can be decomposed into transversal waveguide eigenstates and hence it is possible to reduce the problem to the one-dimensional case. This idea is employed in [54] for a linear finite element approximation of the stationary Schrödinger equation and is called the quantum transmitting boundary method. However, its implementation is rather complex and to the best of our knowledge there are no implementations employing higher order numerical approximations.

In contrast, absorbing boundary conditions can be implemented easily with the help of a simple imaginary potential. To this end, the computational domain is extended by an artificial layer with the intention to absorb the wave function before it reaches the outer boundaries of the enlarged domain [37, 53, 56, 60]. Criteria for selecting the optimal height and width of imaginary potentials are investigated in [60]. It turns out that for low-energy waves, the computational domain has to be large compared to the physical domain, thus increasing the computational costs.

Another possibility is to employ Perfectly Matched Layers (PML) which were first developed for the Maxwell equations [17]. The method has been applied to the Schrödinger equation in [80, 24, 61] and can be interpreted as the result of a complex coordinate transformation. As a consequence one needs to solve a modified version of the original equation which is defined on an enlarged computational domain. Theoretically, PML yield solutions which are perfectly reflection-free at the boundaries. However, in a practical implementation PML introduce a numerical error which decreases exponentially with the thickness of the layers [2].

TBC for the time-dependent Schrödinger equation are nonlocal in time and therefore the realization of open boundaries in transient device simulations is much more involved. Inadequate discretizations often introduce numerical reflections at the boundaries and destroy the stability of the final numerical scheme [31]. These problems can be overcome if the boundary conditions are derived on the discrete level of the numerical method employed to approximate the Schrödinger equation. Such discrete TBC have been developed for the Crank-Nicolson scheme which is one of the most frequently used numerical methods to solve the transient Schrödinger equation [5, 6]. The resulting numerical scheme is unconditionally stable and avoids any physically incorrect reflections from the boundaries. Since discrete TBC include the discrete convolution of the wave function with a given kernel, simulations involving many time steps may become very expensive. This problem can be solved if the kernel is approximated by a finite sum of exponentials which allows to accelerate the evaluation of the boundary conditions significantly [8].

Both imaginary potentials and PML can also be applied in transient device simulations. In the transient case they need to absorb incoming waves of very low to very high energies simultaneously which is why the thickness of the layers needs to be large (PML) or even very large (imaginary potentials).

In the literature, many other approaches are known such as, for example, the time-dependent phase-space filter method [72], where periodically in time, the wave function is decomposed into a family of coherent states and those states which are outgoing are deleted. However, like for imaginary potentials, it is not easy to treat low-energy wave functions. An explicit local boundary condition which involves 16 neighboring grid points and achieves a good balance between accuracy and numerical costs was recently proposed in [63]. For further information on TBC, we refer to [2, 80, 63] and the references therein.

1.3 Outline of the thesis

Chapter 2

Quantum waveguide devices are the subject of Chapter 2. In these devices the electrons are confined to small channels or waveguides and the electrical properties depend on quantum interference effects which can be controlled by voltages applied at the gate contacts. Quantum waveguide devices may be used as nanoscale electronic switches, quantum interference transistors, multiplexers etc. [22, 73, 77]. At sufficiently low temperatures scattering processes are mostly eliminated and the inelastic mean free path of the electrons is larger than the characteristic length scales of the devices [73, 77]. As a consequence, the electron transport is in the ballistic regime.

Our model is based on the two- and three-dimensional time-dependent Schrödinger equation with open boundary conditions. For the discretization of the Schrödinger equation we employ a time-splitting spectral method. More precisely, the

Schrödinger equation is split into the free Schrödinger equation and an ordinary differential equation for the electric potential. The latter equation can be solved explicitly, whereas the former one is approximated by a spectral method [11, 64]. There are several time-splitting strategies such as the Trotter and Strang splitting; see [44] for the corresponding error estimates. These methods are unconditionally stable, mass conservative, and gauge invariant [11]. Another advantage of the spectral method is that the discrete set of equations can be solved very efficiently by using the Fast Fourier Transform. In fact, the complexity of the complete algorithm for one time step is of the order $\mathcal{O}(M \log M)$, where $M = M_1 \cdots M_d$ and M_j is the number of grid points in the j-th direction.

Our aim is to develop a fast, easy-to-implement numerical scheme for the open Schrödinger problem in up to three space dimensions. Therefore, the open boundary conditions are realized via simple imaginary potentials. In order to be able to absorb even low-energy waves the absorbing layers need to be large which increases the computational costs. However, due to the low complexity of the time-splitting spectral scheme, the overall complexity is still low, and three-dimensional simulations are possible on desktop computers within a few hours of computing time.

There are only a few results in the literature on transient quantum device simulations in three space dimensions. In fact, most of the three-dimensional numerical simulations concern the stationary Schrödinger equation, see e.g. [24, 67, 70]. Transient simulations are typically performed in one or two space dimensions only, see e.g. [9, 72] for Schrödinger simulations and [59] for Wigner simulations. In [40], the time-dependent Schrödinger equation is numerically solved in three space dimensions, but no devices have been simulated. In this thesis, we present a dynamical simulation of a three-dimensional quantum interference transistor.

Chapter 3

Chapter 3 is devoted to stationary and transient simulations of a resonant tunneling diode which has a variety of applications as high-frequency and low-consumption oscillator or switch. The resonant tunneling structure is usually treated as an open quantum system with two large reservoirs and an active region containing a double-barrier heterostructure. There exist several approaches in the literature to model a resonant tunneling diode. The simplest approach is to replace the diode by an equivalent circuit containing nonlinear current-voltage characteristics [52]. Another approximation is to employ the Wannier envelope function development [55]. Other physics-based approaches rely on the Wigner equation [19, 51], the nonequilibrium Green's function theory [26, 50], quantum hydrodynamic models [35, 42, 47], and the Schrödinger equation [16, 20, 66, 75]. In this thesis, we adopt the latter approach and simulate the time-dependent behavior of a resonant tunneling diode using the system of Schrödinger-Poisson equations in one space dimension. Accordingly, the electrons are assumed to be in a mixed state with Fermi-Dirac statistics and the electrostatic interaction is taken into account at the Hartree level. Each state is determined as the solution of the time-dependent Schrödinger equation with inhomogeneous transparent boundary conditions. The Schrödinger equations are discretized by the Crank-Nicolson finite-difference scheme and coupled self-consistently to the Poisson equation. Our aim is to realize a long-time simulation of a high-frequency oscillator circuit containing a resonant tunneling diode. For this, we need to adapt and improve several existing numerical techniques from, e.g., [2, 8, 66].

The first improvement concerns the model itself. In the literature [15, 66], a modified description of the potential energy is used to overcome problems related to the numerical convergence in the stationary calculations. Physically interpreted, this modification introduces artificial surface charge densities at the junction interfaces of the tunneling diode. We show how the original problem can be solved which is an improvement compared to the simulations in [66], where the modified model is also employed for the time-dependent case.

The second improvement concerns the discretization of the open boundary conditions in the stationary problem. We discretize the stationary open boundary conditions in such a way that their discrete version is compatible with the underlying finite difference discretization, as proposed in [6]. Thereby, we eliminate any spurious oscillations which would otherwise propagate in the subsequent transient simulations.

A similar problem is related to the discretization of inhomogeneous transparent boundary conditions used to solve the time-dependent Schrödinger equations of the transient problem. Inhomogeneous transparent boundary conditions are transparent boundary conditions which at the same time describe a continuously incoming beam of electrons. The potentials in the leads of the resonant tunneling diode are constant in space but may vary over time and therefore the boundary conditions become even more complicated. It is well known that, using a suitable gauge change, one can get rid of the transient potentials [3]. Corresponding inhomogeneous discrete transparent boundary conditions can be found in [15]. However, in numerical simulations we observed that these boundary conditions may lead to physically incorrect distortions in the conduction current density. The reason is that the considered discretization of the gauge change is not compatible with the underlying finite-difference scheme. Therefore, we suggest a new discretization which is derived from the Crank-Nicolson time integration method. Our approach completely removes these numerical artifacts, and we show that the total current density is perfectly conserved. We stress the fact that our discretization is completely consistent with the underlying Crank-Nicolson scheme inheriting its conservation and stability properties.

Since transparent boundary conditions for the time-dependent Schrödinger equation are of memory type [6, 12], their numerical implementation requires to store and to use the boundary data for all the past history. For this reason, simulations involving longer time scales are extremely costly which explains why simulations in the literature [15, 20, 66] have been restricted to some picoseconds only. However, if the discrete convolution kernel is approximated by a finite sum of exponentials, the evaluation of the boundary conditions can be accelerated significantly. This rather new numerical technique has been presented in [8] and employed in [7] on circular domains. Here it is used for the first time in an advanced quantum transport calculation.

Another challenge results from the large number of wave functions which need to be propagated, accounting for the energy distribution of the incoming electrons. Therefore we develop a parallel version of our solver utilizing multiple cores on shared memory processors.

The improvements mentioned above enable us to present simulations of the Schrödinger-Poisson system for large times up to 100 ps (ps = picosecond) with reasonable computational effort (compared to 5 ps in [66], 6 ps in [20], and 8 ps in [15]). Using the numerical results we identify plasma oscillations and estimate the life time of the resonant state. Moreover, we present for the first time simulations of a high-frequency oscillator circuit containing a resonant tunneling diode, based on a full Schrödinger-Poisson solver with transparent boundary conditions. Simplified simulations of tunneling diode oscillators have been considered in [52, 55, 58]. However, our approach is expected to be more accurate and furthermore it allows us to observe the complex time-dependent behavior of quantities like the electron density in an unprecedented way.

Chapter 4

In Chapter 4 we compare discrete transparent boundary conditions (DTBC) and the technique of Perfectly Matched Layers (PML), which is another approach to implement open boundary conditions in quantum device simulations. Our considerations are motivated by an article on different numerical techniques to solve the time-dependent Schrödinger equation on unbounded domains [2]. Numerical examples presented in the final section of [2] suggest that PML represent an interesting alternative to more elaborate methods like DTBC. However, the examples are restricted to the simulation of wave packets in one space dimension. In device simulations the initial wave function is a scattering state, i.e., a solution to the stationary Schrödinger equation subject to the boundary condition that the incoming beam of electrons is represented by a plane wave. When the transient simulation is started, the external potential may change over time and hence the scattering state starts to evolve in time too. A transient Schrödinger-Poisson solver using thousands of transient scattering states is the subject of Chapter 3. In this chapter we concentrate on the key tasks of solving the stationary and time-dependent Schrödinger equation with open boundary conditions.

PML have been used to solve the linear and nonlinear time-dependent Schrödinger equation on unbounded domains but the simulations include wave packets only [80]. The three-dimensional stationary scattering state problem is considered in [24] using PML and the spectral element method. In this thesis, we show how to apply PML in stationary and, especially, in transient scattering state calculations.

To this end, we employ relatively large PML which are capable of absorbing incoming waves of extremely low to very high energies simultaneously. However, we would like to note that the width and the shape of the PML are chosen manually and thus leave room for further improvements [61].

Since the open boundary problem in two- and three-dimensional devices can be reduced to the one-dimensional case, we consider one-dimensional simulations first. Besides of our explanations on the numerical methods using PML we recall the methods which are based on DTBC. Moreover, we need to introduce notations and formulas needed in the subsequent sections. The numerical solutions of both methods are compared in a series of simulations including scattering states, wave packets and transient scattering states.

We then turn our attention to two-dimensional quantum waveguide devices. The stationary scattering state problem has been solved in [54] using the quantum transmitting boundary method. The transient case is considered in Chapter 2 where we employ a time-splitting spectral method in combination with imaginary potentials. Since imaginary potentials need to be adapted to the energies of the incoming electron waves this method could not be applied in an universal time-dependent Schrödinger-Poisson solver. DTBC for quantum waveguide devices based on the Crank-Nicolson scheme have been developed in [9, 68]. However, transient scattering states are not considered and the cross sections of the waveguides need to be infinite square well potentials. In this thesis, we show how to remove these limitations. Our explanations are based on the example of a ring-shaped two-terminal quantum waveguide device but our approach could be easily generalized to more complicated multi-terminal devices including even time-dependent applied voltages at the device contacts. Admittedly, the numerical implementation of DTBC for a transient scattering state problem is demanding and involves a lot of bookkeeping. Moreover, our presentation is limited to a 2nd-order finite difference discretization of the spatial derivatives. For that reason it is interesting to investigate whether PML could be used as an alternative.

The implementation of open boundary conditions in quantum waveguide device simulations using PML works analogously to the one-dimensional case. Contrary to DTBC, a decomposition into cross-sectional waveguide eigenstates is not required. Nonetheless, our numerical experiments demonstrate that the numerical error which results from the PML is of the same order as the error which results from the approximation of the Schrödinger equation itself. In contrast to DTBC which are tailored specifically to numerical methods like the 2nd-order Crank-Nicolson scheme, PML can be applied in a more flexible way. As an example, we employ 2nd-, 4th- and 6th-order finite difference formulas to approximate the spatial derivatives. For the time-integration we use the Crank-Nicolson method or, alternatively, the classical Runge-Kutta method.

Runge-Kutta methods are rarely used in the context of quantum mechanics and especially in case of the Schrödinger equation. This is probably because the resulting spatio-temporal discretizations are only conditionally stable. Furthermore, the mass of the particles is not conserved exactly. However, our numerical results suggest that these issues might be overestimated. The combination of the classical Runge-Kutta method, higher-order spatial discretizations and PML appears to be a promising solution for transient quantum device simulations.

Finally, we apply the above mentioned methods in a simulation of the Aharonov-Bohm effect which is considered to be one of the cornerstones of modern quantum physics [1, 13]. Simulations of ring quantum interference transistors imitating this effect via electrostatic potentials are shown in [41]. In this thesis we present stationary and transient simulations of the original Aharonov-Bohm effect utilizing a magnetic field. As far as we know, these are the first transient scattering state simulations of this well-known physical phenomenon.

1.4 Declaration of authorship

Chapter 2 and Chapter 3 have been published in [48] and [57], respectively. Needless to say that this work is based on many discussions and continuous exchange of ideas with my co-authors Ansgar Jüngel and Hans Kosina. All numerical simulations including discretizations, implementations, figures and artwork were solely created by myself. Moreover, I am the main author of the above mentioned publications. The publication of Chapter 4 is planned for the future.

Chapter 2

Simulation of quantum waveguide devices using a time-splitting spectral method

Chapter 2 is organized as follows. In Section 2.1, we detail the time-splitting spectral method, the choice of the negative imaginary potential, and the injection of a continuously incoming mono-energetic plane wave pulse. Section 2.2 is devoted to numerical examples. First, we perform a numerical test in one space dimension to compute numerical convergence rates. Furthermore, in two space dimensions, the stationary behavior in a T-stub interference transistor and a single-branch coupler are simulated. The numerical results are compared with those from [22]. Finally, we present the dynamical behavior of a three-dimensional T-stub waveguide device.

2.1 Numerical scheme

We consider the time-dependent Schrödinger equation for the wave function ψ:

$$i\hbar\partial_t\psi = -\frac{\hbar^2}{2m^*}\Delta\psi + V(x)\psi, \quad \text{in } \Omega,\ t>0, \quad \psi(\cdot,0)=\psi_0 \quad \text{in } \Omega, \tag{2.1}$$

where $\Omega \subset \mathbb{R}^d$ ($d \leq 3$) is a bounded domain. The physical constants are the reduced Planck constant $\hbar$ and the effective mass m^*, and V denotes the external confinement potential. The device domain is generally included in the computational domain Ω which is taken as a rectangle or cuboid in the simulations. Since we want to employ a time-splitting spectral method (TSSM) we prescribe periodic boundary conditions on Ω.

2.1.1 Numerical discretization

Let $\Omega = \Pi_{j=1}^{3}(a_j, b_j)$ be a cuboid. We introduce the spatial grid $(x_\alpha) = (x_1^{(\alpha_1)}, x_2^{(\alpha_2)}, x_3^{(\alpha_3)})$, where $x_j^{(\alpha_j)} = a_j + \alpha_j \triangle x_j$, $\triangle x_j = (b_j - a_j)/M_j$, $\alpha_j \in \{0, \ldots, M_j - 1\}$, and M_j

are even integers ($j = 1, 2, 3$). The time steps are given by $t_n = n\triangle t$, where $\triangle t > 0$ and $n \in \mathbb{N}$. We denote by ψ_α^n the numerical approximation of $\psi(x_\alpha, t_n)$. In this notation, $\alpha = (\alpha_1, \alpha_2, \alpha_3)$ denotes a multiindex with $\alpha \in I := \Pi_{j=1}^3\{0, \dots, M_j - 1\}$.

The solution to the Schrödinger equation (2.1) at time t_{n+1} with initial datum $\psi(t_n)$ can be formally written as $\psi(t_{n+1}) = e^{-i(A+B)\triangle t}\psi(t_n)$, where $A = -(\hbar/2m^*)\Delta$ and $B = V(x)/\hbar$, and $\psi(t)$ denotes the function $\psi(\cdot, t)$. The Trotter time-splitting is based on the approximation

$$\psi(t_{n+1}) \approx e^{-iB\triangle t}e^{-iA\triangle t}\psi(t_n),$$

i.e., first the free Schrödinger equation is solved for one time step,

$$i\hbar\partial_t\psi_1 = -\frac{\hbar^2}{2m^*}\Delta\psi_1, \quad \psi_1(0) = \psi(t_n), \quad t > 0, \tag{2.2}$$

followed by solving the ordinary differential equation

$$i\hbar\partial_t\psi_2 = V(x)\psi_2, \quad \psi_2(0) = \psi_1(\triangle t), \quad t > 0, \tag{2.3}$$

for another time step. Then $\psi_2(\triangle t)$ is an approximation of $\psi(t_{n+1})$.

An alternative time-splitting is the Strang splitting

$$\psi(t_{n+1}) \approx e^{-iB\triangle t/2}e^{-iA\triangle t}e^{-iB\triangle t/2}\psi(t_n).$$

Convergence of this approximation follows from the Trotter product formula, and error estimates have been derived in [11, 44]. Equation (2.2) will be discretized in space by the spectral method and integrated in time exactly. Then (2.3) is solved exactly. The method is given as follows. Let the Fourier coefficients of ψ_α^n be given by

$$\widehat{\psi}_k^n = \sum_{\alpha\in I}\psi_\alpha^n e^{-i\mu_k\cdot(x_\alpha - a)}, \quad \mu_k = (\mu_{k,1}, \mu_{k,2}, \mu_{k,3}), \quad \mu_{k,j} = \frac{2\pi k_j}{b_j - a_j},$$

where $k = (k_1, k_2, k_3) \in J := \Pi_{j=1}^3\{-M_j/2, \dots, M_j/2 - 1\}$ and $a = (a_1, a_2, a_3)$. Then, given $\widehat{\psi}_k^n$ at time step t_n, the approximation at step t_{n+1} is computed from

$$\psi_\alpha^{n+1} = \frac{1}{M}e^{-iV(x_\alpha)\triangle t/\hbar}\sum_{k\in J}e^{-i\hbar|\mu_k|^2\triangle t/2m^*}\widehat{\psi}_k^n e^{i\mu_k\cdot(x_\alpha - a)},$$

where $M = M_1M_2M_3$. The initial value is given by

$$\psi_\alpha^0 = \psi(x_\alpha, 0) = \psi_0(x_\alpha), \quad \alpha \in I.$$

The Strang time splitting is similar to the Trotter time-splitting but due to the symmetric structure the order increases from one (Trotter) to two (Strang). As the computational work is nearly the same, the Strang splitting is clearly preferable (see Section 2.2.1).

In the simulations below, the above algorithm is implemented in the *Matlab* programming language. The discrete Fourier transforms are computed by the Fast Fourier Transform (FFT) based on the *FFTW* library [34]. This FFT implementation is fastest when the length of the vector is a power of two, but it is almost as fast for lengths which have small prime factors. Thus, the numbers M_1, M_2, and M_3 do not necessarily need to be powers of two. This fact is employed in our two- and three-dimensional simulations. The complexity of the time-splitting spectral method for one time step is dominated by the d-dimensional FFT and is therefore of the order $\mathcal{O}(M \log M)$.

2.1.2 Absorbing boundary conditions

Due to the periodic boundary conditions, wave packets will, after some time, wrap around the computational domain which is not intended in our applications. One way to overcome this problem is to damp the wave function before it reaches the boundary of the computational domain. To this end we employ a complex-valued potential with negative imaginary part in the vicinity of the boundaries. Other methods for designing absorbing boundary conditions have been described in Section 1.2. Our choice is based on the observation that the resulting numerical scheme can be solved very efficiently.

Negative imaginary potentials have been employed in quantum chemistry computations since several years; see, e.g. [53] and the references in [43, 56]. In [60], a linear imaginary potential has been suggested, and criteria for selecting the optimal height and width of the potential have been derived. The Saxon-Woods potential $V_{\text{abs}}(x) = -iV_0/(1+e^{\alpha(x-a)})$ has been used in [53] for studies of molecular multiphoton dissociation. Since it is generally difficult to absorb outgoing electron waves with large wavelength, some authors add a negative real potential to increase the kinetic energy of the wave function, thereby reducing its de Broglie wavelength. For instance, a complex-valued absorbing potential with power functions has been chosen in [37], whereas in [43] exponential functions have been taken.

In three dimensions, assuming that the wave packet travels in x_1-direction, we use a potential of quadratic type

$$V_{\text{abs}}(x_1,x_2,x_3) = \begin{cases} -iV_0\left(\frac{x_1-x_1^\ell}{a_1-x_1^\ell}\right)^2 & \text{if } x_1 < x_1^\ell, \\ 0 & \text{if } x_1^\ell \le x_1 < x_1^r, \\ -iV_0\left(\frac{x_1-x_1^r}{b_1-x_1^r}\right)^2 & \text{if } x_1^r \le x_1, \end{cases} \tag{2.4}$$

where x_1^ℓ and x_1^r ($x_1^\ell < x_1^r$) denote the boundaries of the device domain in the x_1-direction. As an example, the imaginary part of (2.4) is presented in Figure 2.1. In all of the following simulations, we have chosen $V_0 = 50\,\text{meV}$, $a_1 = -100\,\text{nm}$, $b_1 = 180\,\text{nm}$, $x_1^\ell = 0\,\text{nm}$, and $x_1^r = 80\,\text{nm}$. Thus, in the simulations, we replace the external potential V in the Schrödinger equation (2.1) by $V + V_{\text{abs}}$.

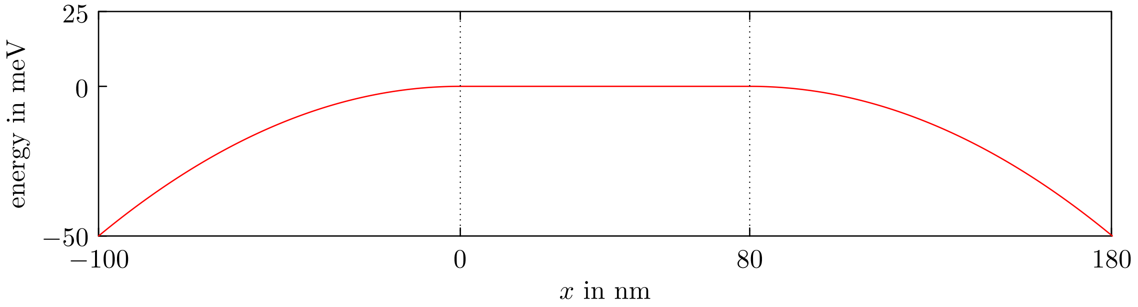

Figure 2.1: Imaginary part of the absorbing potential (2.4) with $V_0 = 50\,\mathrm{meV}$.

As a numerical example, the evolution of a free Gaussian wave packet in one space dimension under the influence of the potential (2.4) is illustrated in Figure 2.2. The wave packet (dashed line) is given by

$$\psi(x,t) = \Big(1 + i\frac{t}{\tau}\Big)^{-1/2} \exp\left[\Big(1 + i\frac{t}{\tau}\Big)^{-1} \left(-\Big(\frac{x - x_s}{2\sigma}\Big)^2 + ik(x - x_s) - i\sigma^2 k^2 \frac{t}{\tau}\right)\right],$$

where $\tau = 2m^*\sigma^2/\hbar$, $k = \sqrt{2m^*E}/\hbar$, $x_s = 40\,\mathrm{nm}$, $\sigma = 10\,\mathrm{nm}$, and $E = 16.74\,\mathrm{meV}$. The effective mass is $m^* = 0.067m_0$, where m_0 is the electron mass at rest, corresponding to GaAs. The other wave packet in Figure 2.2 (solid line) is computed from the Strang time-splitting spectral scheme, with $\triangle x = 0.25\,\mathrm{nm}$ and $\triangle t = 0.25\,\mathrm{fs}$, using the complex absorbing potential (2.4). The device domain is the interval $[0{,}80\,\mathrm{nm}]$, whereas the computational domain extends from $-100\,\mathrm{nm}$ to $180\,\mathrm{nm}$ and is more than three times larger than the physical domain. This ensures that the numerical solution (solid line) is indistinguishable from the exact solution (dashed line) in the physical domain.

The drawbacks of imaginary potentials are that they require a greatly enlarged computational domain and that they have to be fitted to the energies of the incident electron waves. However, since the numerical algorithm is dominated by the $\mathcal{O}(M \log M)$ complexity of the time-splitting spectral method, the additional computational effort due to the enlarged computational domain is less important. Moreover, the algorithm is not difficult to implement and can be parallelized easily.

2.1.3 Injection of plane waves

The incoming electrons are modeled by mono-energetic plane waves $e^{i(k\cdot x - \omega t)}$, which describe electrons with kinetic energy $E = \hbar^2|k|^2/2m^*$ and angular frequency $\omega = E/\hbar$. More precisely, we create a continuously incoming plane wave pulse spreading from the incoming lead contact to the outgoing leads. In one space dimension, we

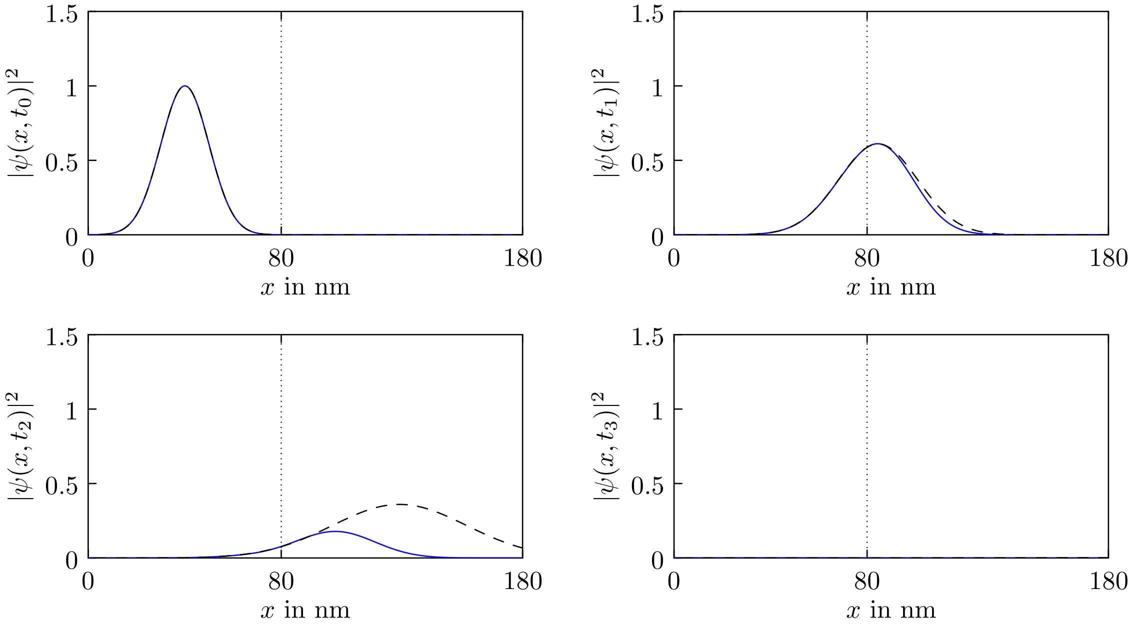

Figure 2.2: Propagation of a Gaussian wave packet under the influence of the potential (2.4) with averaged kinetic energy 16.74 meV at times $t_0 = 0\,\mathrm{fs}$, $t_1 = 150\,\mathrm{fs}$, $t_2 = 300\,\mathrm{fs}$ and $t_3 = 2\,\mathrm{ps}$. Solid line: numerical solution, dashed line: exact solution.

start with the wave function

$$\psi_j^0 = \begin{cases} \phi(x_j) & \text{if } x_j < 0, \\ e^{ikx_j}\left(\frac{1}{2} + \frac{1}{2}\cos\left(x_j\pi/\delta\right)\right) & \text{if } 0 \le x_j < \delta, \\ 0 & \text{if } \delta \le x_j, \end{cases}$$

where ϕ denotes the numerical solution of the stationary Schrödinger equation

$$-\frac{\hbar^2}{2m^\star}\frac{\partial^2}{\partial x^2}\phi(x) + V_{\text{abs}}\,\phi(x) = E\phi(x) = \frac{(\hbar k)^2}{2m^\star}\phi(x), \quad x \in [a_1, 0],$$
$$\phi(x = a_1) = 0,\ \phi(x = 0) = 1,$$

which is approximated by central finite-differences. Further, let $\tilde{\psi}_j^1$ denote the result of the time-splitting spectral method applied to the initial wave function ψ_j^0 for a single time step. We then define

$$p_j = \begin{cases} e^{-i\omega\triangle t}\psi_j^0 - \tilde{\psi}_j^1 & \text{for } x_j < 0, \\ 0 & \text{else,} \end{cases}$$

and set

$$\psi_j^1 := \tilde{\psi}_j^1 + p_j, \quad j = 0, ..., M-1$$

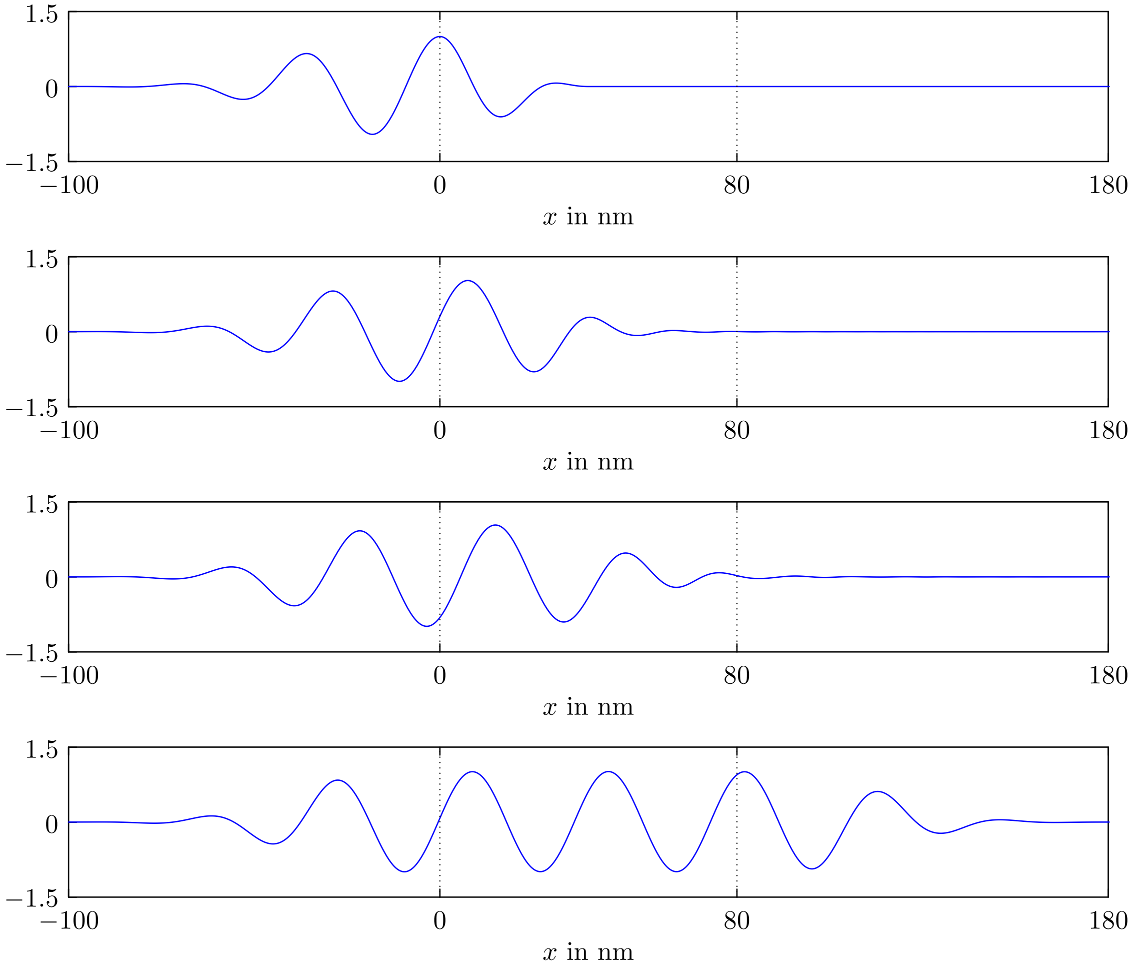

Figure 2.3: Real part of an incoming plane wave pulse at times 0 fs, 50 fs, 100 fs, and 5 ps.

for the approximation at the first time level. The next approximations are computed similarly. Subsequent to every application of the time-splitting spectral method we add the wave packet p which is then multiplied by $e^{-i\omega\triangle t}$ to adapt the phase shift of the incoming wave. This process is illustrated in Figure 2.3 for $E = 16.74\,\text{meV}$, $\delta = 40\,\text{nm}$, $\triangle x = 0.25\,\text{nm}$, and a time step size of $\triangle t = 0.25\,\text{fs}$. The real part of the incoming plane wave pulse is shown at various times. We see that the pulse spreads from the left to the right lead and finally equals a plane wave in the physical domain $[0, 80]$ nm.

In several space dimensions, we assume that the incoming pulse travels in the x_1-direction, whereas the electrons are confined in the other directions. Then the incoming plane wave pulse is the product of the one-dimensional pulse, as described above, in the x_1-direction and the solution to the stationary Schrödinger equation in the x_2-direction (and x_3-direction if $d = 3$).

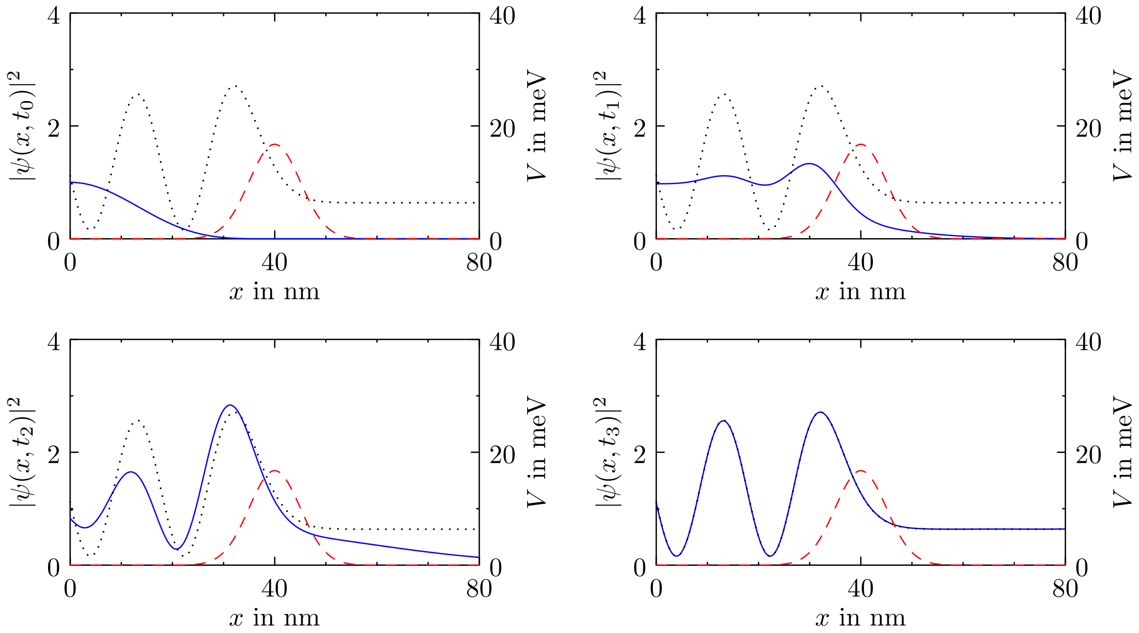

Figure 2.4: Evolution of the incoming plane wave pulse in the presence of a smooth external potential (dashed line) at times $t_0 = 0\,\mathrm{fs}$, $t_1 = 100\,\mathrm{fs}$, $t_2 = 200\,\mathrm{fs}$ and $t_3 = 5\,\mathrm{ps}$. Solid line: numerical solution computed with the spectral method. Dotted line: scattering state computed with transparent boundary conditions.

2.2 Numerical simulations

2.2.1 Numerical experiments in one space dimension

As a test of the numerical scheme described in Section 2.1, we consider the evolution of the incoming plane wave pulse in the presence of a smooth external potential

$$V(x) = V^\star\, e^{-0.02\,\left(\frac{x-x_0}{\mathrm{nm}}\right)^2}, \quad x \in [0, 80\,\mathrm{nm}],$$

placed at $x_0 = 40\,\mathrm{nm}$ (see Figure 2.4). The maximum value of the potential $V^\star$ equals the energy of the incoming plane wave $E = 16.74\,\mathrm{meV}$. The dotted line in Figure 2.4 represents the scattering state computed with stationary transparent boundary conditions (see Section 1.2) on a very fine grid with $\triangle x = 0.0025\,\mathrm{nm}$. This is taken as a reference solution for the expected scattering state. The solid line is the numerical solution of the time-splitting spectral method using $\triangle x = 0.25\,\mathrm{nm}$ and $\triangle t = 0.25\,\mathrm{fs}$. Apparently, the solution converges to the scattering state computed with transparent boundary conditions. The relative difference in the ℓ^2-norm between the particle densities at various times is shown in Figure 2.5.

Next, we present numerical convergence rates with respect to the time and space discretization parameters. With the help of a reference solution we compute the relative error in the ℓ^2-norm. The reference solution is obtained from the Crank-

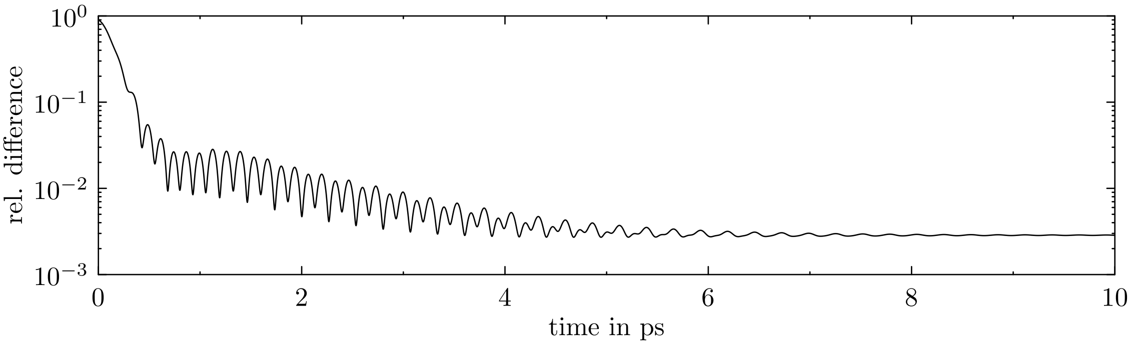

Figure 2.5: Relative difference between the spectral approximation and the solution calculated with transparent boundary conditions in the ℓ^2-norm as a function of time.

Nicolson finite-difference scheme in combination with discrete transparent boundary conditions (DTBC); see Section 1.2. More precisely, a homogeneous DTBC is used at $x = 80\,\mathrm{nm}$, whereas an inhomogeneous DTBC is used at $x = 0\,\mathrm{nm}$, modeling the incoming plane wave pulse. For further details, we refer to [6]. The numerical scheme is unconditionally stable and completely reflection-free at the boundary [8]. Taking $\triangle x = 0.0025\,\mathrm{nm}$ and $\triangle t = 0.005$ as discretization parameters, we calculate a very accurate reference solution at $t = 500\,\mathrm{fs}$ which corresponds to 100 000 time steps. Since in each time step a convolution of size n (time step number) has to be computed, this calculation is very expensive.

Now we perform the same simulation as above until $t = 500\,\mathrm{fs}$ with the time-splitting spectral method, where we use different time step sizes $\triangle t$ but a fixed spatial discretization $\triangle x = 0.025\,\mathrm{nm}$. The relative error in the ℓ^2-norm between the numerical solution and the reference solution is shown in Figure 2.6 (left). Here we distinguish between the Trotter time splitting (triangles) and the Strang time splitting (squares). Obviously, the Strang splitting is superior to the Trotter splitting. When the time step size is getting very small, both numerical schemes yield approximately the same error. This is probably due to the influence of the complex absorbing potential outside of the device domain. The convergence rate of the Trotter splitting for moderate time step sizes is approximately 1.1, which corresponds to the first-order time splitting. The convergence rate of the Strang splitting for moderate time step sizes is approximately 2.0, which corresponds to the second-order time splitting. Next, we repeat the experiment with variable spatial discretizations $\triangle x$ and a fixed time step size $\triangle t = 0.1\,\mathrm{fs}$. The relative errors are presented in Figure 2.6 (right).

We note that the convergence rate obtained in [11] for the Trotter time-splitting spectral method *without* absorbing potentials reads as follows [11, Thm. 4.1]:

$$\|\psi(t_n) - \psi_I^n\|_{L^2} \leq C_m \frac{T}{\triangle t} \left(\frac{1}{M}\right)^m + CT\triangle t \quad \text{for all } m \in \mathbb{N},\ t_n \leq T,$$

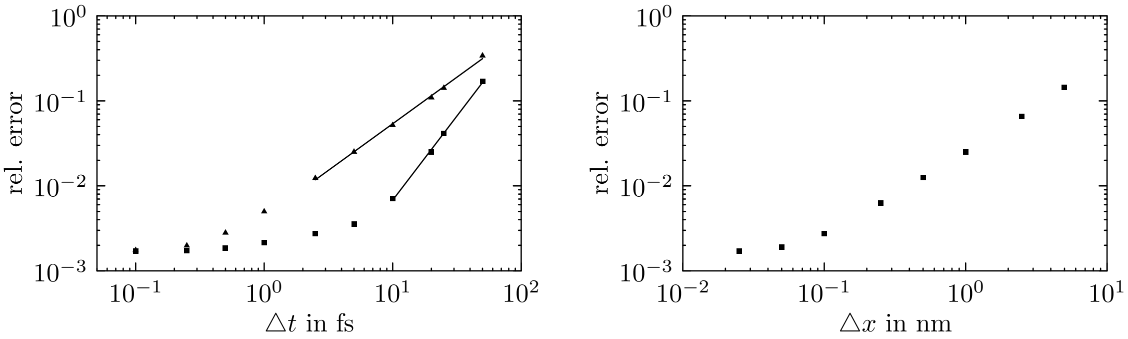

Figure 2.6: Relative errors for various time step sizes $\triangle t$ (left) and spatial discretizations $\triangle x$ (right) at time t = 500 fs. Triangles: Trotter time-splitting approximation, squares: Strang time-splitting approximation.

where ψ is the solution to the Schrödinger equation (2.1) with periodic boundary conditions and ψ_I^n is the time-splitting spectral approximation, obtained from

$$\psi_I^n(x) = \frac{1}{M} \sum_{k=-M/2}^{M/2-1} \widehat{\psi}_k^n e^{i\mu_k(x-a_1)}.$$

The constant $C_m > 0$ depends on the L^∞-norm of the m-th derivative of V and the L^2-norm of the m-th derivative of ψ, and $C > 0$ contains the operator-splitting error. It is difficult to compare our numerical convergence rate with the theoretical result, since we would need to include the error due to the approximation of the transparent boundary conditions via absorbing potentials. Moreover the value of C_m is not easy to compute. However, on a graphical level, the solution obtained from the time-splitting spectral method can not be distinguished from the reference solution as illustrated in Figure 2.7.

2.2.2 Simulation of two-dimensional quantum waveguide devices

The electron transport in a quantum T-stub waveguide is based on the interference of electron waves. The electrons have two main paths, one straight path from source to drain and another path going by the stub (Figure 2.8). The gate voltage modifies the penetration of the electron wave function in the lateral stub. The trajectories interfere constructively or deconstructively, depending on the stub length [4]. Thus, there are two states: the transmission is (almost) one, corresponding to an on-state, or zero, corresponding to an off-state. In this sense, the device acts as a nanoscale switch, also referred to as a quantum (interference) transistor [4]. The mobility of the electrons is assumed to be confined to two space dimensions realized by $Al_{0.3}Ga_{0.7}As/GaAs$ heterostructures such that it is sufficient to solve the two-dimensional Schrödinger equation.

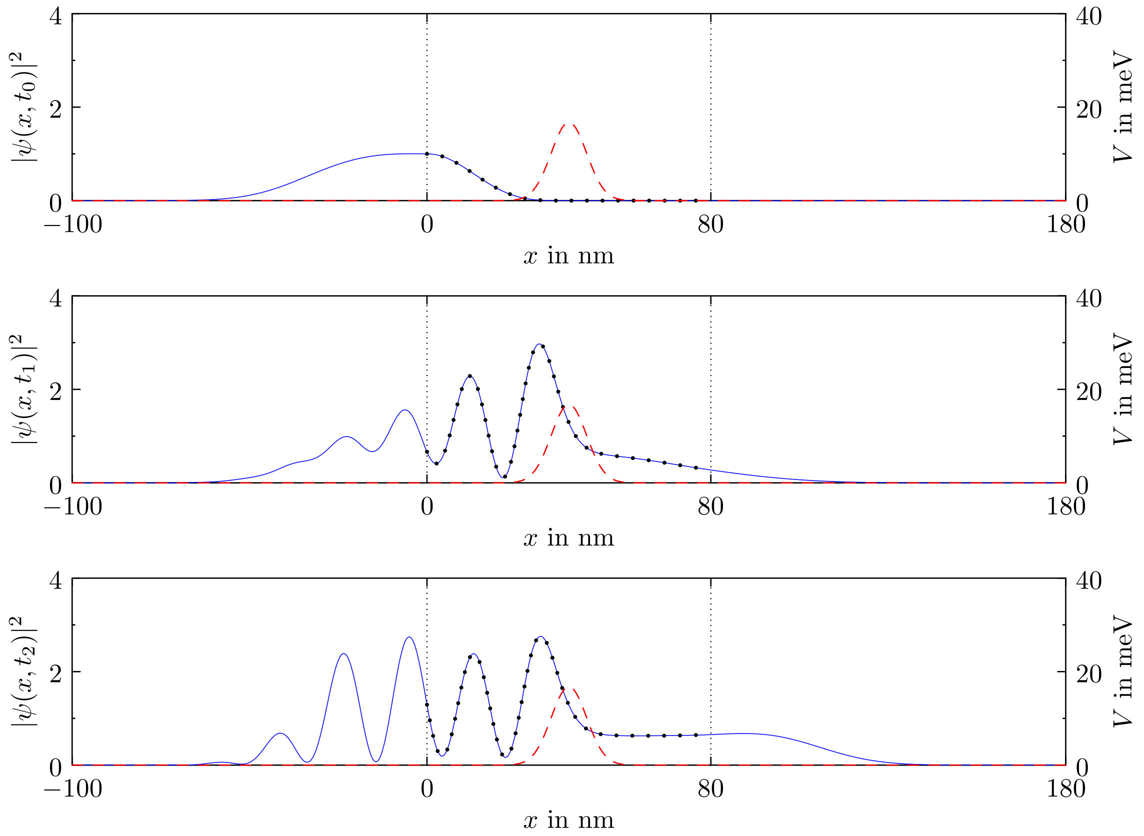

Figure 2.7: Evolution of a reference solution and the solution computed with the spectral method at times $t_0 = 0\,\mathrm{fs}$, $t_1 = 250\,\mathrm{fs}$ and $t_2 = 500\,\mathrm{fs}$. The reference solution is obtained from a Crank-Nicolson discretization in combination with discrete transparent boundary conditions. The discretization parameters are $\triangle x = 0.0025\,\mathrm{nm}$ and $\triangle t = 0.005\,\mathrm{fs}$. The time-splitting spectral approximation is computed with $\triangle x = 0.25\,\mathrm{nm}$ and $\triangle t = 0.25\,\mathrm{fs}$. Solid line: time-splitting spectral method, dotted line: reference solution.

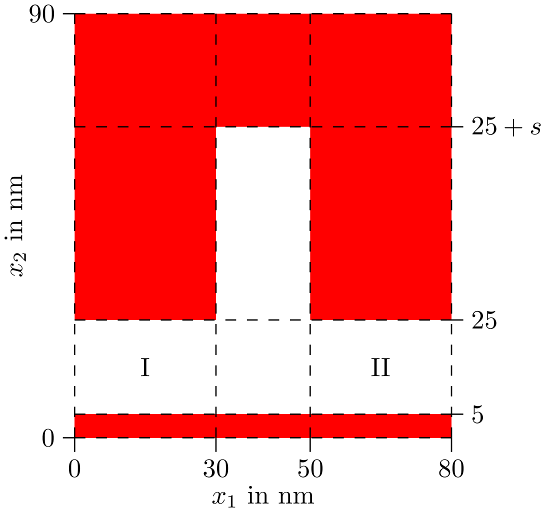

Figure 2.8: Geometry of the quantum stub transistor.

The geometry of the simulated quantum transistor is similar to that of [9, 22], compare Figure 2.8. The length of the transistor is 80 nm, the width of the stub is 20 nm and its length varies between 20 nm and 60 nm. The computational domain is the rectangle $\Omega = [-100, 180] \times [0, 90]\,\mathrm{nm}^2$, and periodic boundary conditions are imposed on that domain. In contrast to the simulations in [9, 22], the heterostructure is not modeled by hard walls and square corners but by a smooth, finite confinement potential with maximal value 1 eV. The profile of the potential is depicted in Figure 2.9. The material is GaAs with the effective mass $m^* = 0.067 m_0$.

Due to the translation invariance of the waveguide problem without stub in the x_1-direction, the stationary full wave function can be separated as

$$\psi_{k,n}(x_1, x_2) = e^{ikx_1}\phi_n(x_2),$$

where the exponential part corresponds to a plane wave associated to the wave vector k. The energy is given by the sum of the energy corresponding to ϕ_n and the kinetic energy in x_1-direction, $E = E_n + (\hbar k)^2/2m^*$. The wave function ϕ_n is a solution to the stationary Schrödinger equation

$$-\frac{\hbar^2}{2m^*}\frac{\partial^2 \phi_n}{\partial x_2^2} + V(x_2)\phi_n = E_n \phi_n$$

with periodic boundary conditions. This equation is solved by a simple central finite-difference scheme together with the sparse eigenvalue solver `eigs` of *Matlab*. The ground state ϕ_0 and the first excited state ϕ_1 are shown in Figure 2.9. The wave functions decrease exponentially at the transition to the finite potential, whereas in the case of hard walls, they vanish at the walls. The ground state has the energy $E_0 = 13.16\,\mathrm{meV}$, which is not much smaller than the energy of the ground state $E_0^* = 14.03\,\mathrm{meV}$ corresponding to the infinite square well case.

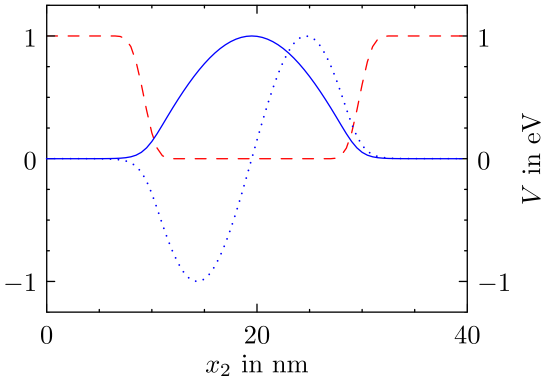

Figure 2.9: Profile of the confinement potential (dashed line), the ground state with $E_0 = 13.16\,\mathrm{meV}$ (solid line) and the first excited state with $E_1 = 52.33\,\mathrm{meV}$ (dotted line).

The electrons are continuously fed into the lead using the plane wave pulse described in Section 2.1.3. We note that the angular frequency $\omega = E/\hbar$ occuring in the factor $e^{-i\omega\triangle t}$ is computed by employing the total energy E. The incoming wave has the energy $E = 29.9\,\mathrm{meV}$ (as in [9]), comprised of the ground-state energy $E_0 = 13.16\,\mathrm{meV}$ to confine the electrons in the channel and the kinetic energy 16.74 meV. This means that we perform the simulation using the lowest transversal mode only. We have chosen $\triangle x_1 = \triangle x_2 = 0.5\,\mathrm{nm}$ corresponding to $M_1 = 560$ and $M_2 = 160$ grid points. The time step size equals $\triangle t = 0.25\,\mathrm{fs}$.

In this subsection, we are interested in the stationary behavior in order to compare our simulation results with those of [9, 22]. A (quasi) steady state is reached after about 2 ps within 67 seconds computing time on an Intel Core 2 Quad Q9550 CPU @ 2.83GHz × 4. The probability densities corresponding to the stub lengths $s_1 = 22.5\,\mathrm{nm}$, $s_2 = 31.5\,\mathrm{nm}$, $s_3 = 41\,\mathrm{nm}$, and $s_4 = 50\,\mathrm{nm}$ are shown in Figure 2.10. The conductance of the transistor with stub lengths s_2 and s_4 almost vanishes, i.e., the electrons interfere in such a way that (almost) no electrons can flow through the device. This corresponds to an off-state of the transistor. The transmission becomes maximal at the stub lengths s_1 and s_3, corresponding to an on-state of the device.

The transmission through the device as a function of the stub length is shown in Figure 2.11. As above, the incident energy equals 29.9 meV. The transmission at time t_n is approximated by the quotient

$$\sum_{j_2=0}^{M_2-1} |\psi^n_{i_r,j_2}|^2 \Big/ \sum_{j_2=0}^{M_2-1} |\psi^0_{i_\ell,j_2}|^2, \tag{2.5}$$

where $\psi^n_{j_1,j_2}$ approximates the wave function $\psi(a_1 + j_1\triangle x_1, j_2\triangle x_2, t_n)$ and i_ℓ and i_r are the indices of the grid points at $x_1 = 0$ and $x_1 = 80\,\mathrm{nm}$. Since the numerical solution does not reach a perfect steady state, the transmission is averaged over the time interval from 5 ps to 6 ps. Interestingly, we find the off- and on-states (31.5 nm

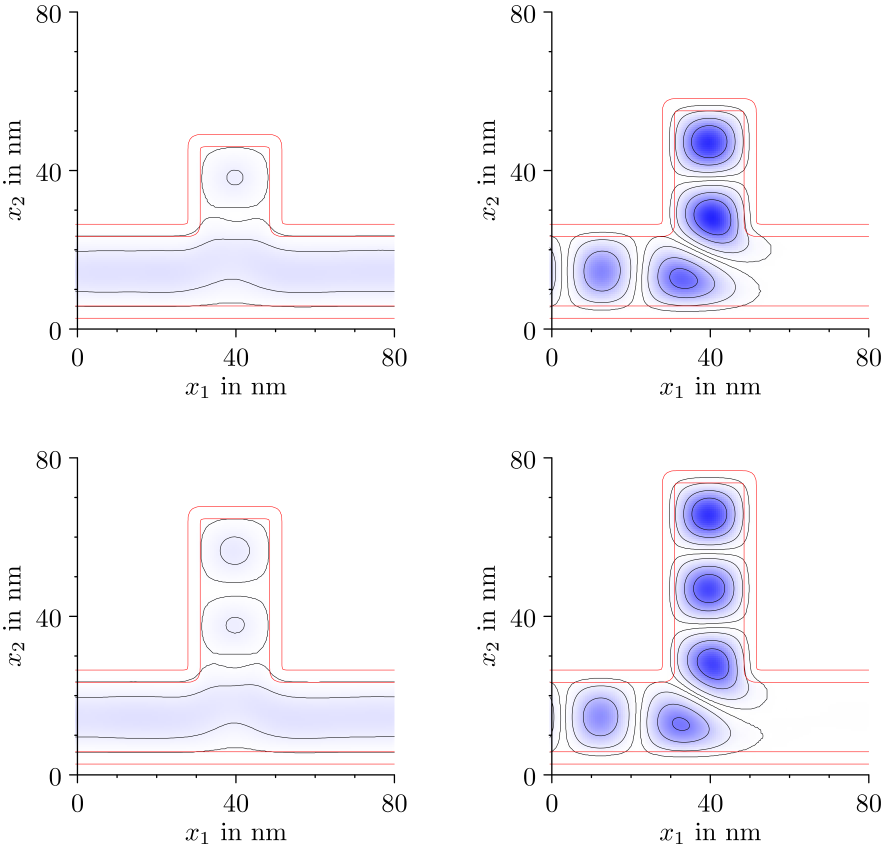

Figure 2.10: Probability densities in the quantum transistor for stub lengths 22.5 nm, 31.5 nm (upper row) and 41 nm, 50 nm (lower row) at $t = 2$ ps. Isolines of the density $|\psi|^2$ are shown at the values 0.05, 0.5, 2, 4, and those of the potential V at 0.05 eV, 0.95 eV.

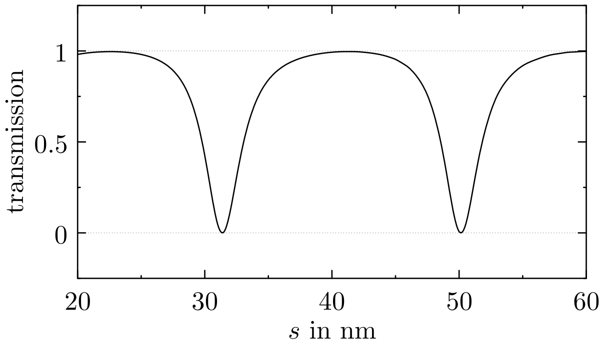

Figure 2.11: Transmissions of the quantum transistor, averaged over the time interval from 5 ps to 6 ps, depending on the stub length s.

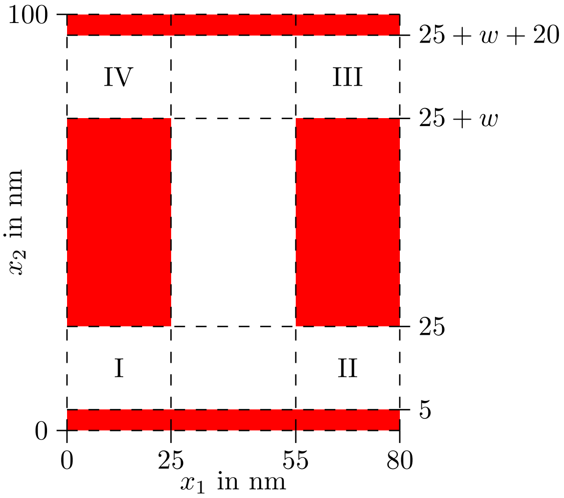

Figure 2.12: Geometry of the single-branch coupler.

and 41.0 nm, respectively) at almost the same stub lengths as in [22] (32 nm and 40.5 nm), although we employ a smoothed confinement potential in contrast to the hard-wall potential of [22]. This shows that the solution using a smoothed potential does not differ significantly from the hard-wall solution.

As a second example we simulate a single-branch coupler, which is an example of a multiport structure. The coupler consists of four ports, coupled through a small window in the middle; see Figure 2.12. A detailed study of the conductance in a single-branch coupler with hard walls can be found in [22]. The geometry is taken from [22]. The window width equals $w = 30\,\mathrm{nm}$, and the computational domain is $[-100, 180] \times [0, 100]\,\mathrm{nm}^2$. Like in the previous example we employ a smoothed potential with the maximal value 1 eV.

The mono-energetic plane wave pulse is injected at the lower left lead of the device (port I). The other ports are numbered counter-clockwise. Depending on the incident energy (and the window width), we obtain different steady states and different transmissions τ_{12}, τ_{13}, and τ_{14}, which are defined similarly as in (2.5). The transmissions as a function of the kinetic energy are shown in Figure 2.13. The transmission τ_{14} from port I to port IV is maximal at 16.5 meV, i.e., the injected electrons leave most likely the device at port IV. The corresponding probability density is illustrated in Figure 2.14 (left). In Figure 2.14 (right), the density for a window width $w = 51\,\mathrm{nm}$ is shown. Compared to the results of [22], we find the same interference patterns, and τ_{14} reaches its maximum value for almost the same energy (which equals $16.37\,\mathrm{meV} = 30.4\,\mathrm{meV} - 14.03\,\mathrm{meV}$ in [22, p. 710]), although we employ a smoothed potential.

We note that all simulations are performed with the same absorbing potential (2.4) where $V_0 = 50\,\mathrm{meV}$. This choice turned out to be appropriate if the kinetic energy of the electrons is between 15 meV and 25 meV. For different kinetic energies,

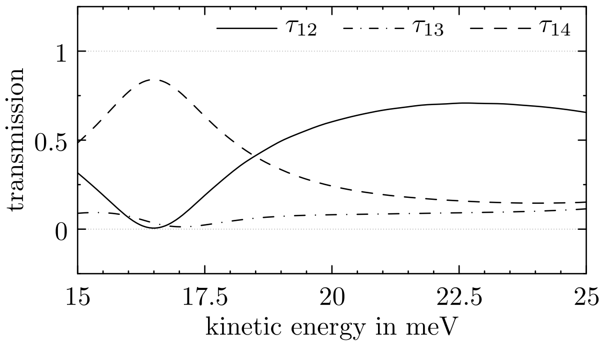

Figure 2.13: Transmissions from port I to ports II, III, and IV, respectively, of the single-branch coupler, averaged over the time interval from 5 ps to 6 ps.

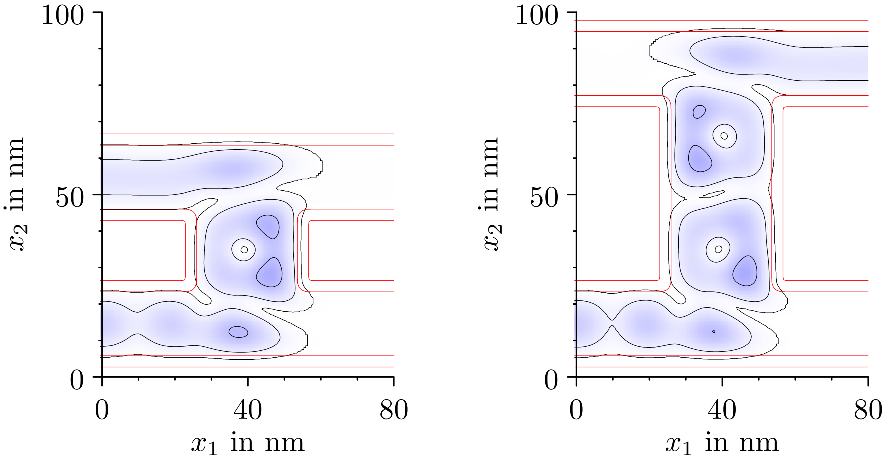

Figure 2.14: Probability densities of the single-branch coupler at time $t = 2$ ps. The kinetic energy of the electrons injected in the lower left port amounts to 16.5 meV. The window width equals $w = 20$ nm (left) and $w = 51$ nm (right).

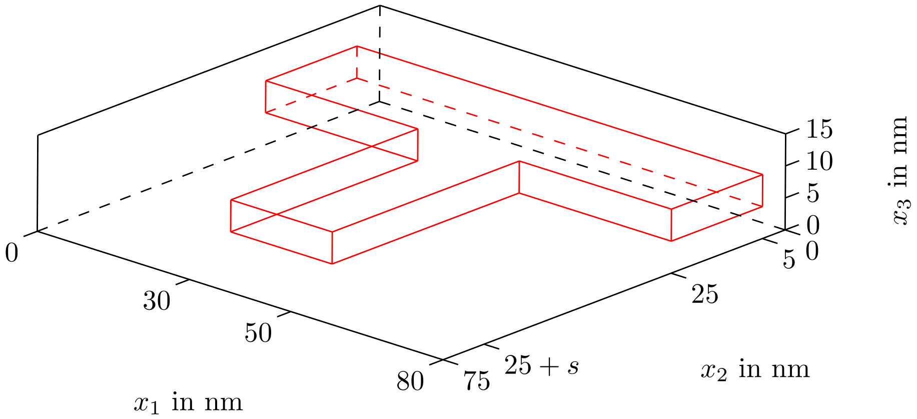

Figure 2.15: Geometry of the T-stub quantum interference transistor.

the absorbing potential needs to be adapted, which is a significant disadvantage of the method compared to, for instance, the method of [9]. However, we stress the fact that, due to the simple absorbing potential technique, our algorithm is fast, and three-dimensional simulations are feasible (see below).

2.2.3 Simulation of a three-dimensional quantum interference transistor

The mobility of electrons in a quantum waveguide is essentially confined to two space dimensions. Therefore, we choose a channel height of only 5 nm, whereas the total length of the quantum transistor is 80 nm and the waveguide width is 20 nm (see Figure 2.15). The stub length is between 33 nm and 43 nm.

The channel profile is depicted in Figure 2.16. The ground state and the first excited state are computed from the two-dimensional Schrödinger equation. The three-dimensional simulations are performed on a grid with $\triangle x_1 = \triangle x_2 = \triangle x_3 = 0.5\,\mathrm{nm}$ and a time step size of $\triangle t = 0.25\,\mathrm{fs}$. Complex arrays of size $560 \times 150 \times 30$ are needed to store the wave function, the potential, and three auxiliary variables. We note that the total memory consumption amounts to only 322 MB. The simulation presented below took about four hours computing time on an Intel Core 2 Quad Q9550 CPU @ 2.83GHz × 4.

Figures 2.17-2.18 show the transient behavior of the probability density in the T-stub transistor at different times. At time $t = 0\,\mathrm{ps}$, the stub length is fixed at $s_1 = 33\,\mathrm{nm}$. It takes about 2 ps to reach a (quasi) steady state. It can be clearly seen that the device is in the off-state. From $t = 2\,\mathrm{ps}$ to $t = 2.5\,\mathrm{ps}$, the stub length is continuously increased to $s_2 = 43\,\mathrm{nm}$. After another transient phase, the solution converges to a new (quasi) steady state. Apparently the transmission through the device becomes almost maximal and hence the device is in the on-state. During the period from $t = 5.5\,\mathrm{ps}$ to $t = 6\,\mathrm{ps}$ the stub length is decreased again to s_1 and the

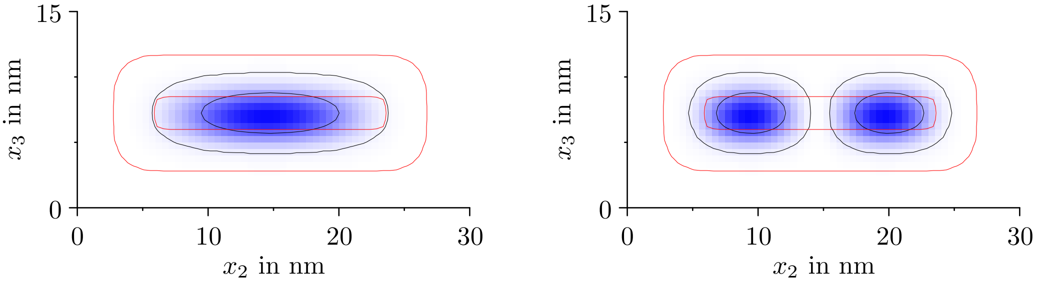

Figure 2.16: Cross section of the three-dimensional T-stub transistor, isolines of the potential at 0.05 eV and 0.95 eV, and the densities of the ground state with energy $E_0 = 176.98\,\text{meV}$ and the first excited state with $E_1 = 215.79\,\text{meV}$, together with the isolines at 0.05 and 0.5.

simulation is stopped at $t = 7.5\,\text{ps}$.

Figures 2.17-2.18 are realized as follows. Every 25 time steps, we calculate isosurfaces of the potential and the probability density using the *Matlab* built-in function `isosurface`. This function yields vertices and faces which describe a triangle mesh. The normals at the isosurface vertices are computed using the *Matlab* command `isonormals`. Finally, the matrices describing the vertices, faces, and normals are used to create representations of the isosurfaces which can be rendered with the ray tracing program POV-Ray [62]. In order to simultaneously visualize the outer and inner isosurfaces of the probability density at 0.05 and 0.25 we make the outer surface almost transparent. In total, 1200 scene description files have been rendered to create a movie illustrating the switching process. The rendering process took about six hours computing time on the above mentioned CPU.

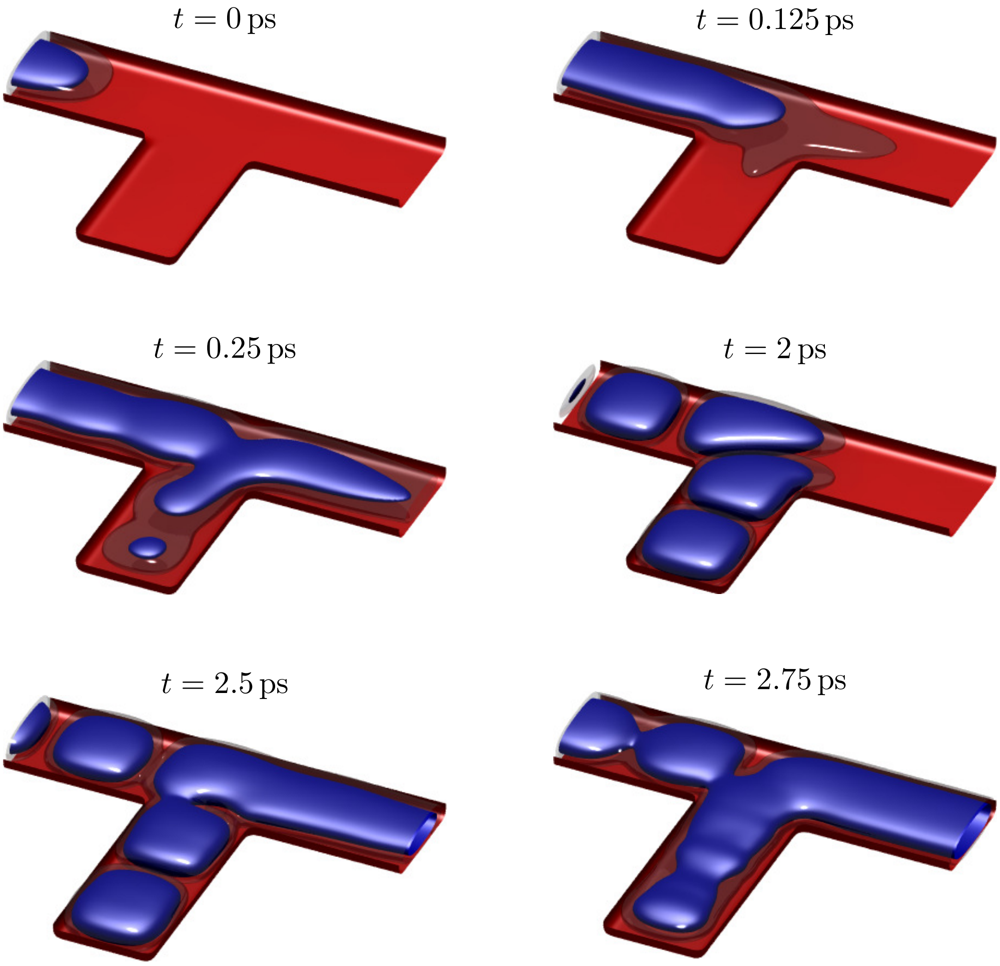

$t = 0\,\mathrm{ps}$

$t = 0.125\,\mathrm{ps}$

$t = 0.25\,\mathrm{ps}$

$t = 2\,\mathrm{ps}$

$t = 2.5\,\mathrm{ps}$

$t = 2.75\,\mathrm{ps}$

Figure 2.17: Probability density and potential energy in a simulation of a three-dimensional quantum interference transistor at various times. The red surface shows the isosurface (lower half) of the potential energy at 0.5 eV. The blue and the semi-transparent surfaces correspond to the isovalues 0.25 and 0.05 of the probability density.

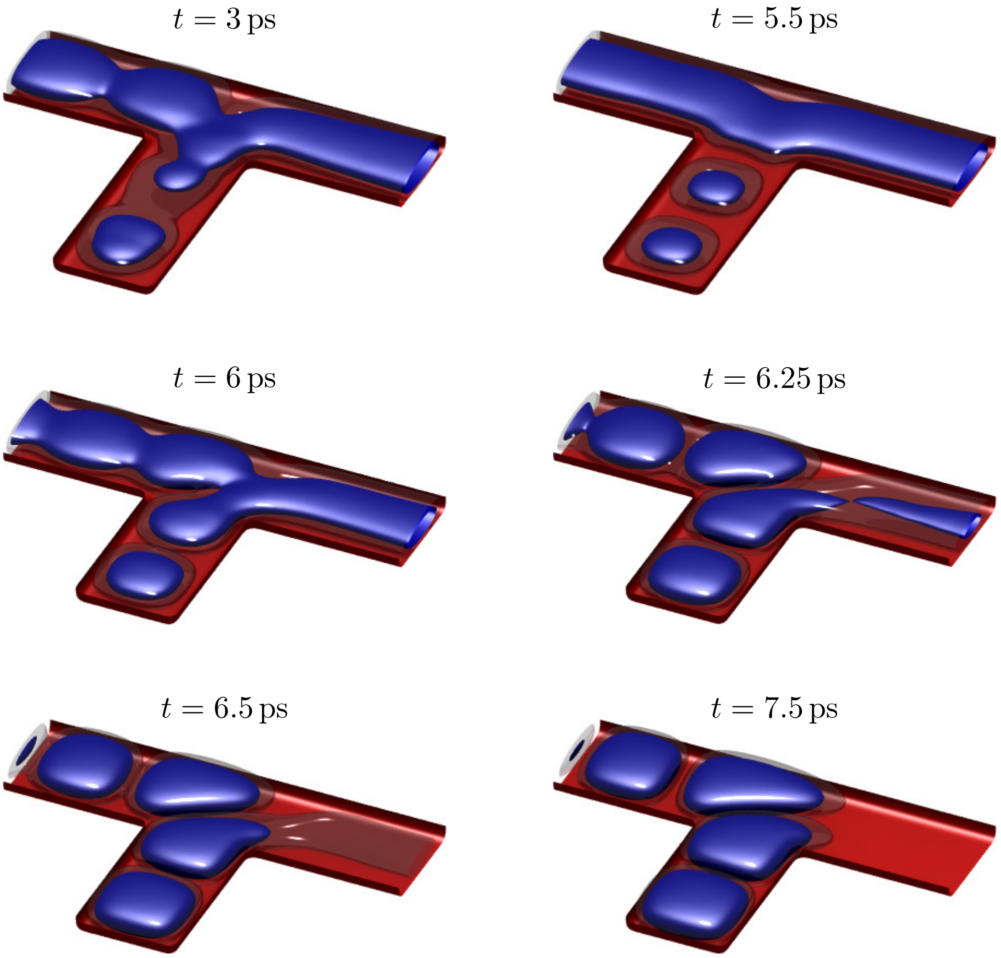

$t = 3\,\mathrm{ps}$ $t = 5.5\,\mathrm{ps}$

$t = 6\,\mathrm{ps}$ $t = 6.25\,\mathrm{ps}$

$t = 6.5\,\mathrm{ps}$ $t = 7.5\,\mathrm{ps}$

Figure 2.18: Probability density and potential energy in a simulation of a three-dimensional quantum interference transistor at various times. The red surface shows the isosurface (lower half) of the potential energy at 0.5 eV. The blue and the semi-transparent surfaces correspond to the isovalues 0.25 and 0.05 of the probability density.

Chapter 3

Transient Schrödinger-Poisson simulations of a high-frequency resonant tunneling diode oscillator

Chapter 3 is structured as follows. In Section 3.1, we explain the algorithm of the stationary problem. The transient algorithm is described in Section 3.2. In Section 3.3, we consider numerical experiments for constant and time-dependent applied voltages. Furthermore, we investigate the numerical convergence related to the approximation of the discrete convolution kernel by sum-of-exponentials. Finally, high-frequency oscillator circuit simulations are presented in Section 3.4.

3.1 Stationary simulations

The steady state is the basis for the transient simulations. Therefore, we discuss the stationary regime first.

3.1.1 Schrödinger-Poisson model

We assume that the one-dimensional device in $(0, L)$ is connected to the semi-infinite leads $(-\infty, 0]$ and $[L, \infty)$. The leads are assumed to be in thermal equilibrium and at constant potential. At the contacts, electrons are injected with some given profile. We suppose that the charge transport is ballistic and that the electron wave functions evolve independently from each other. The one-dimensional device consists of three regions: two highly doped regions, $[0, a_1]$ and $[a_6, L]$, with the doping concentration n_D^1 and a lowly doped region, $[a_1, a_6]$, with the doping density n_D^2 (see Figure 3.1). The middle interval contains a double barrier, described by the barrier potential

$$V_{\text{barr}}(x) = \begin{cases} V^\star & \text{for } x \in [a_2, a_3] \cup [a_4, a_5], \\ 0 & \text{else.} \end{cases}$$

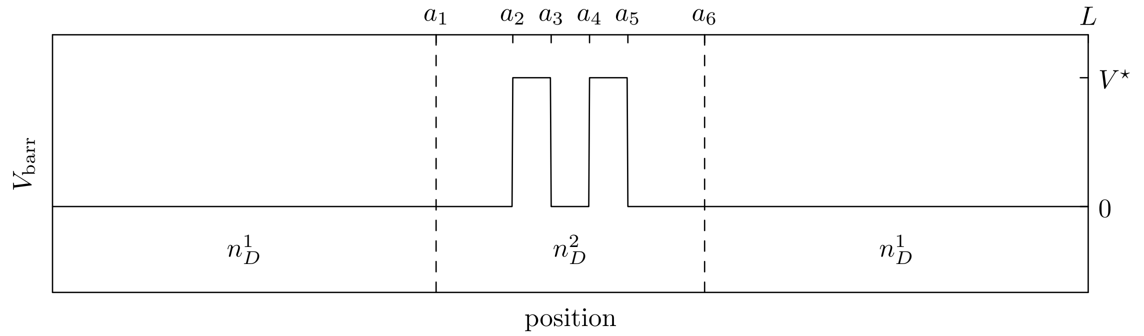

Figure 3.1: Barrier potential and doping profile of a double-barrier heterostructure.

The doping profile n_D is defined by

$$n_D(x) = \begin{cases} n_D^1 & \text{for } x \in [0, a_1] \cup [a_6, L], \\ n_D^2 & \text{else.} \end{cases}$$

The parameters are taken from [15, 66]:

$$\begin{array}{lll} a_1 = 50\,\text{nm}, & a_2 = 60\,\text{nm}, & a_3 = 65\,\text{nm}, \\ a_4 = 70\,\text{nm}, & a_5 = 75\,\text{nm}, & a_6 = 85\,\text{nm}, \\ L = 135\,\text{nm}, & n_D^1 = 10^{24}\,\text{m}^{-3}, & n_D^2 = 5 \cdot 10^{21}\,\text{m}^{-3}, \end{array}$$

and the barrier height is $V^\star = 0.3\,\text{eV}$.

The Coulomb interaction is taken into account at the Hartree level, i.e., by an infinite number of Schrödinger equations

$$-\frac{\hbar^2}{2m^\star}\frac{d^2\phi_k}{dx^2}(x) + V(x)\phi_k(x) = E(k)\phi_k(x), \quad x \in \mathbb{R}, \tag{3.1}$$

self-consistently coupled to the Poisson equation,

$$\begin{gathered} -\frac{d^2 V_{\text{self}}}{dx^2} = \frac{e^2}{\varepsilon}(n[V_{\text{self}}] - n_D), \quad x \in (0, L), \\ V_{\text{self}}(0) = 0, \quad V_{\text{self}}(L) = -eU, \end{gathered} \tag{3.2}$$

where $V = V_{\text{barr}} + V_{\text{self}}$ is the potential energy. The physical parameters are the reduced Planck constant $\hbar$, the effective electron mass $m^\star$, the elementary charge e, and the permittivity $\varepsilon = \varepsilon_r \varepsilon_0$, being the product of the relative permittivity ε_r and the electric constant ε_0. Furthermore, $U \geq 0$ denotes the applied voltage, and the electron density is defined by

$$n[V_{\text{self}}](x) = \int_{\mathbb{R}} g(k)|\phi_k(x)|^2 dk. \tag{3.3}$$

The injection profile $g(k)$ is given according to the Fermi-Dirac statistics by

$$g(k) = \frac{m^\star k_B T_0}{2\pi^2\hbar^2} \ln\left(1 + \exp\left(\frac{E_F - \hbar^2k^2/(2m^\star)}{k_B T_0}\right)\right), \tag{3.4}$$

where k_B is the Boltzmann constant, T_0 is the temperature of the semiconductor and E_F is the Fermi energy (relative to the conduction band edge). In all subsequent simulations, we use, as in [66], $\varepsilon_r = 11.44$, $T_0 = 300\,\mathrm{K}$, $E_F = 6.7097 \cdot 10^{-21}\,\mathrm{J}$, and the effective mass of Gallium arsenide, $m^\star = 0.067m_e$, with m_e being the electron mass at rest.

In order to define the total electron energy $E(k)$ depending on the wave number $k \in \mathbb{R}$, we need to distinguish the cases $k > 0$ and $k < 0$. For $k > 0$, the electrons enter from the left, and we have $E(k) = \hbar^2k^2/(2m^\star)$. The wave function in the leads is given by

$$\begin{aligned}
\phi_k(x) &= e^{ikx} + r(k)e^{-ikx}, \quad x < 0,\\
\phi_k(x) &= t(k)\exp\left(i\sqrt{2m^\star(E(k) - V(L))/\hbar^2}x\right), \quad x > L.
\end{aligned}$$

Eliminating the transmission and reflection coefficients $t(k)$ and $r(k)$, respectively, the boundary conditions

$$\phi_k'(0) + ik\phi_k(0) = 2ik, \quad \phi_k'(L) = i\sqrt{2m^\star(E(k) - V(L))/\hbar^2}\phi_k(L) \tag{3.5}$$

follow. For $k < 0$, the electrons enter from the right. The total energy is given by $E(k) = \hbar^2k^2/(2m^\star) - eU$, and the wave function in the leads reads as

$$\begin{aligned}
\phi_k(x) &= t(k)\exp\left(-i\sqrt{2m^\star E(k)/\hbar^2}x\right), \quad x < 0,\\
\phi_k(x) &= e^{ikx} + r(k)e^{-ikx}, \quad x > L.
\end{aligned}$$

This yields the boundary conditions

$$\phi_k'(0) = -i\sqrt{2m^\star E(k)/\hbar^2}\phi_k(0), \quad \phi_k'(L) + ik\phi_k(L) = 2ike^{ikL}. \tag{3.6}$$

Summarizing, the stationary problem consists in the Schrödinger equation (3.1) with the transparent boundary conditions (3.5)-(3.6) coupled to the Poisson equation (3.2) via the electron density (3.3). We remark that the existence and uniqueness of solutions to a Schrödinger-Poisson boundary-value problem similar to (3.1)-(3.6) has been shown in [14].

3.1.2 Discrete transparent boundary conditions

We recall the finite-difference discretization of the stationary Schrödinger equation with transparent boundary conditions [6]. Using standard second-order finite differences on the equidistant grid $x_j = j\triangle x$, $j \in \{0, \dots, J\}$, with $x_J = L$ and $\triangle x > 0$, we find for the grid points located in the computational domain,

$$\phi_{j+1} - 2\phi_j + \phi_{j-1} + \frac{2m^\star(\triangle x)^2}{\hbar^2}(E(k) - V_j)\phi_j = 0. \tag{3.7}$$

It is well known that a standard centered finite-difference discretization of the boundary conditions (3.5) and (3.6) may lead to spurious oscillations in the numerical solution [6]. In principle, the numerical errors can be made as small as desired by choosing $\triangle x$ sufficiently small. However, since the stationary solutions will serve as intitial states in our transient simulations, we need to avoid any spurious oscillations, which would otherwise be propagated with every time step.

For this, we apply (stationary) discrete transparent boundary conditions compatible with the finite-difference discretization (3.7) as proposed in [6]. For the sake of completeness, we review the derivation. Note that the final discretization is equivalent to the discretization (3.7) extended to the whole space, i.e. for $j \in \mathbb{Z}$.

In the semi-infinite leads $j \leq 0$ and $j \geq J$, the potential energy is assumed to be constant,

$$V_j = \begin{cases} V_0 = 0 & \text{for } j \leq 0, \\ V_J = -eU & \text{for } j \geq J. \end{cases}$$

Then (3.7) reduces to a difference equation with constant coefficients which admits two solutions of the form $\phi_j = (\alpha_{0,J}^{\pm})^j$, where

$$\alpha_{0,J}^{\pm} = 1 - \frac{m^\star(E(k) - V_{0,J})(\triangle x)^2}{\hbar^2} \pm i\sqrt{\frac{2m^\star(E(k) - V_{0,J})(\triangle x)^2}{\hbar^2} - \frac{(m^\star)^2(E(k) - V_{0,J})^2(\triangle x)^4}{\hbar^4}}.$$

Here, $E(k) - V_{0,J}$ corresponds to the kinetic energy $E_{0,J}^{\text{kin}}(k)$ in the left or right lead. In case $E_{0,J}^{\text{kin}}(k) > 0$, the solution is a discrete plane wave and $(\triangle x)^2 < 2\hbar^2/(m^\star(E(k) - V_{0,J}))$ is needed to ensure $|\alpha_{0,J}| = 1$, which in practise is not a restriction. In case $E_{0,J}^{\text{kin}}(k) = 0$, the solution is constant. Depending on the applied voltage, $E_{0,J}^{\text{kin}}(k)$ might also become negative. In that case, the solution is decaying or growing exponentially fast and we select the decaying solution as it is the only physically reasonable solution.

In practice, we start with the calculation of the total energy $E(k) = E_{0,J}^{\text{kin}}(k) + V_{0,J}$. For electrons coming from the left contact we have $E(k) = E_0^{\text{kin}}(k)$. As the incoming electron is represented by a discrete plane wave, $E_0^{\text{kin}}(k)$ is positive but, depending on the applied voltage, $E_J^{\text{kin}}(k)$ might be positive, zero or negative. For electrons coming from the right contact, we have $E(k) = E_J^{\text{kin}}(k) - eU$. Again, the incoming wave function is a discrete plane wave, i.e., $E_J^{\text{kin}}(k) > 0$ but nothing is said about $E_0^{\text{kin}}(k)$. At this point it should be noted that the kinetic energy of the incoming electron is related to the wave number according to the discrete E–k–relation

$$E^{\text{kin}}(k) = \frac{\hbar^2}{m^\star(\triangle x)^2}(1 - \cos(k\triangle x)), \tag{3.8}$$

which follows after solving the centered finite-difference discretization of the free

Schrödinger equation

$$-\frac{\hbar^2}{2m^\star(\triangle x)^2}\left(e^{ik(x_j-\triangle x)}-2e^{ikx_j}+e^{ik(x_j+\triangle x)}\right)=E^{\mathrm{kin}}e^{ikx_j},$$

or

$$-\frac{\hbar^2}{2m^\star(\triangle x)^2}\left(-2+e^{-ik\triangle x}+e^{+ik\triangle x}\right)=E^{\mathrm{kin}}(k).$$

Substituting $e^{-ik\triangle x}+e^{+ik\triangle x}$ with $2\,\mathrm{Re}(e^{ik\triangle x})=2\cos(k\triangle x)$ yields (3.8). In the limit $\triangle x\to 0$, we recover the continuous relation $E^{\mathrm{kin}}(k)=\hbar^2k^2/(2m^\star)$.

Let us consider a wave function entering the device from the left contact ($k>0$). For $j\le 0$, the solution to (3.7) is a superposition of an incoming and a reflected discrete plane wave, $\phi_j=\beta^j+B\beta^{-j}$, where $\beta=\alpha_0$. We eliminate B from $\phi_{-1}=\beta^{-1}+B\beta$, $\phi_0=1+B$ to find the discrete transparent boundary condition at x_0:

$$-\beta^{-1}\phi_{-1}+\phi_0=1-\beta^{-2}.$$

For $j\ge J$, the solution to (3.7) is given by $\phi_j=C\gamma^j$ with $\gamma=\alpha_J$. This means that $\phi_{J+1}=C\gamma^{J+1}=\gamma\phi_J$, and the boundary condition at x_J becomes

$$\phi_J-\gamma^{-1}\phi_{J+1}=0.$$

Summarizing, we obtain the linear system $A\phi=b$ with the tridiagonal matrix A consisting of the main diagonal $(-\beta^{-1},-2+2m^\star(\triangle x)^2(E(k)-V_0)/\hbar^2,\dots,-2+2m^\star(\triangle x)^2(E(k)-V_J)/\hbar^2,-\gamma^{-1})$ and the first off diagonals $(1,\dots,1)$. The vector of the unknowns is given by $\phi=(\phi_{-1},\dots,\phi_{J+1})^\top$ and b represents the right-hand side $b=(1-\beta^{-2},0,\dots,0)^\top$.

The case of a wave function entering from the right contact ($k<0$) works analogously.

3.1.3 Solution of the Schrödinger-Poisson system

We explain our strategy to solve the coupled Schrödinger-Poisson system. To this end, we introduce the equidistant energy grid

$$\mathcal{K}=\{-k_M,-k_M+\triangle k,\dots,-\triangle k,+\triangle k,\dots,k_M-\triangle k,k_M\},\quad K:=|\mathcal{K}|. \tag{3.9}$$

The electron density (3.3) is approximated by

$$n_{\mathrm{disc}}[V_{\mathrm{self}}](x)=\triangle k\sum_{k\in\mathcal{K}}g(k)|\phi_k(x)|^2,$$

where the Fermi-Dirac statistics $g(k)$ is defined in (3.4) and the functions ϕ_k are the scattering states, i.e., the solutions to the discretized stationary Schrödinger equation (3.7) with discrete transparent boundary conditions as described in Section 3.1.2. This approximation is reasonable if $\triangle k$ is sufficiently small and k_M is sufficiently large. In the numerical simulations below, we choose $K = 3000$ and, as in [15, Section 5], $k_M = \sqrt{2m^\star(E_F + 7k_BT_0)}/\hbar$, recalling that $E_F = 6.7097 \cdot 10^{-21}$ J and $T_0 = 300\,\mathrm{K}$.

The discrete Schrödinger-Poisson system is iteratively solved as follows. We set $V = V_{\mathrm{barr}} + V^{(p)}_{\mathrm{self},U}$, where $V^{(p)}_{\mathrm{self},U}$ is the p-th iteration of V_{self} for the applied voltage U. Given V, we compute a set of quasi eigenstates $\{\phi^{(p)}_k\}_{k\in\mathcal{K}}$. This defines the discrete electron density

$$n_{\mathrm{disc}}[V^{(p)}_{\mathrm{self},U}] = \triangle k \sum_{k\in\mathcal{K}} g(k)|\phi^{(p)}_k(x)|^2.$$

The Poisson equation is solved by employing a Gummel-type method [39]:

$$\begin{aligned} &-\frac{d^2}{dx^2}V^{(p+1)}_{\mathrm{self},U} = \frac{e^2}{\varepsilon}\left(n[V^{(p)}_{\mathrm{self},U}]\exp\left(\frac{V^{(p)}_{\mathrm{self},U} - V^{(p+1)}_{\mathrm{self},U}}{V^{\mathrm{ref}}_{\mathrm{self}}}\right) - n_D\right), \\ &V^{(p+1)}_{\mathrm{self},U}(0) = 0, \quad V^{(p+1)}_{\mathrm{self},U}(L) = -eU. \end{aligned}$$

The idea of the Gummel method is to decouple the Schrödinger and Poisson equations but to formulate the Poisson equation in a nonlinear way, using the relation between the electron density and electric potential in thermal equilibrium. The parameter $V^{\mathrm{ref}}_{\mathrm{self}}$ can be tuned to reduce the number of iterations; we found empirically that the choice $V^{\mathrm{ref}}_{\mathrm{self}} = 0.04\,\mathrm{eV}$ minimizes the number of iterations. If the relative error in the ℓ^2-norm is smaller than a fixed tolerance,

$$\left\| \frac{V^{(p+1)}_{\mathrm{self},U} - V^{(p)}_{\mathrm{self},U}}{V^{(p+1)}_{\mathrm{self},U}} \right\|_2 \le \delta, \tag{3.10}$$

we accept $V_{\mathrm{self}} := V^{(p+1)}_{\mathrm{self},U}$ and $\{\phi^{(p+1)}_k\}_{k\in\mathcal{K}}$ as the approximate self-consistent solution. Otherwise, we proceed with the iteration $p+1 \to p+2$ and compute a new set of scattering states. The procedure is repeated until (3.10) is fulfilled. We have choosen the tolerance $\delta = 10^{-6}$.

For zero applied voltage we use $V^{(0)}_{\mathrm{self},0\,\mathrm{mV}} = 0\,\mathrm{mV}$ to start the iteration. Only 7 iterations are needed until criterion (3.10) is fulfilled. As a result we obtain $V^{(7)}_{\mathrm{self},0\,\mathrm{mV}}$, which is depicted in Figure 3.2 (left part, solid line).

Numerical problems arise when non-equilibrium solutions are computed. As an example we consider the case of a small applied voltage $U = 1\,\mathrm{mV}$. To start the iteration process we use the previously computed solution, i.e., we set $V^{(0)}_{\mathrm{self},1\,\mathrm{mV}} := V^{(7)}_{\mathrm{self},0\,\mathrm{mV}}$. The next iterations are illustrated in Figure 3.2 (left part, dashed lines). Obviously they do not converge and are physically not realistic. This phenomenon is well-known in the literature [32, 33] and is believed to be related to the absence of inelastic processes in the Schrödinger-Poisson equations.

In the literature [15, 66], a modified version of the Schrödinger-Poisson equations is employed to overcome this problem. The modification concerns the description of

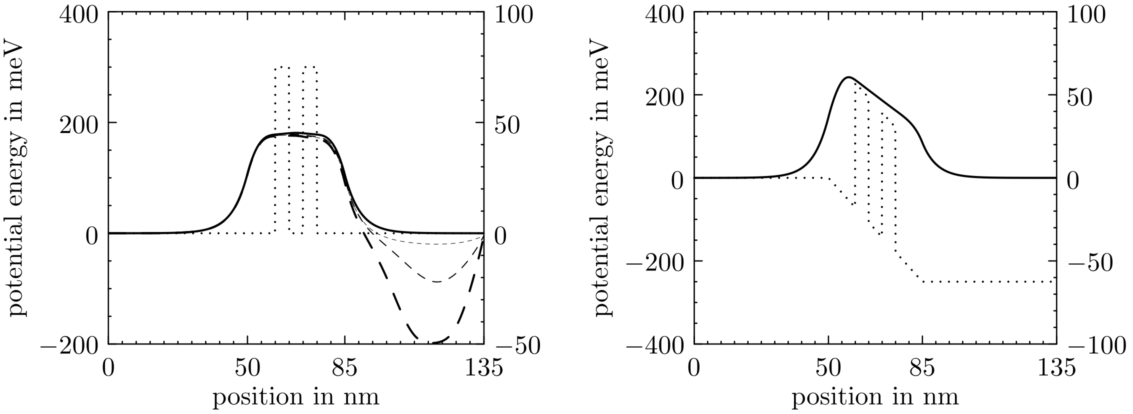

Figure 3.2: Left part: Solid line: self-consistent solution V_{self} for $U = 0\,\text{mV}$, found after 7 iterations. Dashed lines: divergent approximations for $U = 1\,\text{mV}$. Dotted line: barrier potential. Right part: Solid line: self-consistent solution V_1 for $U = 250\,\text{mV}$ according to approximation (3.11). Dotted line: sum of the barrier and the ramp-like potential.

the potential energy in the Poisson equation. For this, we write the Poisson equation (3.2) as follows:

$$\begin{aligned} -\frac{d^2V_0}{dx^2} &= 0 && \text{in } (0,L), \quad V_0(0) = 0, \quad V_0(L) = -eU, \\ -\frac{d^2V_1}{dx^2} &= \frac{e^2}{\varepsilon}(n - n_D) && \text{in } (0,L), \quad V_1(0) = 0, \quad V_1(L) = 0, \end{aligned}$$

i.e., the self-consistent potential is $V_{\text{self}} = V_0 + V_1$. The first boundary-value problem can be solved explicitly: $V_0(x) = -eUx/L$, $x \in [0, L]$. In [15, 66], the linearly decreasing potential V_0 has been replaced by the ramp-like potential

$$\widetilde{V}_0(x) = -eU\left(\frac{x - a_1}{a_6 - a_1}\mathbf{1}_{[a_1,a_6)} + \mathbf{1}_{[a_6,\infty)}\right), \quad x \in [0, L], \tag{3.11}$$

where $\mathbf{1}_I$ is the characteristic function on the interval $I \subset \mathbb{R}$ (see Figure 3.1 for the definition of a_1 and a_6). The function $\widetilde{V}_0 + V_{\text{barr}}$ is illustrated in Figure 3.2 (right part, dotted line). The potential energy is then given by $V = \widetilde{V}_0 + V_1 + V_{\text{barr}}$. Using this modified physical model, the above Gummel iteration scheme for the Poisson equation describing V_1 converges without any problems, see Figure 3.2 (right part, solid line), even for large applied voltages. However, we will see below that the results from the modified model differ considerably from the results obtained by the original Schrödinger-Poisson model. Furthermore, the potential energy is no longer differentiable at a_1 and a_6. This may be interpreted as a model of surface charge densities at the interfaces which, however, are not intended in the model.

In fact, we are able to solve numerically the original Schrödinger-Poisson problem. To this end, the applied voltage needs to be increased in small steps. We

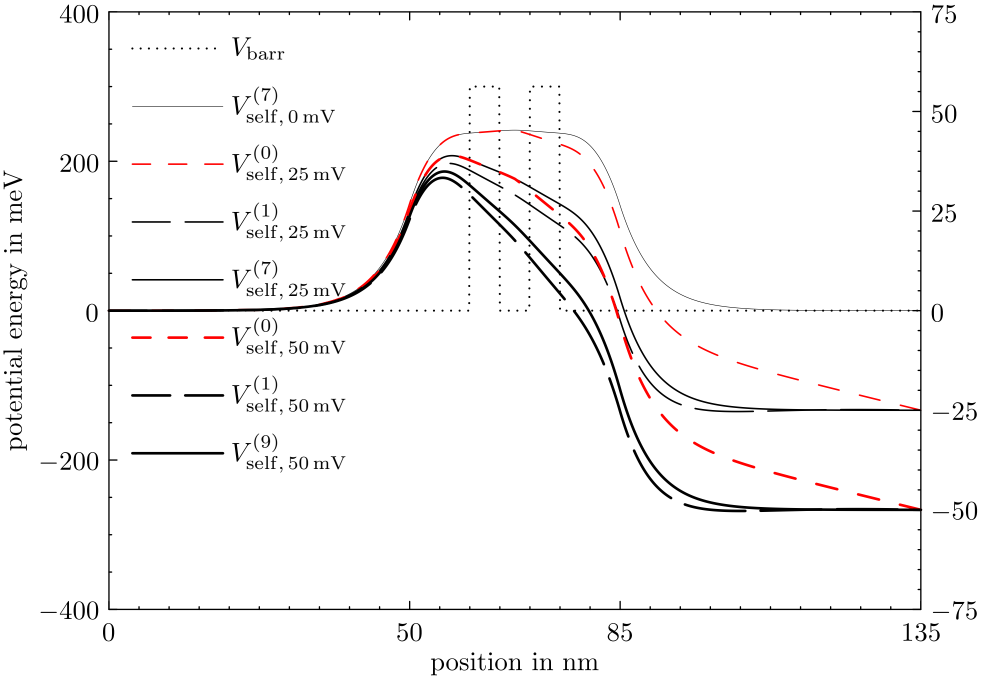

Figure 3.3: Some iterations computed according to (3.12).

found that the starting potential in each step needs to be initialized carefully. More precisely, given the self-consistent solution $V_{\mathrm{self,U}}$ for the applied voltage U, we wish to compute a self-consistent solution with the applied voltage $U + \triangle U$. In each step we choose

$$V^{(0)}_{\mathrm{self},U+\triangle U}(x) := V_{\mathrm{self},U}(x) - \triangle U \frac{2x - L}{L} \mathbf{1}_{[L/2,L]} \tag{3.12}$$

to start the iteration. For $U = 0\,\mathrm{mV}$ and $\triangle U = 25\,\mathrm{mV}$, the Gummel scheme converges to a physically reasonable solution after 7 iterations. Some iterations are shown in Figure 3.3. We observed that a voltage step $\triangle U < 30\,\mathrm{mV}$ leads to convergent solutions also for large applied voltages.

In order to compare the original Schrödinger-Poisson model with the model using approximation (3.11), we computed the current-voltage characteristics shown in Figure 3.4. Here, the (conduction) current density

$$J_{\mathrm{cond}} = \frac{e\hbar}{m} \int_{\mathbb{R}} g(k) \mathrm{Im} \left(\phi_k^* \frac{d\phi_k}{dx} \right) dk \tag{3.13}$$

is approximated by a simple quadrature formula using symmetric finite differences to compute $d\phi_k/dx$. Figure 3.4 shows that the results differ considerably, i.e., the choice (3.11) leads to different results than those computed from the original model. Therefore, we employ the original description of the potential energy in the transient simulations of the next sections.

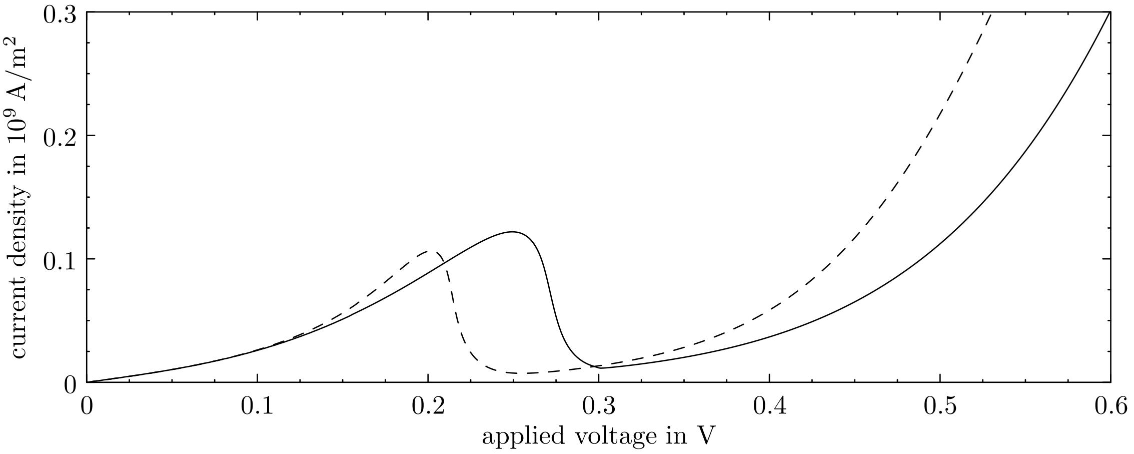

Figure 3.4: Current-voltage characteristics. The solid line corresponds to our solution of the original stationary Schrödinger-Poisson system. The dashed line is obtained with the modified model using approximation (3.11).

3.2 Transient simulations

In this section, we detail the numerical discretization of the transient Schrödinger equations

$$i\hbar\frac{\partial\psi_k}{\partial t} = -\frac{\hbar^2}{2m^\star}\frac{\partial^2\psi_k}{\partial x^2}+V(\cdot,t)\psi_k, \quad \psi_k(\cdot,0)=\phi_k, \quad x\in[0,L],\ t>0,\ k\in\mathcal{K}, \tag{3.14}$$

with discrete transparent boundary conditions, where $\mathcal{K}$ is defined in (3.9). To simplify the presentation, we skip in this section the index k.

3.2.1 Inhomogeneous discrete transparent boundary conditions

The transient Schrödinger equation (3.14) is discretized by the commonly used Crank-Nicolson scheme:

$$\begin{aligned} \psi_{j-1}^{(n+1)} + \Big(iR-2+wV_j^{(n+1/2)}\Big)\psi_j^{(n+1)} + \psi_{j+1}^{(n+1)} \\ = -\psi_{j-1}^{(n)} + \Big(iR+2-wV_j^{(n+1/2)}\Big)\psi_j^{(n)} - \psi_{j+1}^{(n)}, \end{aligned} \tag{3.15}$$

where $\psi_j^{(n)}$ approximates $\psi(x_j,t_n)$ with $x_j = j\triangle x$ and $t_n = n\triangle t$ ($j\in\mathbb{Z}$, $n\in\mathbb{N}_0$), $V_j^{(n+1/2)}$ approximates $V(j\triangle x,(n+1/2)\triangle t)$, and $R = 4m^\star(\triangle x)^2/(\hbar\triangle t)$, $w = -2m^\star(\triangle x)^2/\hbar^2$.

Under the assumptions that the initial wave function is compactly supported in $(0,L)$ and that the exterior potential vanishes, $V(x,t)=0$ for $x\le 0$ and $x\ge L$,

$t \geq 0$, it is well known (see, e.g., [6, 12]) that transparent boundary conditions for the Schrödinger equation (3.14) read:

$$\frac{\partial \psi}{\partial x}(x,t)\big|_{x=0} = +\sqrt{\frac{2m^\star}{\pi\hbar}}\, e^{-i\pi/4} \frac{d}{dt}\int_0^t \frac{\psi(0,\tau)}{\sqrt{t-\tau}}\, d\tau, \tag{3.16a}$$

$$\frac{\partial \psi}{\partial x}(x,t)\big|_{x=L} = -\sqrt{\frac{2m^\star}{\pi\hbar}}\, e^{-i\pi/4} \frac{d}{dt}\int_0^t \frac{\psi(L,\tau)}{\sqrt{t-\tau}}\, d\tau. \tag{3.16b}$$

Based on (3.16) one can easily derive transparent boundary conditions for nonzero exterior potentials which are spatially constant but may change with time [3]. As an example, we consider $V(x,t) = V_r(t)$ for $x \geq L$, $t \geq 0$, $V_r(t) := -eU(t)$ where $U(t)$ denotes the applied voltage. To get rid of the potential in the right lead we define

$$\widetilde{\psi}(x,t) := e^{i\int_0^t V_r(s)\,ds/\hbar}\psi(x,t) \quad x \geq L,\, t \geq 0.$$

This phase shift is sometimes referred to as a gauge change in quantum mechanics. The new function solves the free time-dependent Schrödinger equation and consequently (3.16b) yields a transparent boundary condition for a time-dependent exterior potential in the right lead

$$\frac{\partial \psi}{\partial x}(x,t)\big|_{x=L} = -\sqrt{\frac{2m^\star}{\pi\hbar}}\, e^{-i\pi/4} e^{-i\int_0^t V_r(s)\,ds/\hbar} \frac{d}{dt}\int_0^t \frac{e^{i\int_0^t V_r(s)\,ds/\hbar}\psi(L,\tau)}{\sqrt{t-\tau}}\, d\tau.$$

For zero exterior potentials discrete transparent boundary conditions at the left ($x_0 = 0$) and the right ($x_J = L$) contact, based on the above Crank-Nicolson scheme are given as follows (see [5] for the derivation):

$$\psi_1^{(n+1)} - s^{(0)}\psi_0^{(n+1)} = \sum_{\ell=1}^{n} s^{(n+1-\ell)}\psi_0^{(\ell)} - \psi_1^{(n)}, \quad n \geq 0, \tag{3.17a}$$

$$\psi_{J-1}^{(n+1)} - s^{(0)}\psi_J^{(n+1)} = \sum_{\ell=1}^{n} s^{(n+1-\ell)}\psi_J^{(\ell)} - \psi_{J-1}^{(n)}, \quad n \geq 0, \tag{3.17b}$$

with the convolution coefficients

$$s^{(n)} = \left(1 - i\frac{R}{2}\right)\delta_{n,0} + \left(1 + i\frac{R}{2}\right)\delta_{n,1} + \alpha e^{-in\varphi}\frac{P_n(\mu) - P_{n-2}(\mu)}{2n-1} \tag{3.18}$$

and the abbreviations

$$\varphi = \arctan\frac{4}{R}, \quad \mu = \frac{R}{\sqrt{R^2+16}}, \quad \alpha = \frac{i}{2}\sqrt[4]{R^2(R^2+16)}\,e^{i\varphi/2}.$$

Here, P_n denotes the nth-degree Legendre polynomial ($P_{-1} = P_{-2} = 0$), and $\delta_{n,j}$ is the Kronecker symbol. In practice, the coefficients defined in (3.18) are computed with an efficient three-term recursion, relying on the three-term recursion of the

Legendre polynomials [31]. The Crank-Nicolson scheme (3.15) along with these discrete transparent boundary conditions yields an unconditionally stable discretization which is perfectly free of reflections [5, 6].

Next, let the initial wave function be a solution to the stationary Schrödinger equation with energy E and let the exterior potential at the right contact be given by a time-dependent function, $V(x,t) = -eU(t)$ for $x \geq L$, $t \geq 0$. This leads to inhomogeneous transparent boundary conditions [2]. We describe our strategy to discretize these boundary conditions. Our approach is motivated by that presented in [15, Appendix B], but we suggest, similarly as in [6], a discretization of the gauge change which is compatible with the underlying finite-difference scheme. Additionally, our approach requires only a single set of convolution coefficients instead of two.

Applying (3.16) to $\psi - \psi^{\mathrm{inc}}$ yields inhomogeneous transparent boundary conditions describing a time-dependent incoming wave ψ^{inc} prescribed at the left or right device contact [3]. Inhomogeneous transparent boundary conditions suitable for the problem outlined above follow similarly [6]. In order to derive the boundary condition at the left contact we apply (3.16a) to the difference of the wave function ψ and the time-evolution of the scattering state $\exp(-iEt/\hbar)\phi(x)$ which gives

$$\begin{aligned} &\frac{\partial}{\partial x}\left[\psi(x,t) - e^{-iEt/\hbar}\phi(x)\right]\Big|_{x=0} \\ &\qquad = \sqrt{\frac{2m^\star}{\pi\hbar}}e^{-i\pi/4}\frac{d}{dt}\int_0^t \frac{\psi(0,\tau) - e^{-iE\tau/\hbar}\phi(0)}{\sqrt{t-\tau}}\,d\tau. \end{aligned} \tag{3.19}$$

To be able to apply (3.16b) we first employ a gauge change to get rid of the time-dependent potential $V_r(t) = -eU(t)$. It is easy to show that

$$\exp(i\int_0^t V_r(s)ds/\hbar)\psi(x,t)$$

and

$$\exp(iV_r(0)t/\hbar)\exp(-iEt/\hbar)\phi(x)$$

solve the free time-dependent Schrödinger equation in the right contact. Hence, the application of (3.16b) to

$$\varphi(x,t) := \exp\left(\frac{i}{\hbar}\int_0^t V_r(s)ds\right)\psi(x,t) - \exp(iV_r(0)t/\hbar)\exp(-iEt/\hbar)\phi(x) \tag{3.20}$$

yields the desired inhomogeneous transparent boundary condition at the right contact

$$\begin{aligned} &\frac{\partial}{\partial x}\left[e^{i\int_0^t V_r(s)\,ds/\hbar}\psi(x,t) - e^{iV_r(0)t/\hbar}e^{-iEt/\hbar}\phi(x)\right]\Big|_{x=L} \\ &\quad = -\sqrt{\frac{2m^\star}{\pi\hbar}}e^{-i\pi/4}\frac{d}{dt}\int_0^t \frac{e^{i\int_0^\tau V_r(s)\,ds/\hbar}\,\psi(L,\tau) - e^{iV_r(0)\tau/\hbar}e^{-iE\tau/\hbar}\phi(L)}{\sqrt{t-\tau}}\,d\tau. \end{aligned} \tag{3.21}$$

Let us now derive an inhomogeneous discrete transparent boundary condition at $x_J = L$ which is consistent with the Crank-Nicolson scheme. To this end, we replace $\varphi(x,t)$ by some approximation $\varphi_j^{(n)}$. Subsequently we apply (3.17b). The question is how to approximate the quantities

$$\exp(i\int_0^t V_r(s)ds/\hbar)$$

and

$$\exp(iV_r(0)t/\hbar)\exp(-iEt/\hbar).$$

Indeed, the ad-hoc discretization for $t = n\triangle t$,

$$\begin{aligned} \exp\left(\frac{i}{\hbar}\int_0^t V_r(s)ds\right) &\approx \exp\left(\frac{i}{\hbar}\sum_{\ell=0}^{n-1} V_r^{(\ell+1/2)}\triangle t\right), \\ \exp\left(\frac{i}{\hbar}V_r(0)t\right)\exp\left(-\frac{i}{\hbar}Et\right) &= \exp\left(\frac{i}{\hbar}\left(V_r^{(0)}-E\right)n\triangle t\right), \end{aligned} \tag{3.22}$$

where $V_r^{(\ell)} = V_r(\ell\triangle t)$, is not derived from the underlying finite-difference discretization, causing unphysical numerical reflections at the boundary. In principle, these reflections can be made arbitrarily small for $\triangle t \to 0$. However, for practical time step sizes, the resulting current density would be distorted. Our idea is to apply the Crank-Nicolson time-integration method to a differential equation satisfied by $\exp(i\int_0^t V_r(s)ds/\hbar)$. Indeed, this expression solves

$$\frac{d\varepsilon}{dt}(t) = \frac{i}{\hbar}V_r(t)\varepsilon(t), \quad \varepsilon(0) = 1.$$

The Crank-Nicolson discretization of this ordinary differential equation reads

$$\varepsilon^{(n+1)} = \varepsilon^{(n)} + \triangle t\frac{i}{2\hbar}V_r^{(n+1/2)}(\varepsilon^{(n+1)}+\varepsilon^{(n)}), \quad \varepsilon^{(0)} = 1.$$

This recursion relation can be solved explicitly yielding

$$\varepsilon^{(n)} = \exp\left(2i\sum_{\ell=0}^{n-1}\arctan\left(\frac{\triangle t}{2\hbar}V_r^{(\ell+1/2)}\right)\right), \quad n \in \mathbb{N}_0.$$

A Taylor series expansion

$$2i\arctan\left(\frac{\triangle t}{2\hbar}V_r^{(\ell+1/2)}\right) = \frac{i}{\hbar}V_r^{(\ell+1/2)}\triangle t + O((\triangle t)^3)$$

reveals that in the limit $\triangle t \to 0$, the ad-hoc discretization in (3.22) coincides with the discrete gauge change which is derived from the Crank-Nicolson time-integration method.

Analogously, $\exp(iV_r(0)t/\hbar)\exp(-iEt/\hbar)$ needs to be replaced by

$$\begin{aligned}\gamma_J^{(n)} &:= \exp\left(2i\sum_{\ell=0}^{n-1}\arctan\left(\frac{\triangle t}{2\hbar}V_r^{(0)}\right)\right)\exp\left(2i\sum_{\ell=0}^{n-1}\arctan\left(-\frac{\triangle t}{2\hbar}E\right)\right)\\ &= \exp\left[2in\left(\arctan\left(\frac{\triangle t}{2\hbar}V_r^{(0)}\right)-\arctan\left(\frac{\triangle t}{2\hbar}E\right)\right)\right], \quad n\in\mathbb{N}_0.\end{aligned}$$

Thus, the discrete analogon of φ in definition (3.20) is given by

$$\varphi_j^{(n)} = \varepsilon^{(n)}\psi_j^{(n)} - \gamma_J^{(n)}\phi_j, \quad n\in\mathbb{N}_0.$$

Replacing $\psi_j^{(n)}$ by $\varphi_j^{(n)}$ in (3.17b), we obtain the desired inhomogeneous discrete transparent boundary condition at $x_J = L$:

$$\begin{aligned}\epsilon^{(n+1)}\psi_{J-1}^{(n+1)} - s^{(0)}\epsilon^{(n+1)}\psi_J^{(n+1)} =& -\epsilon^{(n)}\psi_{J-1}^{(n)} + \sum_{\ell=1}^{n} s^{(n+1-\ell)}\left(\epsilon^{(\ell)}\psi_J^{(\ell)} - \gamma_J^{(\ell)}\phi_J\right)\\ &- s^{(0)}\gamma_J^{(n+1)}\phi_J + \left(\gamma_J^{(n+1)}+\gamma_J^{(n)}\right)\phi_{J-1}.\end{aligned} \tag{3.23}$$

At the left contact $x_0 = 0$, an inhomogeneous discrete transparent boundary condition can be derived in a similar way. Since the potential energy in the left lead is assumed to vanish, the term $\varepsilon^{(n)}$ is not needed, and the boundary condition is given by

$$\begin{aligned}\psi_1^{(n+1)} - s^{(0)}\psi_0^{(n+1)} =& -\psi_1^{(n)} + \sum_{\ell=1}^{n} s^{(n+1-\ell)}\left(\psi_0^{(\ell)} - \gamma_0^{(\ell)}\phi_0\right)\\ &- s^{(0)}\gamma_0^{(n+1)}\phi_0 + \left(\gamma_0^{(n+1)}+\gamma_0^{(n)}\right)\phi_1,\end{aligned} \tag{3.24}$$

where

$$\gamma_0^{(n)} := \exp\left(-2in\arctan\left(\frac{\triangle t}{2\hbar}E\right)\right), \quad n\in\mathbb{N}_0.$$

We summarize: The Crank-Nicolson scheme (3.15) with the inhomogeneous discrete transparent boundary conditions (3.23) and (3.24) reads as

$$B\psi^{(n+1)} = C\psi^{(n)} + d^{(n)}, \tag{3.25}$$

where $\psi^{(n)} = (\psi_0^{(n)},\ldots,\psi_J^{(n)})^\top$, $d = (d_0^{(n)},0,\ldots,0,d_J^{(n)})^\top$. Furthermore, B is a tridiagonal matrix with main diagonal

$$(-s^{(0)}, iR-2+wV_1^{(n+1/2)},\ldots,iR-2+wV_{J-1}^{(n+1/2)},-s^{(0)}\varepsilon^{(n+1)}),$$

upper diagonal $(1,\ldots,1)$, and lower diagonal $(1,\ldots,1,\varepsilon^{(n+1)})$; C is a tridiagonal matrix with main diagonal $(0, iR+2-wV_1^{(n+1/2)},\ldots,iR+2-wV_{J-1}^{(n+1/2)},0)$, upper diagonal $(-1,\dots,-1)$ and lower diagonal $(-1,\dots,-1,-\varepsilon^{(n)})$; furthermore,

$$d_0^{(n)} = \sum_{\ell=1}^{n} s^{(n+1-\ell)} \left(\psi_0^{(\ell)} - \gamma_0^{(\ell)}\phi_0\right) - s^{(0)}\gamma_0^{(n+1)}\phi_0 + \left(\gamma_0^{(n+1)} + \gamma_0^{(n)}\right)\phi_1, \tag{3.26}$$

$$d_J^{(n)} = \sum_{\ell=1}^{n} s^{(n+1-\ell)} \left(\epsilon^{(\ell)}\psi_J^{(\ell)} - \gamma_J^{(\ell)}\phi_J\right) - s^{(0)}\gamma_J^{(n+1)}\phi_J + \left(\gamma_J^{(n+1)} + \gamma_J^{(n)}\right)\phi_{J-1}. \tag{3.27}$$

3.2.2 Fast evaluation of the discrete convolution terms

In the subsequent simulations, scheme (3.25) has to be solved in each time step and for every wave function $\psi = \psi_k$, $k \in \mathcal{K}$. We recall that the kernel coefficients $s^{(n)}$ need to be calculated only once as they do not depend on the wave number k. Let N denote the number of time steps. For each $k \in \mathcal{K}$, we require $\mathcal{O}(N)$ storage units and $\mathcal{O}(N^2)$ work units to compute the discrete convolutions in (3.26) and (3.27). For this reason, simulations with several ten thousands of time steps are not feasible. To overcome this problem, one may truncate the convolutions at some index, since the decay rate of the convolution coefficients is of the order $\mathcal{O}(n^{-3/2})$ [31, Section 3.3]. The drawback of this approach is that still more than thousand convolution terms are necessary to avoid unphysical reflections at the boundaries.

The problem has been overcome in [8] by approximating the original convolution coefficients $s^{(n)}$ and calculating the approximated convolutions by recursion. More precisely, approximate $s^{(n)}$ by

$$\widetilde{s}^{(n)} := \begin{cases} s^{(n)}, & n < \nu, \\ \sum_{\ell=1}^{\Lambda} b_l q_l^{-n}, & n \geq \nu, \end{cases}$$

such that

$$\mathcal{C}^{(n)}(u) := \sum_{\ell=1}^{n-\nu} \widetilde{s}^{(n-\ell)} u^{(\ell)} \approx \sum_{\ell=1}^{n-\nu} s^{(n-\ell)} u^{(\ell)} \tag{3.28}$$

can be evaluated by a recurrence formula which reduces the numerical effort drastically. As in [8], we set $\nu = 2$ to exclude $s^{(0)}$ and $s^{(1)}$ from the approximation. In fact, $s^{(0)}$ does not appear in the original convolutions, whereas $s^{(1)}$ is excluded to increase the accuracy.

Let $\Lambda \in \mathbb{N}$. The set $\{b_0, q_0 \dots, b_\Lambda, q_\Lambda\}$ is computed as follows. First, define the formal power series

$$h(x) := s^{(\nu)} + s^{(\nu+1)}x + s^{(\nu+2)}x^2 + \cdots + s^{(\nu+2\Lambda-1)}x^{\nu+2\Lambda-1} + \cdots, \quad |x| \leq 1.$$

The first (at least 2Λ) coefficients are required to calculate the $[\Lambda-1|\Lambda]$-Padé approximation of h, $\widetilde{h}(x) := P_{\Lambda-1}(x)/Q_\Lambda(x)$, where $P_{\Lambda-1}$ and Q_Λ are polynomials of degree $\Lambda - 1$ and Λ, respectively. If this approximation exists, we can compute its

Taylor series $\widetilde{h}(x) = \widetilde{s}^{(\nu)} + \widetilde{s}^{(\nu+1)}x + \cdots$, and by definition of the Padé approximation, it holds that

$$\tilde{s}^{(n)} = s^{(n)} \quad \text{for all } n \in \{\nu, \nu+1, \dots, \nu+2\Lambda-1\}.$$

It can be shown that, if Q_Λ has Λ simple roots q_ℓ with $|q_\ell| > 1$ for all $\ell \in \{1, \dots, \Lambda\}$, the approximated coefficients are given by

$$\tilde{s}^{(n)} = \sum_{\ell=1}^{\Lambda} b_\ell q_l^{-n}, \quad b_\ell := -\frac{P_{\Lambda-1}(q_\ell)}{Q_\Lambda(q_\ell)} q_\ell^{\nu-1} \neq 0, \quad n \geq \nu,\ \ell \in \{1, \dots, \Lambda\}. \tag{3.29}$$

Summarizing, one first computes the exact coefficients $s^{(0)}, \dots, s^{(\nu+2\Lambda-1)}$ followed by the $[\Lambda-1|\Lambda]$-Padé approximation. Then one determines the roots of Q_Λ, yielding the numbers $q_1, \dots, q_\Lambda$. Finally, one evaluates (3.29) to find the coefficients $b_0, \dots, b_\Lambda$. We stress the fact that these calculations have to be performed with high precision ($2\Lambda-1$ mantissa length) since otherwise the Padé approximation may fail (see [8]). We employ the Python library *mpmath* for arbitrary-precision floating-point arithmetics [45]. As an alternative, one may use the *Maple* script from [8, Appendix].

A particular feature of this approximation is that it can be calculated by recursion. More precisely, for $n \geq \nu+1$, the function $\mathcal{C}^{(n)}(u)$ in (3.28) can be written as

$$\mathcal{C}^{(n)}(u) = \sum_{\ell=1}^{\Lambda} C_\ell^{(n)}(u),$$

with

$$C_\ell^{(n)}(u) = q_\ell^{-1} C_\ell^{(n-1)}(u) + b_\ell q_\ell^{-2} u^{(n-2)}, \quad n \geq \nu+1, \quad C_\ell^{(\nu)}(u) = 0.$$

Hence, the discrete convolutions in (3.26) and (3.27) are approximated for $n \geq \nu = 2$ by

$$\sum_{\ell=1}^{n} s^{(n+1-\ell)} u^{(\ell)} \approx \mathcal{C}^{(n+1)}(u) + s^{(1)} u^{(n)}, \tag{3.30}$$

whereas the exact expressions are used for $n = 0$ and $n = 1$. As a result, the memory consumption for the implementation of the discrete transparent boundary conditions reduces from $\mathcal{O}(N)$ to $\mathcal{O}(\Lambda)$. Even more importantly, the work is of order $\mathcal{O}(\Lambda N)$ instead of $\mathcal{O}(N^2)$.

Obviously, the quality of the approximation depends on Λ. By construction, we have $s^{(n)} = \widetilde{s}^{(n)}$ for all $n \in \{0, \dots, 2\Lambda+\nu-1\}$ but $\widetilde{s}^{(n)}$ approximates $s^{(n)}$ very well even if n is much larger [8]. We illustrate in Section 3.3.3 that the convergence of the complete transient algorithm with respect to Λ is exponential.

3.2.3 The complete transient algorithm

In the previous sections, we have explained the approximation of the transient Schrödinger equation with discrete transparent boundary conditions for a given potential energy $V = V_{\mathrm{barr}} + V_{\mathrm{self}}$. Here, we make explicit the coupling procedure of the Poisson equation for the selfconsistent potential

$$-\frac{\partial^2 V_{\mathrm{self}}}{\partial x^2} = \frac{e^2}{\varepsilon}(n[V_{\mathrm{self}}] - n_D), \quad x \in (0, L), \quad V_{\mathrm{self}}(0,t) = 0,\ V_{\mathrm{self}}(L,t) = -eU(t),$$

with the electron density

$$n[V_{\mathrm{self}}](x,t) = \int_{\mathbb{R}} g(k)|\psi_k(x,t)|^2\,dk.$$

According to the Crank-Nicolson scheme, a natural approach would be to employ a two-step predictor-corrector scheme. More precisely, let $\{\psi_k^{(n)}\}_{k\in\mathcal{K}} \to \{\psi_k^{(*)}\}_{k\in\mathcal{K}}$ be propagated for one time step using $V_{\mathrm{self}}^{(n)}$ to obtain $V_{\mathrm{self}}^{(*)}$. Then one uses $V_{\mathrm{self}}^{(n+1/2)} := \frac{1}{2}(V_{\mathrm{self}}^{(n)} + V_{\mathrm{self}}^{(*)})$ to propagate $\{\psi_k^{(n)}\}_{k\in\mathcal{K}} \to \{\psi_k^{(n+1)}\}_{k\in\mathcal{K}}$ again. This procedure doubles the numerical effort and is computationally too costly. As an alternative, the scheme $V_{\mathrm{self}}^{(n+1/2)} := 2V_{\mathrm{self}}^{(n)} - V_{\mathrm{self}}^{(n-1/2)}$ can be employed (as in [66]). We found in our simulations that the most simple approach, $V_{\mathrm{self}}^{(n+1/2)} := V_{\mathrm{self}}^{(n)}$, gives essentially the same results as the above schemes. The reason is that the electron density evolves very slowly compared to the small time step size which is needed to resolve the fast oscillations of the wave functions. Hence, the variations of V_{self} are small. Similarly, the boundary condition of the Poisson equation $V_{\mathrm{self}}(L, (n+1)\triangle t) = -eU((n+1)\triangle t)$ can be replaced by $V_{\mathrm{self}}(L, (n+1)\triangle t) = -eU(n\triangle t)$ if the applied voltage varies slowly. This is used in the circuit simulations of Section 3.4. The complete transient algorithm is presented in Figure 3.5.

3.2.4 Discretization parameters

We choose $K = 3000$ for the number of wave functions as in the stationary simulations and $\triangle t = 1\,\mathrm{fs}$ (fs = femtosecond) for the time step size. With the maximal kinetic energy of injected electrons $\hbar\omega_M = \hbar^2 k_M^2/(2m^\star)$, where k_M is the maximal wave number, the period is computed according to $\tau_M = 2\pi/\omega_M$. Thus, the fastest wave oscillation is resolved by $\tau_M/\triangle t \approx 18.5$ time steps. The spatial grid size is chosen to be $\triangle x = 0.1\,\mathrm{nm}$. Consequently, the smallest wave length $\lambda_M = 2\pi/k_M \approx 10\,\mathrm{nm}$ is resolved by approximately 100 spatial grid points. Furthermore, we take $\Lambda = 70$ for the approximation parameter of the discrete convolution terms. This choice results from a numerical convergence study presented in Section 3.3.3.

It is important to note that the wave functions which are propagated using the fast evaluation of the approximated discrete convolution terms (3.30) practically coincide with the wave functions which are propagated using the exact convolutions

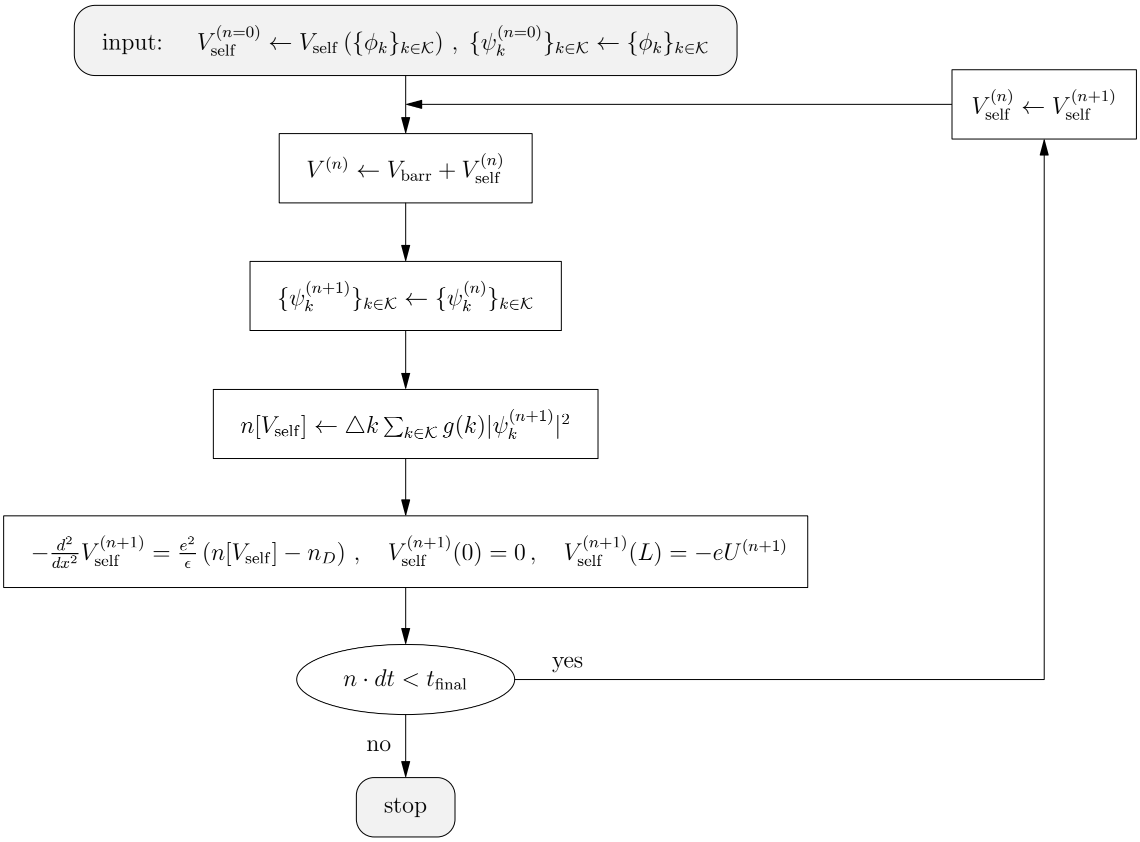
input: $V_{\text{self}}^{(n=0)} \leftarrow V_{\text{self}}\left(\{\phi_k\}_{k\in\mathcal{K}}\right)\,,\ \{\psi_k^{(n=0)}\}_{k\in\mathcal{K}} \leftarrow \{\phi_k\}_{k\in\mathcal{K}}$
$V_{\text{self}}^{(n)} \leftarrow V_{\text{self}}^{(n+1)}$
$V^{(n)} \leftarrow V_{\text{barr}} + V_{\text{self}}^{(n)}$
$\{\psi_k^{(n+1)}\}_{k\in\mathcal{K}} \leftarrow \{\psi_k^{(n)}\}_{k\in\mathcal{K}}$
$n[V_{\text{self}}] \leftarrow \triangle k \sum_{k\in\mathcal{K}} g(k)|\psi_k^{(n+1)}|^2$
$-\frac{d^2}{dx^2}V_{\text{self}}^{(n+1)} = \frac{e^2}{\epsilon}\left(n[V_{\text{self}}] - n_D\right)\,,\quad V_{\text{self}}^{(n+1)}(0) = 0\,,\quad V_{\text{self}}^{(n+1)}(L) = -eU^{(n+1)}$
yes
$n \cdot dt < t_{\text{final}}$
no
stop

Figure 3.5: Flow chart of the transient scheme.

(3.26)–(3.27) (see Section 3.3.3). Employing the exact convolutions, however, is equivalent to solving the Crank-Nicolson finite difference equations of the whole space problem. Considering that the electron density evolves smoothly in space and time, it is clear that the error of the complete transient algorithm (see Section 3.2.3) is determined by the Crank-Nicolson finite difference scheme. A global error estimate, together with a meshing strategy depending on a possibly scaled Planck constant $\hbar$ is given in [11]. The calculations in this chapter are performed without any scaling.

3.2.5 Details of the implementation

The final solver is implemented in the *C++* programming language using the matrix library *Eigen* [38] for concise and efficient computations. As we are interested in simulations with a very large number of time steps N (e.g., $N = 100\,000$), some sort of parallelization is indispensable. We employ the library *pthreads* to realize multiple threads on multi-core processors with shared memory. The most time consuming part in the transient algorithm (see Section 3.2.3) is the propagation of the wave functions and the calculation of the electron density. Since the wave functions evolve independently of each other, this task can be easily parallelized. At every time step, we create a certain number of threads (usually, this number equals the number of cores available). To each thread, we assign a subset of wave functions which are propagated as described above. Before the threads are joined again, each thread computes its part of the electron density. All these parts provide the total eletron density which is used to solve the Poisson equation in serial mode. The simulations presented below have been carried out on an Intel Core 2 Quad Q9550 CPU @ 2.83GHz × 4.

3.3 Numerical experiments

We present three numerical experiments. The first experiment demonstrates the importance to provide a completely consistent discretization of the open Schrödinger-Poisson system. The second experiment shows the time-dependent behavior of a resonant tunneling diode, which allows us to identify several physical mechanisms. In the third experiment, we investigate the convergence of our solver with respect to the parameter Λ which appears in the context of the fast evaluation of the discrete convolution terms.

3.3.1 First experiment: Constant applied voltage

We compute the stationary solution to the Schrödinger-Poisson system for an applied voltage of $U = 250\,\mathrm{mV}$. At this voltage, the current density achieves its first local maximum. We apply the transient algorithm of Section 3.2 until $t = 25\,\mathrm{fs}$,

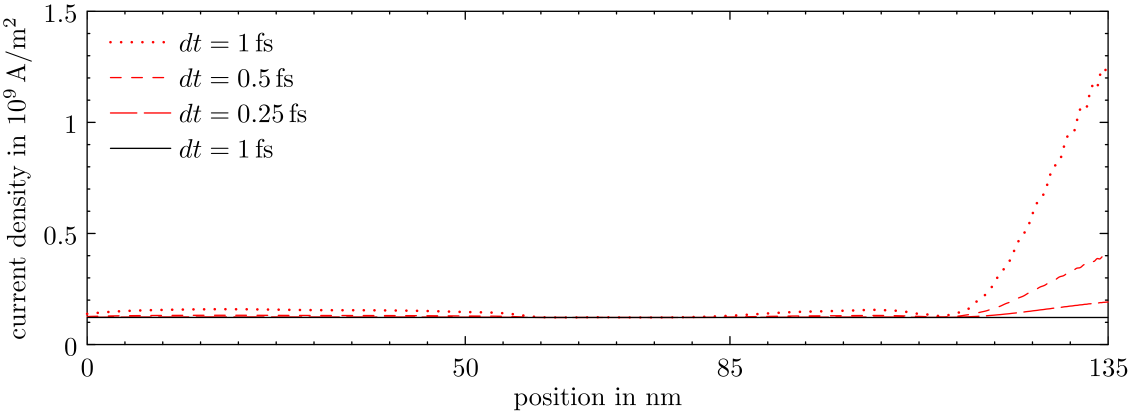

Figure 3.6: Conduction current density in a resonant tunneling diode at $t = 25\,\mathrm{fs}$ for a constant applied voltage of $U = 250\,\mathrm{mV}$. Discretizations using the ad-hoc discretization (3.22) of the analytical boundary conditions yield strongly distorted numerical solutions (broken lines). In contrast, the conduction current density computed with our solver is perfectly constant (solid line).

keeping the applied voltage constant. Accordingly, the stationary solution should be preserved and the current density J_{cond}, defined in (3.13), is expected to be spatially constant.

The ad-hoc discretization (3.22) is employed using the time step sizes $\triangle t = 1\,\mathrm{fs}$, $0.5\,\mathrm{fs}$, $0.25\,\mathrm{fs}$. We observe in Figure 3.6 that the current density is not constant. The reason is that the discretization (3.22) is not consistent with the underlying finite-difference scheme. The distortions are reduced for very small time step sizes but this increases the computing times significantly. In contrast, with the discrete gauge changes of Section 3.2.1, the current density is perfectly constant even for the rather large time step size $\triangle t = 1\,\mathrm{fs}$; see Figure 3.6.

We note that the transient solution is also distorted if the initial wave functions are computed from an ad-hoc discretization of the continuous boundary conditions (3.5) and (3.6). In stationary computations, spurious reflections due to an inconsistent discretization play a minor role but they become a major issue in transient simulations.

3.3.2 Second experiment: Time-dependent applied voltage

For the second numerical experiment, we consider a time-dependent applied voltage. The conduction current density is no longer constant but the total current density is expected to be conserved. We recall that the total current density $J_{\mathrm{tot}} = J_{\mathrm{cond}} + \partial D/\partial t$ is the sum of the conduction current density J_{cond} and the displacement current density $\partial D/\partial t$. Here D denotes the electric displacement field which is related to the electric field E by $D = \epsilon_0 \epsilon_r E$. Indeed, replacing the electric field by the negative gradient of the potential we obtain

$$\frac{\partial D}{\partial t} = -\frac{\epsilon_0 \epsilon_r}{e} \frac{\partial}{\partial t} \nabla V_{\text{self}}.$$

The temporal and spatial derivatives are approximated using centered finite differences. Ampère's circuital law $\nabla \times H = J_{\text{tot}}$ for the magnetic field strength H yields

$$\operatorname{div} J_{\text{tot}} = \operatorname{div}(\nabla \times H) = 0,$$

and hence, in one space dimension, J_{tot} is constant in space.

The following simulation demonstrates that the total current density is a conserved quantity in the discrete system as well. First, we compute the equilibrium state using an applied voltage of $U = 0\,\text{V}$. This solution is then propagated using a raised cosine function for the applied voltage

$$U(t) = \frac{U_0}{2}\left(1 - \cos\frac{2\pi t}{T}\right), \quad 0 \le t \le 1\,\text{ps},$$

where $U_0 = 0.25\,\text{V}$ and $T = 2\,\text{ps}$. At later times, $t \ge 1\,\text{ps}$, $U(t) = U_0$ is kept constant. Conduction, displacement, and total current density at different times are depicted in the left column of Figure 3.7. As can be seen, the total current density is perfectly conserved at all considered times. The change of the charge density $\partial\rho/\partial t$ is illustrated in the right column of Figure 3.7. In our model, ρ is given by $\rho = e\,(n_D - n)$.

The time-dependence of the total current density in response to the applied voltage is shown in Fig. 3.8. We can identify three different regions in the temporal behavior, each of which is governed by a different physical mechanism.

Region I: Capacitive behavior. When the applied voltage increases during the first picosecond, the resonant tunneling diode behaves mainly like a parallel plate capacitor. This can be clearly seen in the top left panel of Figure 3.7. In the region of the double barrier, the displacement current gives the dominant contribution to the total current, whereas the conduction current is small. The top right panel of Figure 3.7 shows a build-up of negative charge before the left barrier and of positive charge after the right barrier. The formation of opposite charges on the two sides of the double barrier results in the formation of an electric field between the two regions of opposite charge density. This field is necessary to accomodate the externally applied voltage. Figure 3.8 shows that the current closely follows the time derivative of the applied voltage:

$$J_{\text{cond}} \approx C\frac{dU}{dt} = \frac{\pi C U_0}{T} \sin\left(\frac{2\pi t}{T}\right).$$

This expression allows us to estimate the apparent capacitance C. The maximum current density occurring at $t = T/4 = 0.5\,\text{ps}$ takes approximately the value $1.2 \cdot 10^9\,\text{Am}^{-2}$. We compute $C = TJ/\pi U_0 = 3.06 \cdot 10^{-3}\,\text{Fm}^{-2}$. Equating this value to

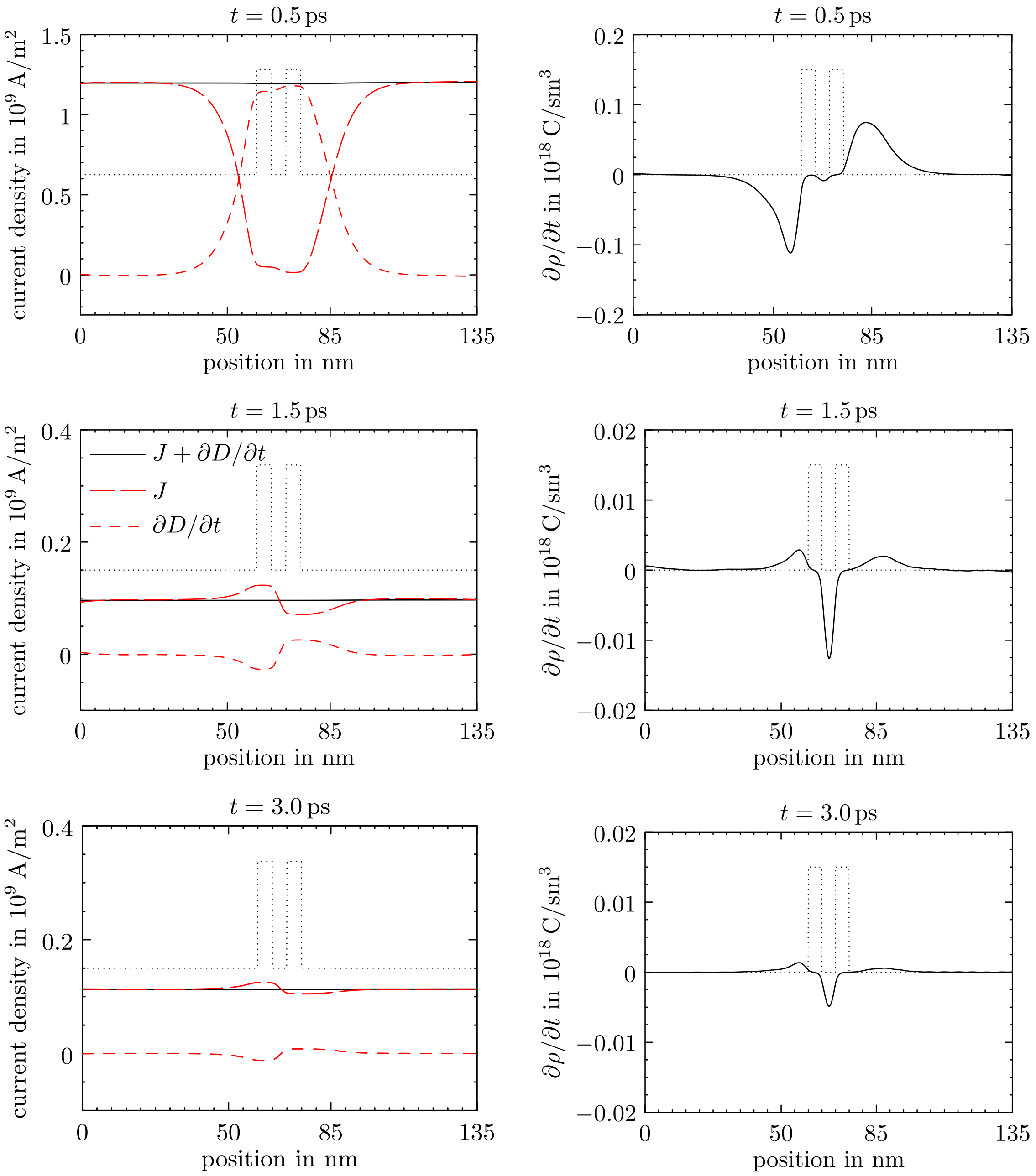

Figure 3.7: Left column: Total current density $J_{\mathrm{tot}} = J_{\mathrm{cond}} + \partial D/\partial t$, conduction current density $J := J_{\mathrm{cond}}$, and displacement current density $\partial D/\partial t$ versus position at different times. Right column: Temporal variation $\partial\rho/\partial t$ of the charge density versus position.

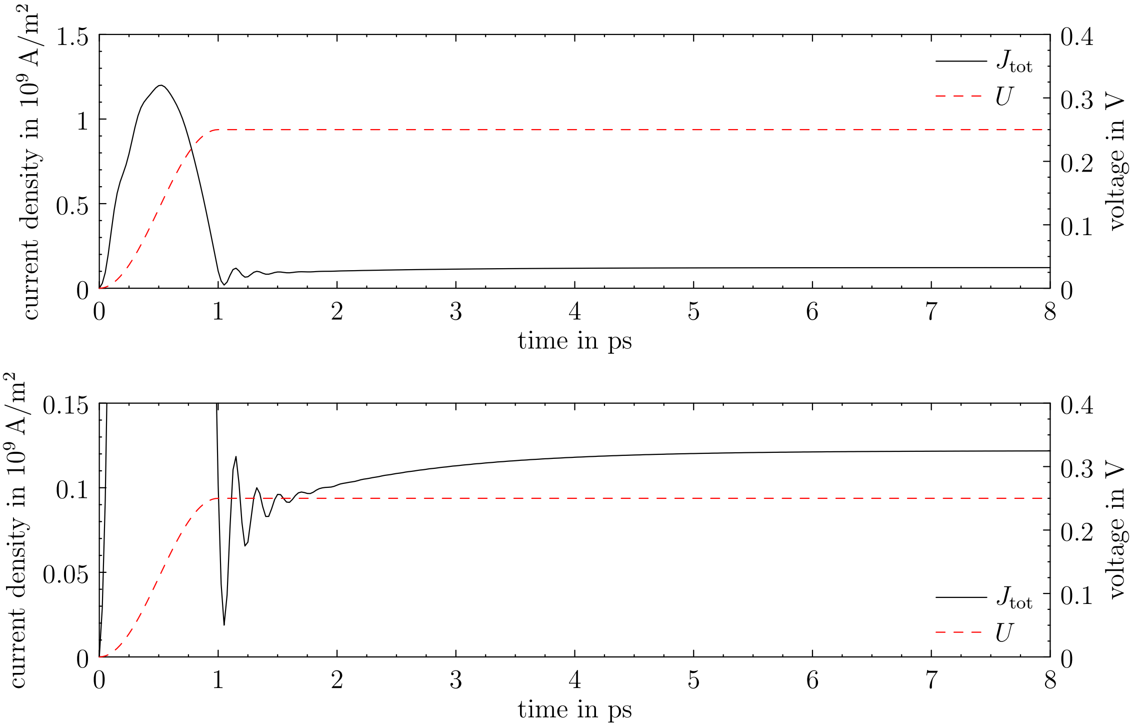

Figure 3.8: Applied voltage and total current density versus time in different scalings.

the parallel plate capacitance, $C = \varepsilon_0\varepsilon_r/d$, we find the average separation of the opposite charge densities to be $d = 33.1\,\mathrm{nm}$.

Region II: Plasma oscillations. During the second picosecond, the current density shows a strongly damped oscillation. From Figure 3.8, we estimate five oscillations to occur during one picosecond, which relates to a period of about 200 fs. It is believed that these are plasma oscillations which were excited by the rapidly changing applied voltage U. As soon as the transient phase of $U(t)$ is over and $U(t)$ is kept constant at U_0 for $t \geq 1\,\mathrm{ps}$, the excitation vanishes and the oscillations fade out quickly. As a rough estimate we calculate the plasma frequency ω_p for a classical electron system of uniform density:

$$\omega_p^2 = \frac{ne^2}{m^\star \varepsilon_0}.$$

Note that in the resonant tunneling diode the density is neither uniform nor is it governed by the classical equations of motion. Nevertheless, we may use this expression to estimate the order of magnitude of the time constant associated with this effect. Since plasma oscillations usually occur in the high-density regions of a device, we set $n = n_D^1 = 10^{24}\,\mathrm{m}^{-3}$ and obtain $\tau_p = 2\pi/\omega_p = 111.4\,\mathrm{fs}$. This value is of the same order as the 200 fs estimated above, which is a strong indication that the physical effect observed here is a plasma oscillation.

Region III: Charging of the quantum well. For $t > 2\,\mathrm{ps}$, an exponential increase in the current can be clearly observed in Figure 3.8. Below 2 ps we see a superposition of both the exponential current increase and the plasma oscillations. The origin of this effect can be understood from the right panels of Figure 3.7. Negative charge builds up in the quantum well. This charge results from electrons tunneling through the left barrier into the quantum well. In this context, we note that the temporal variation of the voltage between the left and right end points a_2 and a_5 of the double-barrier structure, respectively, follows closely the variation of the applied voltage U and hence, it is practically constant for $t > 1\,\mathrm{ps}$ (see Figure 3.9). The rate $|\partial\rho/\partial t|$ decreases with time as can be seen by the snapshots at $t = 1.5\,\mathrm{ps}$ and $t = 3\,\mathrm{ps}$. We calculate the number of electrons residing in the quantum well:

$$N(t) := \int_{a_2}^{a_5} n(x,t)\,dx.$$

Since the charging process is expected to show an exponential time dependence, we assume the following exponential law for $N(t)$ and extract the free parameters τ and N_∞:

$$N(t) = N_\infty + (N(t_1) - N_\infty)\,e^{-(t-t_1)/\tau}.$$

In Figure 3.9, the difference $|N(t) - N_\infty|$ is plotted, which decays to zero with an extracted time constant of $\tau = 1.25\,\mathrm{ps}$. This time scale is related to the life time of a quasi-bound state. At $U = 0.25\,\mathrm{V}$, the current-voltage characteristic

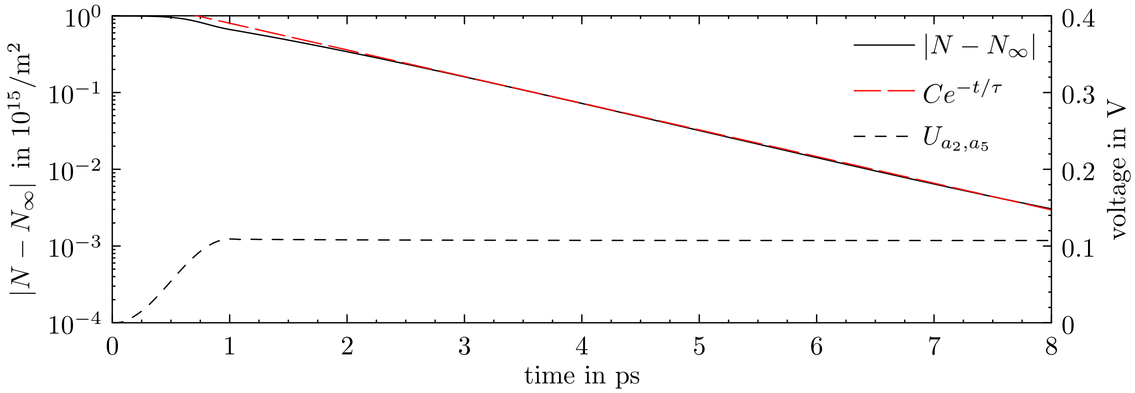

Figure 3.9: Number of electrons in the quantum well versus time. In Region III ($t \geq 2\,\mathrm{ps}$) this number clearly follows an exponential law. U_{a_2,a_5} denotes the temporal variation of the voltage between $x = a_2$ and $x = a_5$.

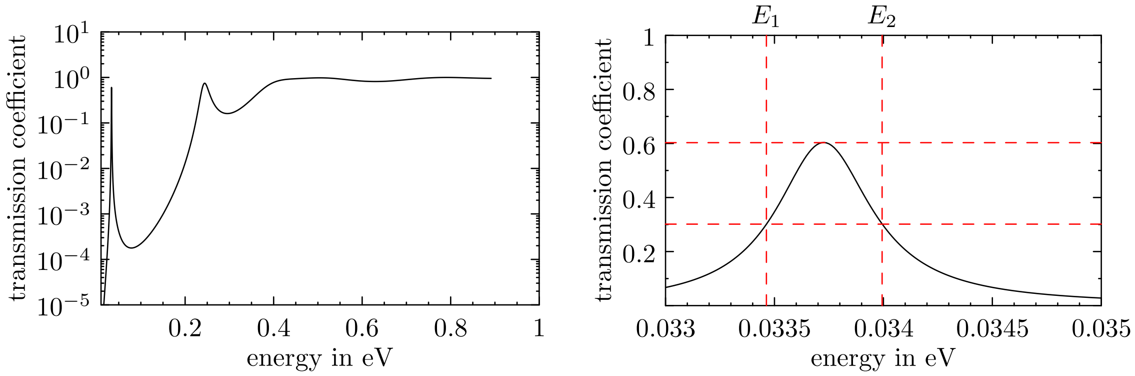

Figure 3.10: Transmission coefficient of the double-barrier structure at $U = 0.25\,\mathrm{V}$ in different scalings.

has its first maximum, which means that the first resonant state in the quantum well is carrying the current. The life time of this resonant state can be extracted from the width of the resonance peak in the transmission coefficient. Figure 3.10 depicts the transmission coefficient of the double-barrier structure at $U = 0.25\,\mathrm{V}$. The transmission coefficient is defined as the ratio between the transmitted and the incident probability current density j_{trans} and j_{inc}. In terms of the amplitude and the wavenumber of the transmitted and the incident wave, it reads:

$$\frac{|j_{\mathrm{trans}}|}{|j_{\mathrm{inc}}|} = \frac{|A_{\mathrm{trans}}|^2 k_{\mathrm{trans}}}{|A_{\mathrm{inc}}|^2 k_{\mathrm{inc}}}.$$

Extracting $\triangle E$, the half width at half maximum of the first transmission peak, the life time of the resonant state can be estimated as follows [49]:

$$\tau = \frac{\hbar}{2\triangle E}.$$

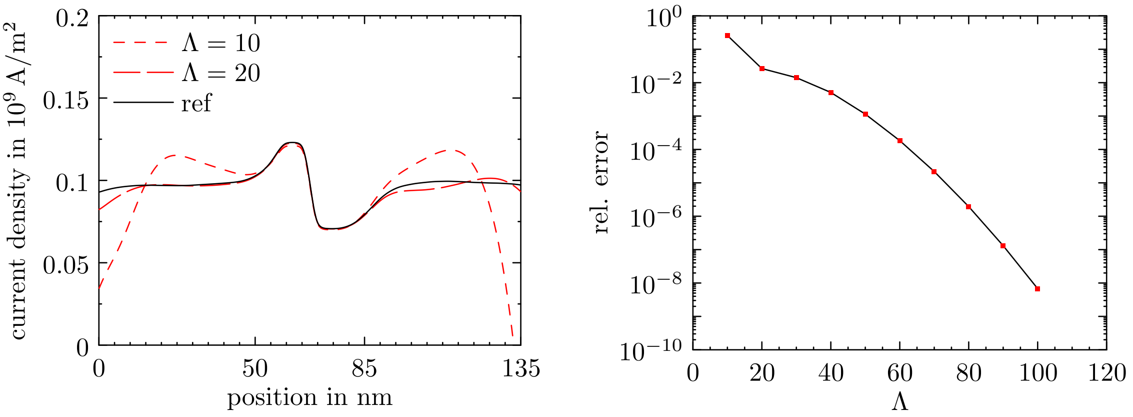

Figure 3.11: Conduction current density at $t = 1.5\,\mathrm{ps}$ (left) and relative ℓ^2-error for increasing Λ (right).

At $U = 0.25\,\mathrm{V}$ we find $2\triangle E = 5.31 \cdot 10^{-4}\,\mathrm{eV}$ and thus $\tau = 1.24\,\mathrm{ps}$. This value is very close to the time constant of $\tau = 1.25\,\mathrm{ps}$ extracted from the exponential charge increase in the quantum well, which is the cause for the observed exponential current increase.

3.3.3 Third experiment: Convergence in Λ

Finally, we study the convergence of the complete transient algorithm detailed in Section 3.2.3 with respect to the parameter Λ which appears in the context of the fast evaluation of the discrete convolution terms. For this purpose, we repeat the last experiment with different values of Λ. We compare the results with those obtained from the algorithm which uses the discrete transparent boundary conditions with the exact convolutions (3.26)–(3.27). Since the computation of the reference solution is rather expensive, we restrict the experiment to the final time $t = 1.5\,\mathrm{ps}$. The conduction current densities at $t = 1.5\,\mathrm{ps}$ for two different values of Λ and for the reference solution are depicted in Figure 3.11 (left). The relative error in the ℓ^2-norm for increasing values of Λ is shown in Figure 3.11 (right). We observe that the relative error decreases exponentially fast. Thus, a relatively small value of Λ yields practically the same results (at dramatically reduced numerical costs) as if the discrete transparent boundary conditions are evaluated exactly.

3.4 Circuit simulations

In this section, we simulate a high-frequency oscillator consisting of a voltage source U_e, a resistor with resistance R, an inductor with inductance L, a capacitor with capacity C, and a resonant tunneling diode RTD; see Figure 3.12. Each element of

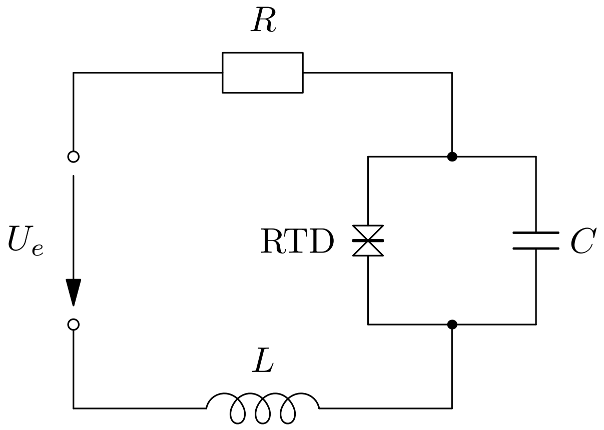

Figure 3.12: High-frequency oscillator containing the resonant tunneling diode RTD.

the circuit yields one current-voltage relationship,

$$U_R = RI_R, \quad U_L = L\dot{I}_L, \quad I_C = C\dot{U}_C, \quad I_{\mathrm{RTD}} = f(U_{\mathrm{RTD}}). \tag{3.31}$$

The last expression is to be understood as follows. Given the applied voltage U_{RTD} at the tunneling diode, the current $I_{\mathrm{RTD}}(t) = AJ_{\mathrm{tot}}(t)$ is computed from the solution of the time-dependent Schrödinger-Poisson system. Here, $A = 10^{-11}\,\mathrm{m}^2$ is the cross-sectional area of the diode and J_{tot} is the total current density. In the simulations we use $R = 5\,\Omega$, $L = 50\,\mathrm{pH}$, and $C = 10\,\mathrm{fF}$.

According to the Kirchhoff circuit laws, we have

$$U_e = U_R + U_{\mathrm{RTD}} + U_L, \quad U_{\mathrm{RTD}} = U_C, \quad I_L = I_R, \quad I_L = I_{\mathrm{RTD}} + I_C. \tag{3.32}$$

Combining (3.31) and (3.32), we find

$$\begin{aligned} C\dot{U}_{\mathrm{RTD}} &= C\dot{U}_C = I_C = I_L - I_{\mathrm{RTD}}, \\ L\dot{I}_L &= U_L = U_e - U_R - U_{\mathrm{RTD}} = U_e - RI_R - U_{\mathrm{RTD}} = U_e - RI_L - U_{\mathrm{RTD}}. \end{aligned}$$

Consequently, we obtain a system of two coupled ordinary differential equations,

$$\frac{d}{dt}\begin{pmatrix} U_{\mathrm{RTD}} \\ I_L \end{pmatrix} = \begin{pmatrix} 0 & \frac{1}{C} \\ -\frac{1}{L} & -\frac{R}{L} \end{pmatrix} \begin{pmatrix} U_{\mathrm{RTD}} \\ I_L \end{pmatrix} + \begin{pmatrix} -\frac{1}{C} I_{\mathrm{RTD}} \\ \frac{1}{L} U_e(t) \end{pmatrix}. \tag{3.33}$$

The time-step size $\triangle t$ is very small compared to the time scale of the variation of the potential energy and the variation of the current flowing through the diode. Hence, using the same time step for the time integration of (3.33), we can resort to an explicit time-stepping method. We choose the simplest one, the explicit Euler method. Alternatively, one may employ an implicit method, but we observed that both methods yield essentially the same results.

First circuit simulation. In the first simulation, the RTD solver is initialized with the steady state corresponding to $U_{\mathrm{RTD}}(t) = 0$ for all $t \leq 0$. The external

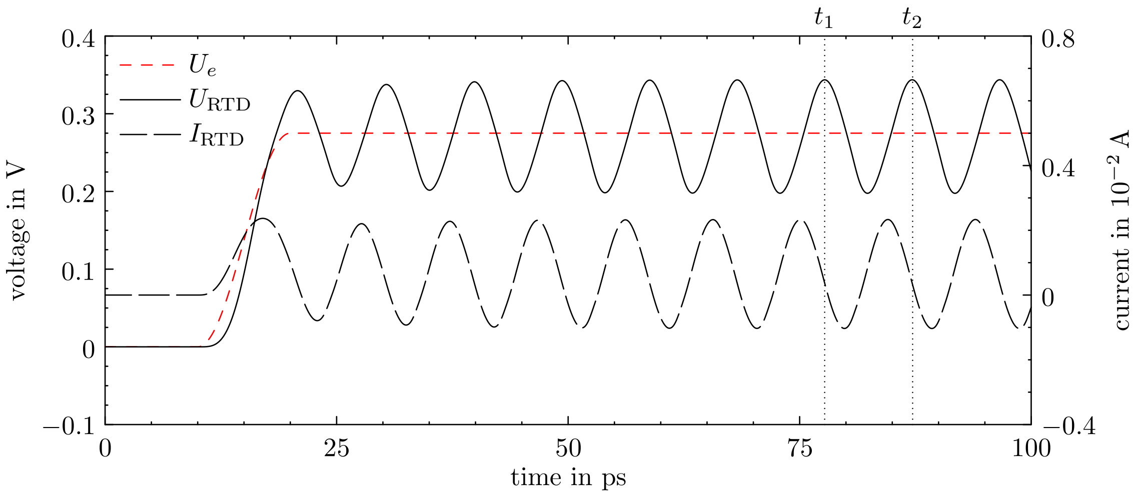

Figure 3.13: First circuit simulation: Voltage U_{RTD} and current I_{RTD} through the resonant tunneling diode versus time.

voltage U_e is assumed to be zero for $t \leq 0$, and the initial conditions for (3.33) are $U_{\mathrm{RTD}}(0) = 0$ and $I_L(0) = 0$. For $t \in [10, 20]$ ps, the external voltage is increased smoothly to 0.275 V and then kept constant (see Figure 3.13). This value is between the voltages where the stationary current density reaches its local maximum and minimum (see Figure 3.4). The time evolution of the voltage and the current at the RTD are depicted in Figure 3.13. It is clearly visible that the system starts to oscillate. Furthermore, the potential energy, electron density, current densities, and the temporal variation of the total charge $\partial\rho/\partial t$ are shown in Figure 3.14 for four different times from the interval $[t_1 = 77.7, t_2 = 87.2]$ ps, which covers exactly one oscillation. Around 2 ps after the beginning of the period, the electron density within the quantum well in $[65, 70]$ nm becomes minimal (first row). After some time, we observe a build-up of negative charge in the quantum well with $\partial\rho/\partial t < 0$ (second row). At about $t = 84.6$ ps the electron density reaches its maximum value (third row). Subsequently, the electrons leave the quantum well again and $\partial\rho/\partial t > 0$ in $[65, 70]$ nm (fourth row). The frequency of the oscillations is approximately 105 GHz which corresponds qualitatively to frequencies observed in standard double-barrier tunneling diodes [21].

Second circuit simulation. In this experiment, the external voltage U_e is kept fixed for all times. At times $t \leq 0$, the circuit contains the voltage source, resistor, and RTD only. We initialize the transient Schrödinger-Poisson solver with the steady state corresponding to $U_{\mathrm{RTD}}(t) = 0.275$ V for all $t \leq 0$. To compensate for the voltage drop at the resistor, the external voltage is set to

$$U_e(t) = RI_{\mathrm{RTD}}(t) + U_{\mathrm{RTD}}(t), \quad t \leq 0.$$

At time $t = 0$, the capacitor and inductor are added to the circuit. In order to avoid discontinuities in the voltages, we charge the capacitor with the same voltage

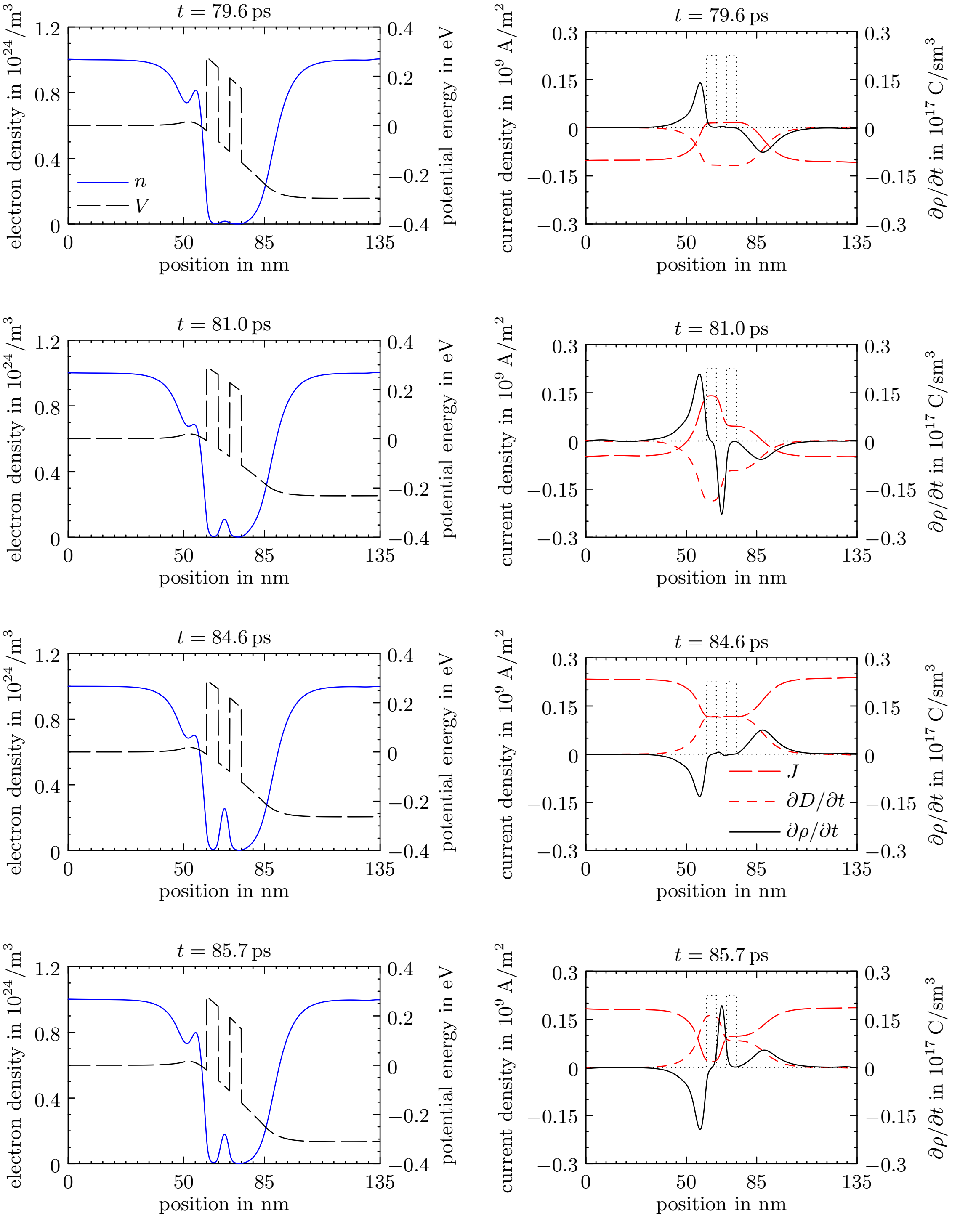

Figure 3.14: First circuit simulation: Electron density, potential energy, current densities, and variation of the electron density versus position in the RTD at four different times.

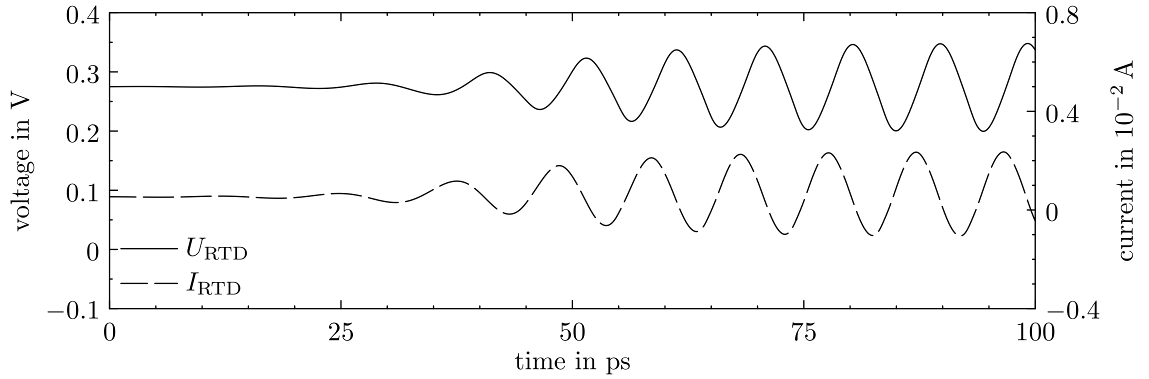

Figure 3.15: Second circuit simulation: Applied voltage and current at the resonant tunneling diode versus time.

which is applied at the RTD before the switching takes place, $U_C(t) = U_{\mathrm{RTD}}(t)$ for $t \leq 0$. For similar reasons, we set the current flowing through the inductor to the current flowing through the RTD, $I_L(t) = I_{\mathrm{RTD}}(t)$ for $t \leq 0$. This configuration corresponds to an equilibrium state. Therefore, one would expect that the system remains in its initial state for all time. However, the equilibrium is unstable and a small perturbation will drive the system out of equilibrium. In fact, numerical inaccuracies suffice to start the oscillator. However, we accelerate the transient phase by perturbing $I_L(t)$ by the value $5 \cdot 10^{-6}$ A for $t \leq 0$. The numerical result is presented in Figure 3.15. The simulation took less than 4 hours computing time on an Intel Core 2 Quad Q9550 CPU @ 2.83GHz × 4.

Chapter 4

Perfectly Matched Layers versus discrete transparent boundary conditions in quantum device simulations

Chapter 4 is organized as follows. Section 4.1 covers scattering states, wave packets and transient scattering states in one space dimension. We detail the discretization of the Schrödinger equation and show how to realize open boundary conditions using Perfectly Matched Layers (PML). Moreover, we recall the numerical methods which are based on discrete transparent boundary conditions (DTBC) and are used to compute reference solutions. In Section 4.2, we consider quantum waveguide devices. The derivation of DTBC for the stationary and transient problem is explained in detail. Besides, we show that PML provide an efficient alternative which can be implemented more easily. Section 4.3 is devoted to the Aharonov-Bohm effect in the stationary and transient regime.

4.1 One-dimensional simulations

4.1.1 Scattering states

Scatterings states play a leading role in the context of quantum device simulations. In one-dimensional calculations they represent a beam of electrons injected at the left or right lead of the device. This beam of particles is identified with a wave function which solves the stationary Schödinger equation

$$-\frac{\hbar^2}{2m^\star}\frac{d^2}{dx^2}\phi(x) + V(x)\phi(x) = E\phi(x), \quad x \in \mathbb{R}, \tag{4.1}$$

subject to the boundary condition that the incoming wave function is a plane wave. A portion of the incoming wave is reflected and a portion is transmitted through the device region described by the potential energy V. In the above equation, E denotes the total energy and $m^\star$ denotes the effective mass of the electrons in the semiconductor. In all subsequent simulations we set $m^\star = 0.067\,m_e$ corresponding to the effective mass of electrons in GaAs with m_e being the electron mass at rest. We further assume that the device in $(0, L)$ is connected to the semi-infinite leads $(-\infty, 0]$ and $[L, \infty)$. In the exterior domain the potential energy is assumed to be constant, i.e., $V(x) = V_\ell$ for $x \leq 0$ and $V(x) = V_r$ for $x \geq L$. Without loss of generality we set $V_\ell = 0$ and $V_r = -eU$, where e denotes the elementary charge and U is the applied voltage at the right contact. The total energy of an electron injected at the left contact is given by $E(k) = \hbar^2 k^2/(2m^\star)$ with $k > 0$ being the electrons wave number in the left lead. The incoming electron is represented by a plane wave $\exp(ikx)$ travelling to the right. Transparent boundary conditions are given in (3.5). In the notation of this chapter they read

$$\phi'(0) + ik\phi(0) = 2ik, \quad \phi'(L) = i\sqrt{2m^\star(E - V_r)/\hbar^2}\,\phi(L). \tag{4.2}$$

Electrons injected at the right contact traveling to the left are treated analogously (compare Section 3.1.1).

Discrete transparent boundary conditions. A symmetric second-order finite difference discretization of the stationary Schrödinger equation (4.1) on the equidistant grid $x_j = j\triangle x$, $j \in \mathbb{Z}$, with $x_J = L$ and $\triangle x > 0$ is given by

$$-\frac{\hbar^2}{2m^\star}\frac{\phi_{j-1} - 2\phi_j + \phi_{j+1}}{(\triangle x)^2} + V_j\phi_j = E\phi_j. \tag{4.3}$$

As before, the potential energy in the semi-infinite leads is assumed to be constant, i.e., $V_j = 0$ for $j \leq 0$ and $V_j = -eU$ for $j \geq J$. We seek for a solution of (4.3) restricted to the grid

$$X_{\mathrm{DTBC}} = \{x_j = j\triangle x,\ j = 0, ..., J\}, \tag{4.4}$$

and hence we have to specify open boundary conditions at $x_0 = 0$ and $x_J = L$. In order to avoid spurious oscillations in the numerical solution we employ DTBC which are explained in Section 3.1.2. Since the notation in this chapter is slightly different we recall the most important formulas.

In the semi-infinite leads the potential energy is assumed to be constant and consequently (4.3) admits two solutions of the form

$$\phi_j = \alpha_{\ell,r}^j, \tag{4.5}$$

where

$$\begin{aligned}\alpha_{\ell,r} =& 1 - \frac{m^\star(E(k) - V_{\ell,r})(\triangle x)^2}{\hbar^2}\\ &\pm i\sqrt{\frac{2m^\star(E(k) - V_{\ell,r})(\triangle x)^2}{\hbar^2} - \frac{(m^\star)^2(E(k) - V_{\ell,r})^2(\triangle x)^4}{\hbar^4}}\end{aligned}$$

depends on the kinetic energy $E^{\mathrm{kin}}_{\ell,r}(k) = E(k) - V_{\ell,r}$ in the left or right lead. For a wave function injected at the left contact travelling to the right the solution to (4.3) is a superposition of an incoming and a reflected discrete plane wave, $\phi_j = A\alpha_\ell^j + B\alpha_\ell^{-j}$ in the left contact, and a transmitted wave $\phi_j = C\alpha_r^j$ in the right contact. The amplitude of the incoming discrete plane wave in the left lead is set to $A = 1$. Eliminating B and C yields the desired DTBC

$$\phi_0 - \alpha_\ell \phi_1 = 1 - \alpha_\ell^2, \quad \alpha_r \phi_{J-1} - \phi_J = 0. \tag{4.6}$$

Here we implicitly assumed $V_j = 0$ for $j \le 1$ and $V_j = -eU$ for $j \ge J-1$ but we could just as easily state the boundary conditions in terms of ϕ_{-1}, ϕ_0 and ϕ_J, ϕ_{J+1} (see Section 3.1.2). However, this requires to extend the grid X_{DTBC} temporarily by the grid points x_{-1} and x_{J+1}. On the discrete level of equation (4.3) we need to replace the continuous E–k–relation

$$k = \sqrt{2m^\star E^{\mathrm{kin}}}/\hbar \tag{4.7}$$

by the discrete E–k–relation

$$k = \arccos\left(1 - m^\star(\triangle x/\hbar)^2 E^{\mathrm{kin}}\right)/\triangle x. \tag{4.8}$$

Plane waves injected at the right contact traveling to the left are treated analogously. For further details we refer to Section 3.1.2.

Perfectly Matched Layers. As an alternative to DTBC we consider PML which were originally developed for the Maxwell equations [17]. In fact, PML can be seen as the result of a complex coordinate transformation [25]. This idea has been applied to a wide range of linear and nonlinear wave problems in unbounded domains. PML have been applied to the nonlinear (and linear) time-dependent Schrödinger equation in [80] . We employ the same complex coordinate transformation

$$x \mapsto x + e^{i\pi/4} \int^x \sigma(x')\, dx', \tag{4.9}$$

with the absorption function

$$\sigma(x) = \begin{cases} \sigma_0(x_\ell^\star - x)^p, & \text{if } x < x_\ell^\star, \\ 0, & \text{if } x_\ell^\star \le x \le x_r^\star, \\ \sigma_0(x - x_r^\star)^p, & \text{if } x_r^\star < x. \end{cases}$$

This coordinate transformation corresponds to the substitution

$$\frac{d}{dx} \to c(x)\frac{d}{dx}, \quad c(x) := \frac{1}{1 + e^{i\pi/4}\sigma(x)}, \tag{4.10}$$

such that the stationary Schrödinger-PML equation reads

$$-\frac{\hbar^2}{2m^\star} c(x)\frac{d}{dx}\left(c(x)\frac{d}{dx}\phi(x)\right) + V(x)\phi(x) = E\phi(x) \tag{4.11}$$

which agrees with the original stationary Schrödinger equation (4.1) for $x \in [x_\ell^\star, x_r^\star]$ and hence we require that $[0, L] \subset [x_\ell^\star, x_r^\star]$. Outside of $[x_\ell^\star, x_r^\star]$ propagating waves are damped exponentially fast

$$\exp(ikx) \to \exp(ikx) \exp\left(ike^{i\pi/4} \int^x \sigma(x')\, dx'\right) \tag{4.12}$$

with their distance to the points $x_{\ell,r}^\star$. Denoting the thickness of the PML with d_{PML} the computational domain is given by $[x_\ell^\star - d_{\mathrm{PML}}, x_r^\star + d_{\mathrm{PML}}]$. We use cubic absorption functions ($p = 3$), which we found give slightly better results than the quadratic functions used in [80]. Absorption functions need not necessarily be power functions. As an alternative absorption functions with singularities at the boundaries of the computational domain are proposed in [18].

A wave propagating through a PML is expected to be practically zero when it hits the boundary of the computational domain, provided d_{PML} is sufficiently large. Therefore, Dirichlet BCs are imposed at the boundary points $x_\ell^\star - d_{\mathrm{PML}}$ and $x_r^\star + d_{\mathrm{PML}}$. Just as well it is possible to impose Neumann BCs. In fact, we will see that Neumann BCs are slightly advantageous in the context of scattering and transient scattering state simulations.

Propagating waves with different wave numbers k experience different attenuation according to equation (4.12). It is easily possible to obtain a uniform attenuation independent of the wave number if the inverse of k is included into the absorption function. This strategy is typically employed in stationary wave problems [18, 71]. However, since the main focus of this chapter are wave packet, and in particular transient scattering state simulations, the strategy is different. Any wave packet can be thought of as a superposition of propagating waves of different energy, i.e., different wave number k. For that reason, we seek for PML which are able to treat all incoming waves simultaneously. In this spirit, the factor $\exp(i\pi/4)$ appearing in (4.9) is meant to give a good effect on average as explained in [80]. In any case, the thickness of the PML will be comparatively large as they are not optimized to absorb waves of a single energy. In the simulations below we choose the thickness of the PML first. Then we choose the absorption strength factor σ_0 such that the numerical error becomes small for a given range of energies.

We use symmetric finite difference formulas to approximate the modified spatial derivative

$$c(x)\frac{d}{dx}\left(c(x)\frac{d}{dx}\right) = c(x)c'(x)\frac{d}{dx} + c^2(x)\frac{d^2}{dx^2}$$

in (4.11). Approximations of 2nd, 4th and 6th order read

$$\tilde{D}_x^{2,\mathrm{2nd}}\phi_j := c(x_j)c'(x_j)D_x^{1,\mathrm{2nd}}\phi_j + c^2(x_j)D_x^{2,\mathrm{2nd}}\phi_j, \tag{4.13a}$$

$$\tilde{D}_x^{2,\mathrm{4th}}\phi_j := c(x_j)c'(x_j)D_x^{1,\mathrm{4th}}\phi_j + c^2(x_j)D_x^{2,\mathrm{4th}}\phi_j, \tag{4.13b}$$

$$\tilde{D}_x^{2,\mathrm{6th}}\phi_j := c(x_j)c'(x_j)D_x^{1,\mathrm{6th}}\phi_j + c^2(x_j)D_x^{2,\mathrm{6th}}\phi_j, \tag{4.13c}$$

wherein

$$D_x^{1,\text{2nd}}\phi_j := (-\phi_{j-1} + \phi_{j+1})/(2\triangle x), \tag{4.14a}$$

$$D_x^{1,\text{4th}}\phi_j := (\phi_{j-2} - 8\phi_{j-1} + 8\phi_{j+1} - \phi_{j+2})/(12\triangle x), \tag{4.14b}$$

$$D_x^{1,\text{6th}}\phi_j := (-\phi_{j-3} + 9\phi_{j-2} - 45\phi_{j-1} + 45\phi_{j+1} - 9\phi_{j+2} + \phi_{j+3})/(60\triangle x), \tag{4.14c}$$

and

$$D_x^{2,\text{2nd}}\phi_j := (\phi_{j-1} - 2\phi_j + \phi_{j+1})/(\triangle x)^2, \tag{4.15a}$$

$$D_x^{2,\text{4th}}\phi_j := (-\phi_{j-2} + 16\phi_{j-1} - 30\phi_j + 16\phi_{j+1} - \phi_{j+2})/(12(\triangle x)^2), \tag{4.15b}$$

$$\begin{aligned} D_x^{2,\text{6th}}\phi_j := (&2\phi_{j-3} - 27\phi_{j-2} + 270\phi_{j-1} - 490\phi_j + 270\phi_{j+1} - 27\phi_{j+2} \\ &+ 2\phi^{(n)}_{j+3})/(180(\triangle x)^2), \end{aligned} \tag{4.15c}$$

are needed frequently in the rest of this chapter. We further introduce the equidistant grid

$$X_{\text{PML}} := \{x_j = x_\ell^\star - d_{\text{pml}} + j\triangle x,\ j = 0, ..., J_{\text{PML}}\} \tag{4.16}$$

with $x_{J_{\text{PML}}} = x_r^\star + d_{\text{PML}}$ and $X_{\text{DTBC}} \subset X_{\text{PML}}$. Then the discrete stationary Schrödinger-PML equation reads

$$-\frac{\hbar^2}{2m^\star}\tilde{D}_x^2\,\phi_j + V_j\phi_j = E\phi_j, \quad \tilde{D}_x^2 \in \{\tilde{D}_x^{2,\text{2nd}}, \tilde{D}_x^{2,\text{4th}}, \tilde{D}_x^{2,\text{6th}}\}. \tag{4.17}$$

At the boundaries of X_{PML} we impose homogeneous Dirichlet or Neumann BCs. In the latter case $\tilde{D}_x^2$ is modified accordingly.

We still need to specify how to realize an incoming plane wave at one of the device contacts. Without loss of generality we consider the left contact only. Moreover, we restrict ourselves to the second order discretization $\tilde{D}_x^2 = \tilde{D}_x^{2,\text{2nd}}$. Let $x_{j_0} = 0$ denote the boundary of the left contact. The wave function in the left contact is given by the sum of an incoming and a reflected wave function $\phi_j = \phi_j^{\text{inc}} + \phi_j^{\text{refl}}$. In the numerical implementation we eliminate ϕ_j^{inc} in the left lead. Thus, to realize an incoming plane wave at x_{j_0} the finite difference equations for $j_0 - 1$ and j_0 need to be modified as follows:

$$-\frac{\hbar^2}{2m^\star}\frac{\phi_{j_0-2} - 2\phi_{j_0-1} + (\phi_{j_0} - \phi_{j_0}^{\text{inc}})}{(\triangle x)^2} + V_{j_0-1}\phi_{j_0-1} = E\phi_{j_0-1}, \tag{4.18a}$$

$$-\frac{\hbar^2}{2m^\star}\frac{(\phi_{j_0-1} + \phi_{j_0-1}^{\text{inc}}) - 2\phi_{j_0} + \phi_{j_0+1}}{(\triangle x)^2} + V_{j_0}\phi_{j_0} = E\phi_{j_0}. \tag{4.18b}$$

In this regard it is noted that the absorption function of the left lead is only active for $x_j \leq x_\ell^\star$. Since we ensure that $x_\ell^\star$ is a little smaller than x_{j_0} the complex function c does not show up in (4.18). Therefore, the final numerical problem becomes

$$-\frac{\hbar^2}{2m^\star}\tilde{D}_x^{2,\text{2nd}}\phi_j + (V_j - E)\phi_j = b_j, \quad j = 0, ..., J_{\text{PML}},$$

where

$$b_j = \begin{cases} -\left(\hbar^2/(2m^\star(\triangle x)^2)\right)\phi_{j_0}^{\mathrm{inc}} & \text{for } j = j_0 - 1, \\ +\left(\hbar^2/(2m^\star(\triangle x)^2)\right)\phi_{j_0-1}^{\mathrm{inc}} & \text{for } j = j_0, \\ 0 & \text{else.} \end{cases}$$

If $\tilde{D}_x^2 = \tilde{D}_x^{2,4\mathrm{th}}$ or $\tilde{D}_x^2 = \tilde{D}_x^{2,6\mathrm{th}}$ we proceed in a similar way. However, due to the extended finite difference stencils, the vector b involves four or six non-zero entries, respectively.

The incoming plane wave is given by $\phi_j^{\mathrm{inc}} = e^{ikj\triangle x}$. In case of the second-order discretization the wave number is related to the kinetic energy by the discrete E–k–relation (4.8). In case of the higher-order discretizations we simply use (4.7) since the corresponding discrete k–E–relations can not easily be inverted and since the differences would be small anyhow.

Exact solutions for piecewise linear potentials. For piecewise linear potentials the scattering state problem can be solved exactly. If the potential energy is a constant $V(x) = V \neq E,\ x \in \mathbb{R}$ the solution to the stationary Schödinger equation

$$\frac{d^2}{dx^2}\phi(x) = -k^2\phi(x), \quad k = \begin{cases} \sqrt{2m(E-V)}/\hbar & \text{for } (E-V) \geq 0, \\ i\sqrt{2m(V-E)}/\hbar & \text{for } (E-V) < 0, \end{cases}$$

is given by a superposition of plane waves

$$\phi(x) = c_1 \exp(ikx) + c_2 \exp(-ikx). \tag{4.19}$$

For $V = E$ the solution is a linear function

$$\phi(x) = c_1 x + c_2. \tag{4.20}$$

In case of a linear potential $V_0 + \triangle V(x - a_0)/d,\ x \in \mathbb{R},\ \triangle V = V_1 - V_0 \neq 0$ and $d = a_1 - a_0 > 0$ the solution to the stationary Schrödinger equation

$$\frac{d^2}{d\tilde{x}^2}\tilde{\phi}(\tilde{x}) + \tilde{x}\tilde{\phi}(\tilde{x}) = 0$$

is a superposition of Airy functions

$$\phi(x) = \tilde{\phi}(\tilde{x}) = c_1 \operatorname{Ai}(-\tilde{x}(x)) + c_2 \operatorname{Bi}(-\tilde{x}(x)), \tag{4.21}$$

wherein we employed the coordinate transformation

$$\tilde{x}(x) = -\alpha\, 2m/\hbar^2\ \left[V_0 + \triangle V(x - a_0)/d - E\right], \ \alpha = \left(\hbar^2 d/(2m\triangle V)\right)^{2/3}.$$

As an example we consider the stationary Schrödinger equation for a ramp-like potential

$$V(x) = \begin{cases} 0 & \text{for } x < a_0, \\ ((x-a_0)/(a_1-a_0))\, V_1 & \text{for } a_0 \leq x < a_1, \\ V_1 & \text{for } x \geq a_1, \end{cases}$$

subject to the boundary condition that the incoming wave function at the left contact is a plane wave. Let $E_{\mathrm{kin}}^{\mathrm{inc}}$ denote the kinetic energy of the electron in the left lead ($x < a_0$). We further assume $E = E_{\mathrm{kin}}^{\mathrm{inc}} \neq V_1$. According to (4.19) and (4.21) the scattering state is given by

$$\phi(x) = \begin{cases} c_0 \exp(ik_0 x) + c_1 \exp(-ik_0 x) & \text{for } x < a_0, \\ c_2 \operatorname{Ai}(-\tilde{x}(x)) + c_3 \operatorname{Bi}(-\tilde{x}(x)) & \text{for } a_0 \leq x < a_1, \\ c_4 \exp(ik_1 x) + c_5 \exp(-ik_1 x) & \text{for } x \geq a_1. \end{cases}$$

Since $\phi \in C^1$ the coefficients $c_0, ..., c_5 \in \mathbb{C}$ are related to one another through $A_0(c_0, c_1)^\top = A_1(c_2, c_3)^\top$ and $A_2(c_2, c_3)^\top = A_3(c_4, c_5)^\top$, with the two-by-two matrices A_1, A_2, A_3 being defined as follows:

$$\begin{aligned} A_0 &= \begin{pmatrix} \exp(ik_0 a_0) & \exp(-ik_0 a_0) \\ ik_0 \exp(ik_0 a_0) & -ik_0 \exp(-ik_0 a_0) \end{pmatrix}, \\ A_1 &= \begin{pmatrix} \operatorname{Ai}(-\tilde{x}(a_0)) & \operatorname{Bi}(-\tilde{x}(a_0)) \\ -\operatorname{Ai}'(-\tilde{x}(a_0))\tilde{x}'(a_0) & -\operatorname{Bi}'(-\tilde{x}(a_0))\tilde{x}'(a_0) \end{pmatrix}, \\ A_2 &= \begin{pmatrix} \operatorname{Ai}(-\tilde{x}(a_1)) & \operatorname{Bi}(-\tilde{x}(a_1)) \\ -\operatorname{Ai}'(-\tilde{x}(a_1))\tilde{x}'(a_1) & -\operatorname{Bi}'(-\tilde{x}(a_1))\tilde{x}'(a_1) \end{pmatrix}, \\ A_3 &= \begin{pmatrix} \exp(ik_1 a_1) & \exp(-ik_1 a_1) \\ ik_1 \exp(ik_1 a_1) & -ik_1 \exp(-ik_1 a_1) \end{pmatrix}. \end{aligned}$$

We further define the matrix $M = A_0^{-1} A_1 A_2^{-1} A_3$ which yields

$$\begin{pmatrix} c_0 \\ c_1 \end{pmatrix} = \begin{pmatrix} m_{00} & m_{01} \\ m_{10} & m_{11} \end{pmatrix} \begin{pmatrix} c_4 \\ c_5 \end{pmatrix}.$$

Since there is no incident wave from the right contact we have $c_5 = 0$. Without loss of generality we set $c_0 = 1$. It follows $c_4 = c_0/m_{00}$ and $c_1 = m_{10} c_4$. The remaining coefficients are $(c_2, c_3)^\top = A_2^{-1} A_3 (c_4, c_5)^\top$. The case $E = E_{\mathrm{kin}}^{\mathrm{inc}} = V_1$ works analogously using the linear wave function (4.20) for $x \geq a_1$.

Simulations. We consider the ramp-like potential

$$V(x) = \begin{cases} 0 & \text{for } x < a_0, \\ -\left((x - a_0)/(a_1 - a_0)\right) eU & \text{for } a_0 \leq x < a_1, \\ -eU & \text{for } x \geq a_1, \end{cases} \tag{4.22}$$

with $a_0 = 40\,\mathrm{nm}$, $a_1 = 80\,\mathrm{nm}$ and an applied voltage of $U = -25\,\mathrm{mV}$; see Figure 4.1. The electrons are injected at the left contact traveling to the right. At the left contact the potential energy is zero and hence the energy of the incoming electrons is given by the kinetic energy only which is denoted by $E_{\mathrm{kin}}^{\mathrm{inc}}$. Figure 4.1 shows the real parts of scattering states computed with DTBC (dotted line) on the one hand and with PML (solid line) on the other. The device domain extends from 0 nm to

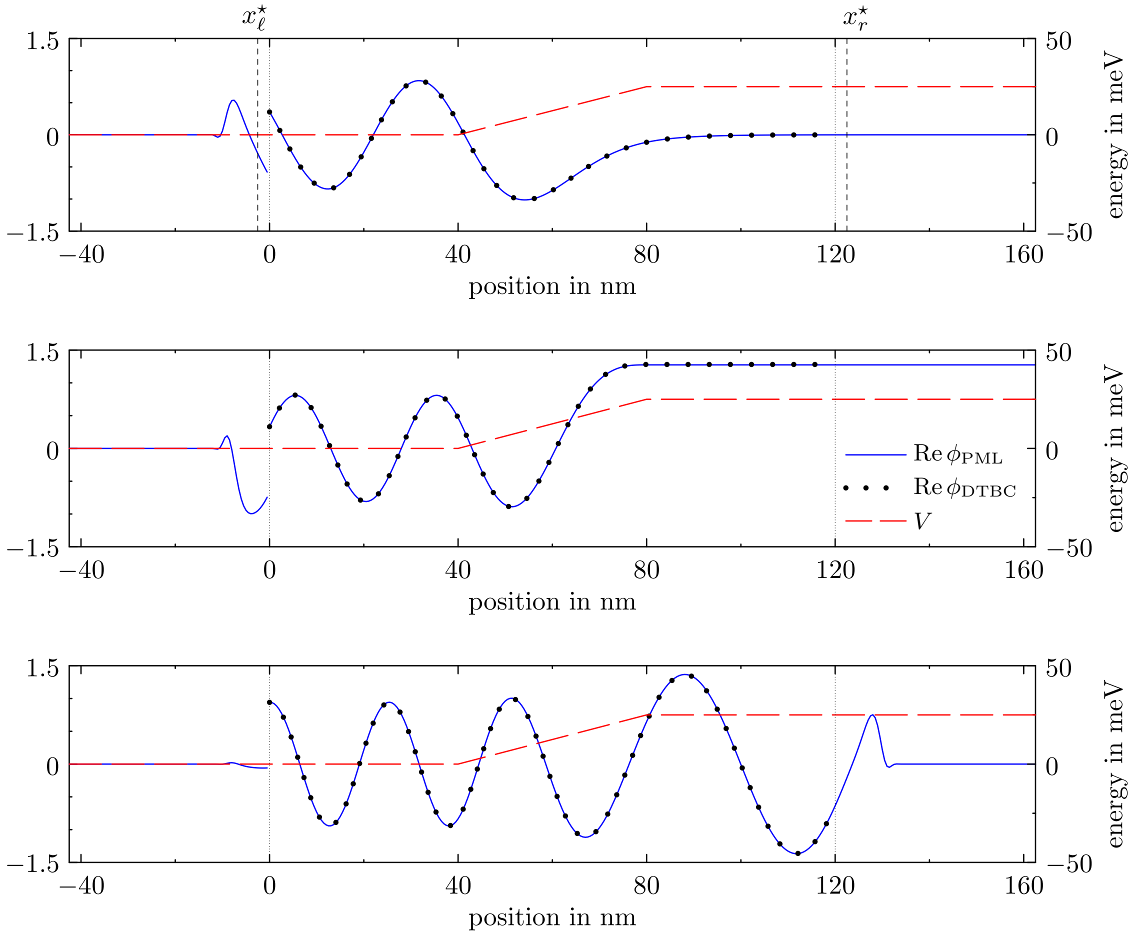

Figure 4.1: Scattering states for an electron injected at the left contact traveling to the right. The kinetic energy of the incoming electrons amounts to $E_{\mathrm{inc}}^{\mathrm{kin}} = 15\,\mathrm{meV}$ (top), $E_{\mathrm{inc}}^{\mathrm{kin}} = 25\,\mathrm{meV}$ (center) and $E_{\mathrm{inc}}^{\mathrm{kin}} = 35\,\mathrm{meV}$ (bottom). The applied voltage is given by $U = -25\,\mathrm{mV}$, i.e., the potential energy in the right lead amounts to $25\,\mathrm{meV}$. Moreover, $x_\ell^\star$ and $x_r^\star$ indicate the boundaries of the PML in the left and right lead, respectively.

$L = 120\,\mathrm{nm}$. The width of the PML amounts to $d_{\mathrm{PML}} = 40\,\mathrm{nm}$ and the absorption strength factor is $\sigma_0 = 0.02$. The beginning of the PML is indicated by the dashed lines below $x_\ell^\star$ and $x_r^\star$. The distances of $x_\ell^\star$ and $x_r^\star$ to the device domain are a few times the mesh size $\triangle x$ which ensures that the discretization inside the device domain is not altered by the PML. Unless stated otherwise, the simulations in this subsection are performed using homogeneous Neumann BCs at the end points of the PML. The mesh size is given by $\triangle x = 0.5\,\mathrm{nm}$. It is important to note that the 2nd-order discretization along with DTBC and the 2nd-order discretization using PML coincide exactly inside the device domain. Therefore it is particularly interesting two compare the results of these two methods. As can be seen from Figure 4.1 the scatterings states of both methods for different values of $E_{\mathrm{kin}}^{\mathrm{inc}}$ can hardly be distinguished. The first row in Figure 4.1 corresponds to $E_{\mathrm{kin}}^{\mathrm{inc}} = 15\,\mathrm{meV}$. Since the potential energy at the right contact amounts to $25\,\mathrm{meV}$ all incoming electrons are being reflected and then absorbed by the PML in the left contact. The discontinuity in the wave function at $x = 0\,\mathrm{nm}$ stems from the fact that the incoming plane wave in the left contact has been eliminated. The second graphics corresponds to the limiting case $E_{\mathrm{kin}}^{\mathrm{inc}} = 25\,\mathrm{meV}$. Electrons which reach the contact on the right-hand side loose all of their kinetic energy while they pass through the linearly increasing potential in $[40, 80]\,\mathrm{nm}$. Hence, the wave number becomes zero and according to (4.12) the PML in the right contact has no effect on the wave function. Nonetheless, we obtain a reasonable approximation due to the Neumann BC imposed at the boundary of the computational domain. However, the question arises of whether the PML will fail when $E_{\mathrm{inc}}^{\mathrm{kin}}$ is very near to this critical energy. This issue will be addressed below. The third graphics at the bottom of Figure 4.1 corresponds to $E_{\mathrm{kin}}^{\mathrm{inc}} = 35\,\mathrm{meV}$. In this case, almost the entire incoming wave function is being transmitted through the device region. The potential energy of the transmitted electrons is increased by $25\,\mathrm{meV}$. Accordingly the kinetic energy is decreased by the same amount, which results in a reduced wave number, or equivalently, in an increased wavelength.

We repeat the same numerical experiment, but this time we compute scattering states for the whole range of energies $E_{\mathrm{kin}}^{\mathrm{inc}} \in [10^{-3}, 10^3]\,\mathrm{meV}$. Since the potential energy is a piecewise linear function it is possible to compute exact reference solutions as explained above. The relative errors in the ℓ^2-norm are depicted in the left column of Figure 4.2 for different numerical methods. As can be seen $\mathrm{DTBC}_{\mathrm{2nd}}$ and $\mathrm{PML}_{\mathrm{2nd}}$ yield similar results for medium to large energies. For very small energies $\mathrm{DTBC}_{\mathrm{2nd}}$ performs significantly better than $\mathrm{PML}_{\mathrm{2nd}}$. In addition, this experiment demonstrates the superiority of the higher-order methods $\mathrm{PML}_{\mathrm{4th}}$ and $\mathrm{PML}_{\mathrm{6th}}$ for energies $E_{\mathrm{kin}}^{\mathrm{inc}} \gtrsim 1\,\mathrm{meV}$. It should be noted that a smaller mesh size $\triangle x$ yields similar curves which are shifted downwards.

Now we compute scattering states for $E_{\mathrm{kin}}^{\mathrm{inc}} \in [24.9999, 25.0001]\,\mathrm{meV}$, i.e., for energies extremely near to the critical energy $E_{\mathrm{kin}}^{\mathrm{inc}} = 25\,\mathrm{meV}$ mentioned above. This time we use Dirichlet or Neumann BCs at the end points of the PML. Furthermore, we repeat the experiment with two different mesh sizes $\triangle x = 0.5\,\mathrm{nm}$ and $\triangle x =$

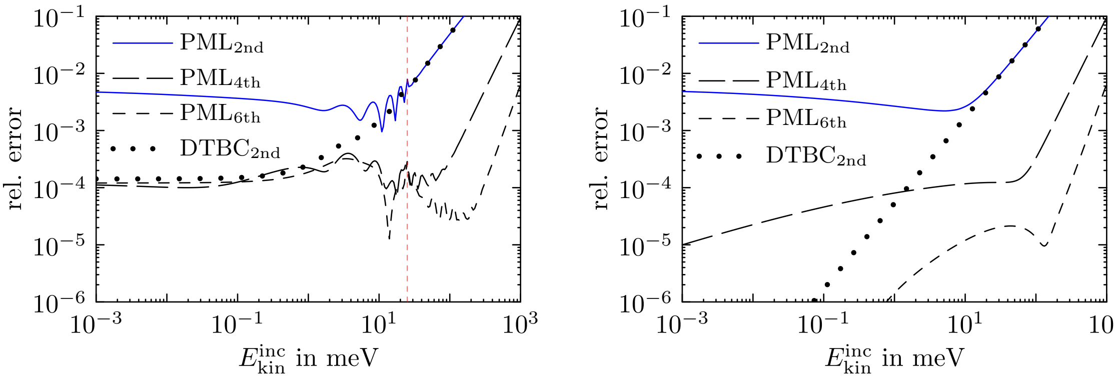

Figure 4.2: Left column: Relative errors of the computed scattering states as a function of the kinetic energy of the injected electrons at the left contact for an applied voltage of $U = -25\,\text{mV}$ corresponding to the simulation depicted in Figure 4.1. The critical energy $E_{\text{kin}}^{\text{inc}} = 25\,\text{meV}$ is marked by the dashed vertical line (see also Figure 4.3). Right column: The same situation as in the left column but for zero potential energy $V \equiv 0$.

0.1 nm. The numerical errors corresponding to Dirichlet BCs are depicted in the left column of Figure 4.3 and those corresponding to Neumann BCs are depicted in the right column. For $\triangle x = 0.5\,\text{nm}$ (top row) we observe a small perturbation of the numerical errors around the critical value. In case of PML_{2nd} the effect is obscured completely by the numerical error of the spatial discretization which is present even if transparent boundary condition are used (compare DTBC_{2nd}). For $\triangle x = 0.1\,\text{nm}$ (bottom row) the effect becomes more pronounced since the error of the spatial discretization is greatly reduced. However, the maximum error is effectively the same. This also holds true for smaller $\triangle x$ and finer sampling of $E_{\text{kin}}^{\text{inc}}$. For $E_{\text{kin}}^{\text{inc}} = 25\,\text{meV}$ the Neumann BC is exact and hence the numerical error is minimized. For that reason we prefer Neumann BCs at the end points of the computational domain in all subsequent simulations. Apart from this, both BCs provide essentially the same results. In summary, we found that the accuracy of the numerical methods using PML is reduced if the kinetic energy and thereby the wave number of an incoming wave approaches zero. However, in practice this effect is comparatively small and is very unlikely to happen.

For zero potential energy $V \equiv 0$ the scattering state solutions to the stationary Schrödinger equation are simple plane waves. The relative errors, to which we will return later, are shown in the right column of Figure 4.2.

In more realistic device simulation, e.g., Schrödinger-Poisson simulations [57], the kinetic energy of electrons injected from the contacts is bounded from above according to the injection profile determined by the Fermi-Dirac statistics. Therefore, typical values of $E_{\text{kin}}^{\text{inc}}$ are no larger than a few hundred meV in practical applications. At the same time the minimal value of $E_{\text{kin}}^{\text{inc}}$ used in quantum device simulations is

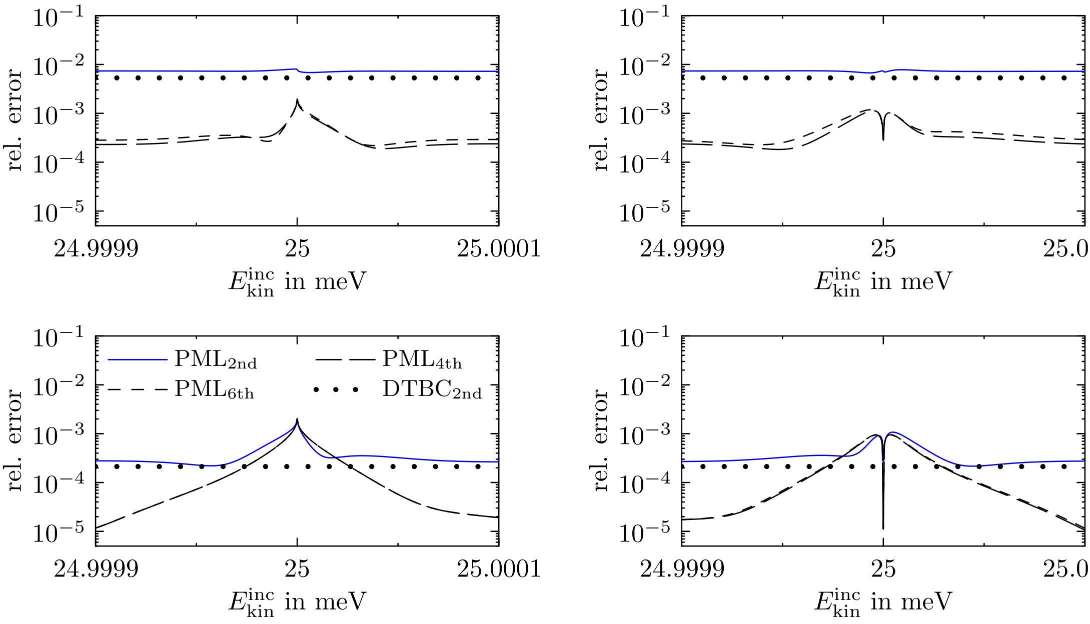

Figure 4.3: Close-up view of the relative errors shown in the left column of Figure 4.2 for $\triangle x = 0.5\,\mathrm{nm}$ and $\triangle x = 0.1\,\mathrm{nm}$ (1st, 2nd row) using Dirichlet (left column) or Neumann BCs (right column) at the end points of the PML.

typically not much smaller than 0.1 meV. In comparison, the simulations depicted in Figure 4.2 cover a much larger range of energies.

4.1.2 Wave packets

In this subsection, we consider the one-dimensional time-dependent Schrödinger equation

$$i\hbar\frac{\partial}{\partial t}\psi(x,t) = -\frac{\hbar^2}{2m^\star}\frac{\partial^2}{\partial x^2}\psi(x,t) + V(x,t)\psi, \quad \psi(\cdot,0)=\psi_0, \quad x\in\mathbb{R},\, t>0, \tag{4.23}$$

where the initial wave function is assumed to be compactly supported in $(0,L)$. We further assume that the the exterior potential is zero, i.e. $V(x,t)=0$ for $x\le 0$ and $x\ge L$, $t\ge 0$. Under these conditions, transparent boundary conditions are given in (3.16).

Discrete transparent boundary conditions. The 3-point finite difference discretization (4.15a) applied to the time-dependent Schrödinger equation yields the semi-discretized problem

$$\frac{d}{dt}\psi_j(t) = i\frac{\hbar}{2m^\star}D_x^{2,2\mathrm{nd}}\psi_j(t) - \frac{i}{\hbar}V(t)\psi_j(t) =: f(t,\psi_j(t)), \tag{4.24}$$

which is solved by the Crank-Nicolson (CN) time-integration method

$$\psi^{(n+1)} = \psi^{(n)} + \triangle t\, f\left((n+1/2)\triangle t, \psi^{(n+1/2)}\right). \tag{4.25}$$

Replacing $\psi_j^{(n+1/2)}$ by the average value $\big(\psi_j^{(n+1)} + \psi_j^{(n)}\big)\big/ 2$ yields the well-known Crank-Nicolson scheme

$$\begin{aligned}\left(I - \frac{i\hbar\triangle t}{4m^\star} D_x^2 + \frac{i\triangle t}{2\hbar} V_j^{(n+1/2)}\right) \psi_j^{(n+1)} \\ = \left(I + \frac{i\hbar\triangle t}{4m^\star} D_x^2 - \frac{i\triangle t}{2\hbar} V_j^{(n+1/2)}\right) \psi_j^{(n)}\end{aligned} \tag{4.26}$$

on the equidistant grid $x_j = j\triangle x$, $t_n = n\triangle t$ with $j \in \mathbb{Z}$ and $n \in \mathbb{N}_0$. DTBC for zero exterior potentials are given in (3.17). The combination of the Crank-Nicolson scheme with the DTBC in (3.17) represents an unconditionally stable discretization which is perfectly free of reflections [5, 6]. Please note that the corresponding solution coincides exactly with the solution of the discrete whole space problem (4.26) restricted to the grid X_{DTBC} defined in (4.4).

Perfectly Matched Layers. In the stationary scattering state calculations we employed PML which are able to absorb incoming waves of arbitrary low to very high energies simultaneously. Therefore we apply the same coordinate transformation (4.9) in the transient case which yields the time-dependent Schödinger-PML equation

$$i\hbar\frac{\partial}{\partial t}\psi(x,t) = -\frac{\hbar^2}{2m^\star} c(x)\frac{\partial}{\partial x}\left(c(x)\frac{\partial}{\partial x}\psi(x,t)\right) + V(x,t)\psi(x,t), \tag{4.27}$$

with the complex valued function c being defined in (4.10). Therefore, the semi-discretized problem is given by (4.24) wherein $D_x^{2,\mathrm{2nd}}$ is replaced with

$$\tilde{D}_x^2 \in \{\tilde{D}_x^{2,\mathrm{2nd}}, \tilde{D}_x^{2,\mathrm{4th}}, \tilde{D}_x^{2,\mathrm{6th}}\}$$

defined in (4.13):

$$\frac{d}{dt}\psi_j(t) = i\frac{\hbar}{2m^\star}\tilde{D}_x^2\psi_j(t) - \frac{i}{\hbar}V(t)\psi_j(t) =: \tilde{f}(t,\psi_j(t)). \tag{4.28}$$

The spatial grid X_{PML} is the same as in the stationary case defined in (4.16). Using the Crank-Nicolson time-integration method gives (4.26) but with the modified spatial differential operator $\tilde{D}_x^2$

$$\begin{aligned}\left(I - \frac{i\hbar\triangle t}{4m^\star} \tilde{D}_x^2 + \frac{i\triangle t}{2\hbar} V_j^{(n+1/2)}\right) \psi_j^{(n+1)} \\ = \left(I + \frac{i\hbar\triangle t}{4m^\star} \tilde{D}_x^2 - \frac{i\triangle t}{2\hbar} V_j^{(n+1/2)}\right) \psi_j^{(n)}.\end{aligned} \tag{4.29}$$

Alternatively, we solve (4.28) via the classical Runge Kutta method (RK4):

$$\begin{aligned}\psi^{(n+1)} &= \psi^{(n)} + \left(k_1 + 2k_2 + 2k_3 + k_4\right)/6,\\ k_1 &= \triangle t\,\tilde{f}(n\triangle t, \psi^{(n)}),\\ k_2 &= \triangle t\,\tilde{f}((n+1/2)\triangle t, \psi^{(n)} + k_1\triangle t/2),\\ k_3 &= \triangle t\,\tilde{f}((n+1/2)\triangle t, \psi^{(n)} + k_2\triangle t/2),\\ k_4 &= \triangle t\,\tilde{f}(n\triangle t, \psi^{(n)} + k_3\triangle t).\end{aligned} \tag{4.30}$$

In the context of quantum mechanics and especially in case of the Schrödinger equation RK4 is used very rarely. This is probably because the resulting spatio-temporal discretization is only conditionally stable. Moreover, the norm of the wave function is not a conserved quantity, i.e., in general $\|\psi^{(n+1)}\|_{\ell^2} = \|\psi^{(n)}\|_{\ell^2}$ does not hold exactly. We address these issues in a simple numerical experiment where we solve the ordinary time-dependent Schrödinger equation (without PML) for a harmonic oscillator potential $V(x) = m^\star\omega_* x^2/2$, $\omega_* = 0.25 \times 10^{14}\,\mathrm{s}^{-1}$. As a reference solution we consider a so called coherent state [36]

$$\psi(x,t) = \left(\frac{m^\star\omega_*}{\pi\hbar}\right)^{1/4} \exp\biggl(- \frac{m^\star\omega_*}{2\hbar}\Bigl(x^2 - 2xx_0e^{-i\omega_*t} + (x_0^2/2)e^{-2i\omega_*t} + x_0^2/2\Bigr) \\ - i\omega_*t/2\biggr)$$

wherein $x_0 = 10\,\mathrm{nm}$ denotes the expectation value of the particle at $t = 0$. The computational domain extends from $-50\,\mathrm{nm}$ to $50\,\mathrm{nm}$. Near the boundaries the wave function is zero (to numerical precision) and hence it is reasonable to employ homogeneous Dirichlet BCs. The initial state $\psi(x, t = 0)$ is propagated for 100 000 time steps using RK4. The spatial derivative is approximated via $D_x^{2,\mathrm{2nd}}$, $D_x^{2,\mathrm{4th}}$ or $D_x^{2,\mathrm{6th}}$ corresponding to 2nd-, 4th- and 6th-order spatial discretizations. Using $\triangle x = 0.5\,\mathrm{nm}$ and $\triangle t = 0.1\,\mathrm{fs}$ we obtain $\bigl|\|\psi^{(100\,000)}\|_{\ell^2}/\|\psi^{(0)}\|_{\ell^2} - 1\bigr| \lesssim 5.9 \times 10^{-11}$ independent from the spatial discretization. Moreover, the relative errors of the final wave functions are given by 2.19×10^{-1}, 6.56×10^{-4} and 6.42×10^{-6} corresponding to $D_x^{2,\mathrm{2nd}}$, $D_x^{2,\mathrm{4th}}$ and $D_x^{2,\mathrm{6th}}$, respectively. Stability bounds $\triangle t < \kappa(\triangle x)^2$ for the linear and nonlinear Schrödinger equation were derived in a recent paper [23] for 2nd- and 4th-order spatial discretizations. Remarkably, the constants κ stated in [23] agree with our experimental findings even if we solve the Schrödinger-PML equation. In case of the 6th-order spatial discretization our numerical experiments suggest that κ needs to be adopted slightly by a factor 3/4 compared to κ in the 4th-order discretization. In fact,

$$\kappa = 9m^\star/(8\sqrt{2}d\hbar) \tag{4.31}$$

gives almost sharp bounds for the simulations presented in this chapter. Here, d denotes the number of space dimensions.

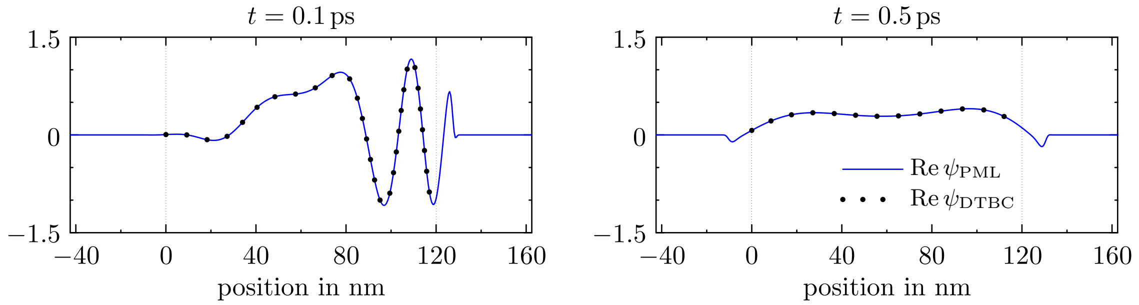

Figure 4.4: Real part of a wave packet corresponding to a superposition of three gaussians at $t = 0.1\,\mathrm{ps}$ and $t = 0.5\,\mathrm{ps}$ calculated using DTBC and PML.

Simulations. We solve the time-dependent Schrödinger equation (4.23) for zero potential energy. As a reference solution we choose a superposition of three gaussian wave packets

$$\xi(x,t) = \left(1 + i\frac{t}{\tau}\right)^{-1/2} \exp\left[\left(1 + i\frac{t}{\tau}\right)^{-1}\left(-\left(\frac{x - x_0}{2\sigma}\right)^2 + ik(x - x_0) - i\sigma^2 k^2 \frac{t}{\tau}\right)\right], \tag{4.32}$$

where $\tau = 2m^\star\sigma^2/\hbar$, $k = \sqrt{2m^\star E}/\hbar$. At $t = 0$ each gaussian is centered around $x_0 = L/2$. Using $\sigma = 7.5\,\mathrm{nm}$ the initial wave packet is practically zero outside the device domain $[0, L]$. The average energy of the first, second and third gaussian is $E = 0\,\mathrm{meV}$, $E = 25\,\mathrm{meV}$ and $E = 75\,\mathrm{meV}$. Therefore the reference solution is a superposition of propagating plane waves $\exp(ik_p x - i\omega_p t)$ of very low to high energies $E_p = (\hbar k_p)^2/2m^\star$ wherein the wave frequency is given by $\omega_p = E_p/\hbar$. We use the same spatial mesh size $\triangle x = 0.5\,\mathrm{nm}$ as for the scattering state simulations. The time step size is given by $0.1\,\mathrm{fs}$. The real part of the numerical solution at $t = 0.1\,\mathrm{ps}$ and $t = 0.5\,\mathrm{ps}$ using DTBC and PML is shown in Figure 4.4. Both solutions were obtained using 2nd-order spatial discretizations in combination with the Crank-Nicolson time-integration method. The corresponding numerical errors as a function of time are depicted in Figure 4.5. At the beginning of the simulation both methods yield similar results. During this phase the numerical error is dominated by the fast traveling parts of the wave packet since their oscillations in space and time are difficult to handle by low order methods. Shortly afterwards, the relative error of the solution corresponding to PML is stabilizing at a value of approximately 3×10^{-3}. This agrees with the numerical errors shown in the right column of Figure 4.2 since at later times the wave packet can be thought of as a superposition of primarily low energy plane wave scattering states. In contrast, the numerical error of the solution computed using DTBC decreases continuously. Moreover, Figure 4.5 shows the numerical errors according to higher order methods. For example, a sixth

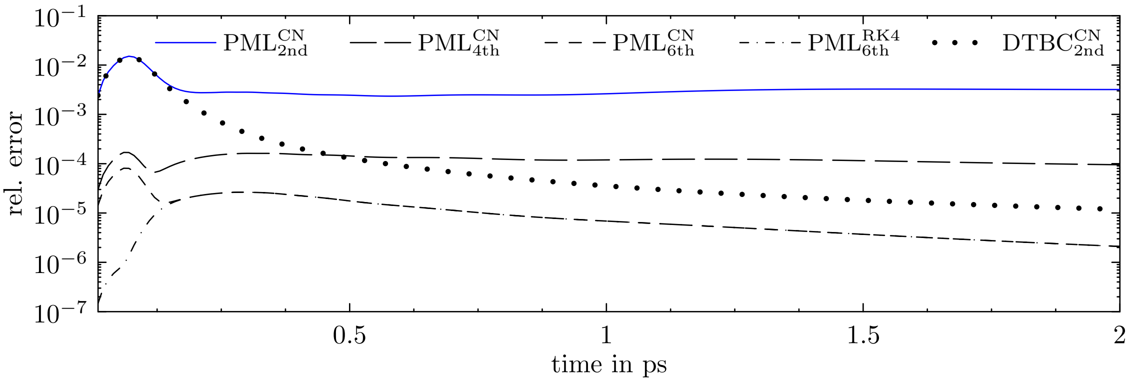

Figure 4.5: Relative errors as a function of time for different numerical methods corresponding to the simulation depicted in Figure 4.4.

order spatial discretization in combination with PML reduces the maximum relative error by more than two orders of magnitude. The maximum error can be reduced further by replacing the 2nd-order Crank-Nicolson time-integration method with the fourth-order Runge-Kutta method. In this case, even the fast temporal oscillations in the beginning of the simulation are resolved with high accuracy.

4.1.3 Time-dependent incoming waves

Before turning to transient scattering state simulations, it is useful to explain first how to realize an incoming wave at a boundary of the device domain. As an example we consider the free time-dependent Schrödinger equation where an incident plane wave

$$\psi^{\mathrm{inc}}(x,t) = \exp(ikx - i\omega t), \quad x \le 0, \quad \omega = \hbar k^2/(2m^\star),$$

is prescribed at $x = 0$. To avoid a discontinuity at $(x,t) = (0,0)$ we assume that the initial wave function is such as the one shown in the left column of Figure 4.6 (for the details see [6]). The transparent boundary condition at $x = L$ in (3.16b) remains the same. However, at $x = 0$ we need to prescribe an inhomogenous transparent boundary condition which follows if we apply (3.16a) to the wave $\psi - \psi^{\mathrm{inc}}$ [6, 3]:

$$\frac{\partial}{\partial x}\left(\psi(x,t) - \psi^{\mathrm{inc}}(x,t)\right)\Big|_{x=0} = \sqrt{\frac{2m^\star}{\pi\hbar}}\, e^{-i\pi/4}\frac{d}{dt}\int_0^t \frac{\psi(0,\tau) - \psi^{\mathrm{inc}}(0,\tau)}{\sqrt{t-\tau}}\, d\tau. \quad (4.33)$$

Discrete transparent boundary conditions. The discrete analogue of (4.33) for the Crank-Nicolson scheme (4.26) follows by replacing $\psi_j^{(n)}$ with $\psi_j^{(n)} - \phi_j^{(n)}$ in (3.17a)

$$\psi_1^{(n+1)} - s^{(0)}\psi_0^{(n+1)} = \sum_{\ell=1}^{n} s^{(n+1-\ell)}\left(\psi_0^{(\ell)} - \phi_0^{(\ell)}\right) - \left(\psi_1^{(n)} - \phi_1^{(n)}\right) + \phi_1^{(n+1)} - s^{(0)}\phi_0^{(n+1)}.$$

Here

$$\phi_j^{(n)} = \exp(ikx_j - i\omega n\triangle t) \tag{4.34}$$

represents an incoming discrete plane wave, i.e., k is related to $E = E_{\mathrm{kin}}^{\mathrm{inc}}$ according to the discrete E–k–relation (4.8) and the wave frequency is given by the discrete E–ω–relation

$$\omega = 2\arctan\left(E\triangle t/(2\hbar)\right)/\triangle t \tag{4.35}$$

which is the discrete analogue of $\omega = E/\hbar$ (see [6]).

Perfectly Matched Layers. We solve the transient Schrödinger-PML equation (4.27) where an incoming time-dependent plane wave is prescribed at one of the device boundaries. The incoming wave is realized analogously to the case of the stationary scattering state simulations. As an example we consider the Crank-Nicolson scheme (4.29) for $\tilde{D}_x^2 = \tilde{D}_x^{2,\mathrm{2nd}}$. In the vicinity of the device boundary $x_{j_0} = 0$ the potential energy is zero, but more importantly, the PML is inactive. The wave function in the left contact is a superposition of an incoming and a reflected wave. However, the incoming wave (4.34) is eliminated in the left lead and hence $\psi_j^{(n)}$ represents the reflected wave for $j < j_0$. Accordingly, the finite difference equations for $j_0 - 1$ and j_0 need to be modified as follows:

$$\begin{aligned}
&\psi_{j_0-1}^{(n+1)} - (i\hbar\triangle t)/(4m^\star(\triangle x)^2)\Big[\psi_{j_0-2}^{(n+1)} - 2\psi_{j_0-1}^{(n+1)} + \big(\psi_{j_0}^{(n+1)} - \phi_{j_0}^{(n+1)}\big)\Big] \\
&\qquad = \psi_{j_0-1}^{(n)} + (i\hbar\triangle t)/(4m^\star(\triangle x)^2)\Big[\psi_{j_0-2}^{(n)} - 2\psi_{j_0-1}^{(n)} + \big(\psi_{j_0}^{(n)} - \phi_{j_0}^{(n)}\big)\Big], \\
&\psi_{j_0}^{(n+1)} - (i\hbar\triangle t)/(4m^\star(\triangle x)^2)\Big[\big(\psi_{j_0-1}^{(n+1)} + \phi_{j_0-1}^{(n+1)}\big) - 2\psi_{j_0}^{(n+1)} + \psi_{j_0+1}^{(n+1)}\Big] \\
&\qquad = \psi_{j_0}^{(n)} + (i\hbar\triangle t)/(4m^\star(\triangle x)^2)\Big[\big(\psi_{j_0-1}^{(n)} + \phi_{j_0-1}^{(n)}\big) - 2\psi_{j_0}^{(n)} + \psi_{j_0+1}^{(n)}\Big].
\end{aligned} \tag{4.36}$$

Since $\phi_{j_0}^{(n)}$ and $\phi_{j_0-1}^{(n)}$ are known for all $n \in \mathbb{N}_0$ we collect these values

$$b_j^{(n)} = \begin{cases} -\big(i\hbar\triangle t/(4m^\star(\triangle x)^2)\big)\big(\phi_{j_0}^{(n+1)} + \phi_{j_0}^{(n)}\big) & \text{for } j = j_0 - 1, \\ +\big(i\hbar\triangle t/(4m^\star(\triangle x)^2)\big)\big(\phi_{j_0-1}^{(n+1)} + \phi_{j_0-1}^{(n)}\big) & \text{for } j = j_0, \\ 0 & \text{else,} \end{cases}$$

on the right-hand side of (4.29). In case $\tilde{D}_x^2 = \tilde{D}_x^{2,\mathrm{4th}}$ and $\tilde{D}_x^2 = \tilde{D}_x^{2,\mathrm{6th}}$ we proceed in a similar way. However, due to the extended finite difference stencils, four or six finite difference equations need to be modified accordingly. If the semi-discretized problem is solved via the Runge-Kutta method (4.30) the incoming wave needs to be taken into account at each intermediate step $k_1, .., k_4$.

Simulations. An incoming plane wave is depicted in Figure 4.6 at $t = 0\,\mathrm{ps}$ and $t = 0.1\,\mathrm{ps}$. The potential energy is zero everywhere and the kinetic energy of the incoming electrons amounts to $E_{\mathrm{kin}}^{\mathrm{inc}} = 25\,\mathrm{meV}$. Please note, that it would take quite a long time (compared to the underlying timescale) before the wave function becomes approximately stationary.

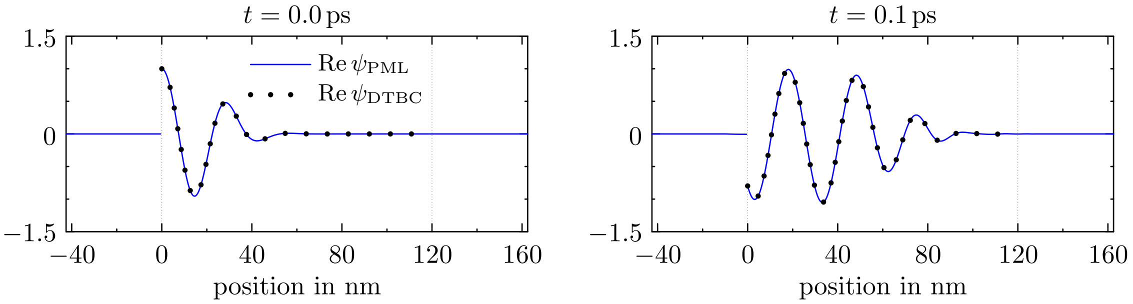

Figure 4.6: An incoming plane wave at the left contact. Solid line: DTBC. Dashed line: PML. The kinetic energy of the incoming plane wave is $E_{\mathrm{kin}}^{\mathrm{inc}} = 25\,\mathrm{meV}$.

4.1.4 Transient scattering states

A transient scattering state simulation describes a quantum device where a continuously incoming plane wave is prescribed at one of the device contacts. At the same time, the potential energy is allowed to change with time. The lead potentials need to be spatially constant but may depend on time too. In contrast to the simulation depicted in Figure 4.6 one is typically not interested in the initial transient phase. Instead of waiting for the wave function to become stationary for the first time, one would like to initialize the simulation with a scattering state. This situation is considered in [6] where the potential energy is switched instantaneously. An extension to continuously time-variable potentials is presented in Chapter 3. As an example we consider the time-dependent Schödinger equation with the ramp-like potential (4.22), where the applied voltage U is assumed to be time-dependent with $U(t \leq 0) = U_0$. The initial wave function is given by the scattering state solution ϕ of the stationary Schrödinger equation for the potential energy according to U_0. As before, we consider electrons injected at the left contact with energy $E = E_{\mathrm{kin}}^{\mathrm{inc}}$. Inhomogeneous transparent boundary conditions are given in (3.19) and (3.21). For further details we refer to Section 3.2.1.

Discrete transparent boundary conditions. The discrete analogue of (3.19) follows by replacing $\psi_j^{(n)}$ with $\psi_j^{(n)} - \beta^{(n)}\phi_j$ in (3.17a)

$$\begin{aligned}(\psi_1^{(n+1)} - \beta^{(n+1)}\phi_1) - s^{(0)}(\psi_0^{(n+1)} - \beta^{(n+1)}\phi_0)& \\ = \sum_{\ell=1}^{n} s^{(n+1-\ell)}(\psi_0^{(\ell)} - \beta^{(\ell)}\phi_0) - (\psi_1^{(n)} - \beta^{(n)}\phi_1)&,\end{aligned} \tag{4.37}$$

where ϕ_j is a solution of the discrete scattering state problem outlined above. The discretization of the gauge-change term

$$\beta^{(n)} = \exp\left(-2in \arctan\left(\triangle t E/(2\hbar)\right)\right) \approx \exp(-iEt/\hbar)$$

is consistent with the underlying Crank-Nicolson time-integration method (compare Section 3.2.1). Similarly, the discrete analogue of (3.21) follows by replacing $\psi_j^{(n)}$

with $\epsilon^{(n)}\psi_j^{(n)} - \gamma^{(n)}\phi_j$ in (3.17b):

$$\begin{aligned}(\epsilon^{(n+1)}\psi_{J-1}^{(n+1)} - \gamma^{(n+1)}\phi_{J-1}) - s^{(0)}(\epsilon^{(n+1)}\psi_J^{(n+1)} - \gamma^{(n+1)}\phi_J)&\\ = \sum_{\ell=1}^{n} s^{(n+1-\ell)}(\epsilon^{(\ell)}\psi_J^{(\ell)} - \gamma^{(\ell)}\phi_J) - (\epsilon^{(n)}\psi_{J-1}^{(n)} - \gamma^{(n)}\phi_{J-1}).&\end{aligned} \tag{4.38}$$

The gauge-change terms are approximated via

$$\begin{aligned}\gamma^{(n)} &= \exp\left[2in\left(\arctan(\triangle t V_r^{(0)}/(2\hbar)) - \arctan(\triangle t E/(2\hbar))\right)\right]\\ &\approx \exp(iV_r(0)t/\hbar)\exp(-iEt/\hbar),\\ \epsilon^{(n)} &= \exp\left(2i\sum_{\ell=0}^{n-1}\arctan(\triangle t V_r^{(\ell+1/2)}/(2\hbar))\right) \approx \exp\left(i\int_0^t V_r(s)\,ds/\hbar\right),\end{aligned} \tag{4.39}$$

which is also compatible with the underlying Crank-Nicolson method. For more information we refer to Section 3.2.1.

We note that the Crank-Nicolson scheme (4.26) along with the inhomogeneous DTBC (4.37) and (4.38) is still perfectly free of spurious reflections. In fact, (4.37) and (4.38) yield an exact truncation of the discrete whole space problem.

Perfectly Matched Layers. No further steps are necessary to realize a transient scattering state simulation using PML. Given the potential energy at $t = 0$ and the kinetic energy $E_{\text{kin}}^{\text{inc}}$ of the electrons injected at the device contact we compute a scattering state solution of the discrete stationary Schödinger-PML equation. This scattering state serves as the initial state of the transient problem where a time-dependent incoming plane wave (4.34) is prescribed at the device contact.

Simulations. We consider the numerical experiment depicted in Figure 4.7 showing the time evolution of a transient scattering state at selected times. The incoming plane wave at the left contact represents electrons with a kinetic energy of $E_{\text{kin}}^{\text{inc}} = 25\,\text{meV}$ traveling to the right. The applied voltage as a function of time is given in the left column of the first row in Figure 4.8. Accordingly, we initialize the simulation with the scattering state corresponding to an applied voltage of $U_0 = -100\,\text{mV}$. Until $t = 0.5\,\text{ps}$ we keep the applied voltage constant and hence the numerical solution remains the same. More precisely, $|\psi|^2$ remains the same while $\operatorname{Re}\psi$ oscillates with time. From $t = 0.5\,\text{ps}$ up to $t = 12.5\,\text{ps}$ the applied voltage is varied corresponding to a medium oscillation with a large amplitude and a fast oscillation with a smaller amplitude. As a result the wave function shows a wild behavior as indicated in the 2nd, 3rd and 4th row of Figure 4.7. From $t = 12.5\,\text{ps}$ until the end of the simulation the applied voltage is kept constant at $U = 0\,\text{mV}$. As can be seen from the last row of Figure 4.7 even at $t = 20\,\text{ps}$ the wave function has not become perfectly stationary again.

The simulation described above was carried out using two numerical methods. In both cases the time-dependent Schrödinger equation is discretized via the Crank-Nicolson scheme using 2nd-order approximations of the spatial derivatives. The first

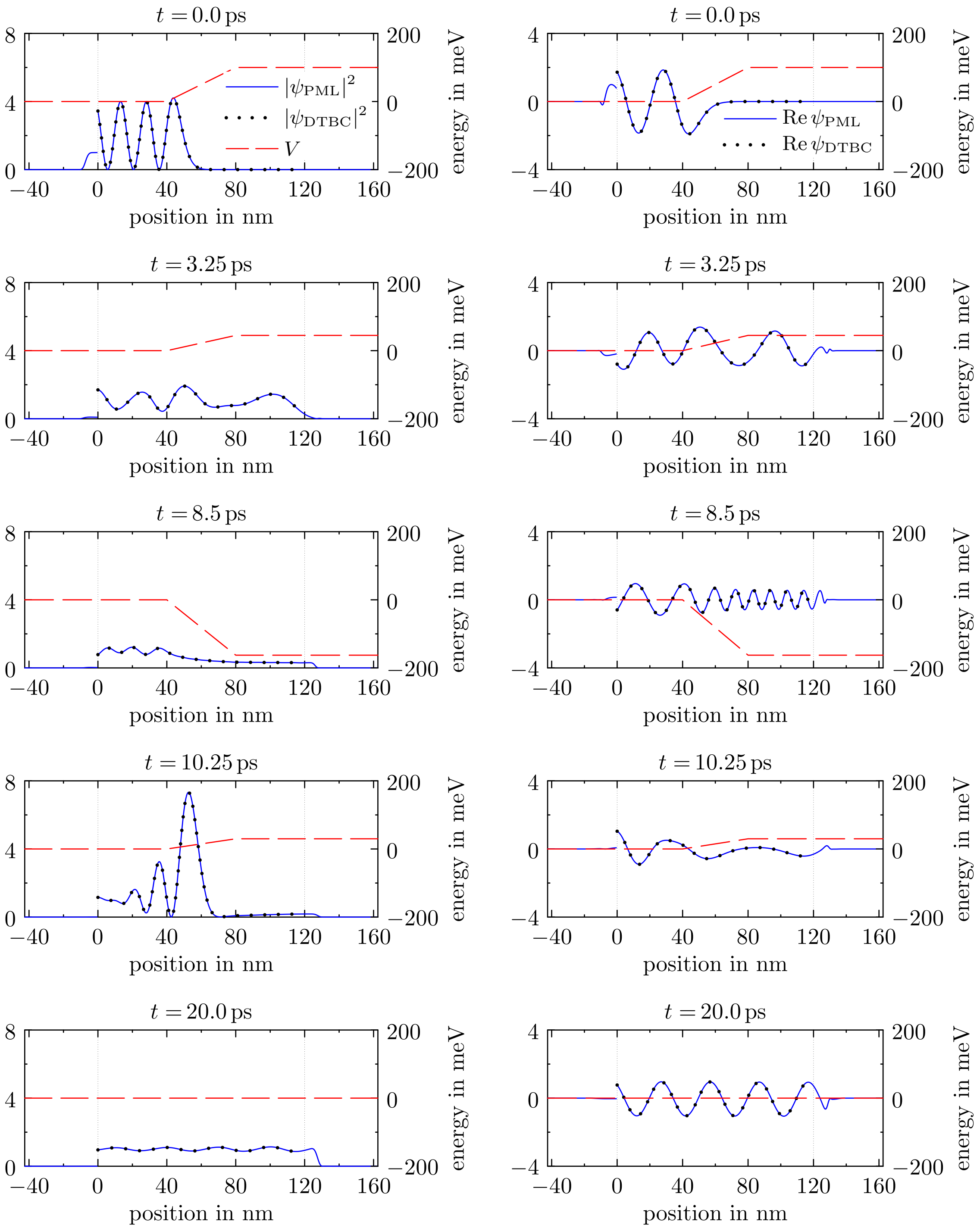

Figure 4.7: Transient scattering state experiment at selected times for a continuously incoming plane wave prescribed at the left contact. The incoming plane wave corresponds to electrons with a kinetic energy of $E_{\mathrm{kin}}^{\mathrm{inc}} = 25\,\mathrm{meV}$ traveling to the right.

method uses DTBC whereas the second method employs PML. Inside the device-domain both discretizations coincide exactly. Since DTBC represent an exact truncation of the discrete whole space problem the relative difference of both methods results from the PML employed by the second method. For a spatial mesh size of $\triangle x = 0.5\,\mathrm{nm}$ and a time step size of $\triangle t = 0.1\,\mathrm{fs}$ the relative difference as a function of time is depicted in left column (2nd row) of Figure 4.8. The same part of the figure shows the relative differences when the experiment is repeated using different values for the kinetic energy of the incoming electrons $E_{\mathrm{kin}}^{\mathrm{inc}} \in [0.25, 2.5, 25, 250]\,\mathrm{meV}$. Even though $E_{\mathrm{kin}}^{\mathrm{inc}}$ varies from extremely low energies to extremely large energies the relative difference is always localized around a value of 3×10^{-3}.

We repeat the experiment for the same values of $E_{\mathrm{kin}}^{\mathrm{inc}}$, but this time the applied voltage oscillates slowly around the critical values $U \in [-0.25, -2.5, -25, -250]\,\mathrm{mV}$ as shown in right column (1st row) of Figure 4.8. In this way we trigger waves of arbitrary low energy in the right lead. The corresponding relative differences as a function of time are depicted in the 2nd row (right column). As can be seen PML can handle even this extreme case.

The DTBC (4.37) and (4.38) are tailored specifically to the 2nd-order Crank-Nicolson scheme (4.26). For that reason we can not easily make a statement on the accuracy of the methods which use PML in combination with higher-order finite difference operators. However, the stationary and transient simulations considered before show that the numerical errors of the higher-order methods are strongly reduced. Here we imitate this effect by repeating the simulations described above with a reduced spatial mesh size of $\triangle x = 0.1\,\mathrm{nm}$. The time steps size $\triangle t$ remains unchanged. As can be seen from the last row in Figure 4.8 the relative differences decrease by more than one order of magnitude.

It is noteworthy that the time step size in case of the larger mesh size $\triangle x = 0.5\,\mathrm{nm}$ could be increased ($\triangle t \approx 0.25\,\mathrm{fs}$) withouth effecting the results significantly. However, in case of $\triangle x = 0.1\,\mathrm{nm}$ a small time step size ($\triangle t \lesssim 0.1\,\mathrm{fs}$) is needed in order to obtain the level of accuracy shown in the last row of Figure 4.8.

4.2 Quantum waveguide device simulations

4.2.1 Scattering states in quantum waveguides

We consider the stationary Schrödinger equation

$$\hat{H}\phi = E\phi, \quad \hat{H} = -\hbar^2/2m^\star\Delta + V \tag{4.40}$$

on the infinite stripe $\Omega = \mathbb{R} \times (0, L_2)$ wherein the Hamiltonian $\hat{H}$ is introduced for later reference. Furthermore, we prescribe homogeneous Dirichlet BCs at $x_2 = 0$ and $x_2 = L_2$. In particular we are interested in quantum waveguide device simulations. For this reason, we assume that the potential energy in the exterior domain depends

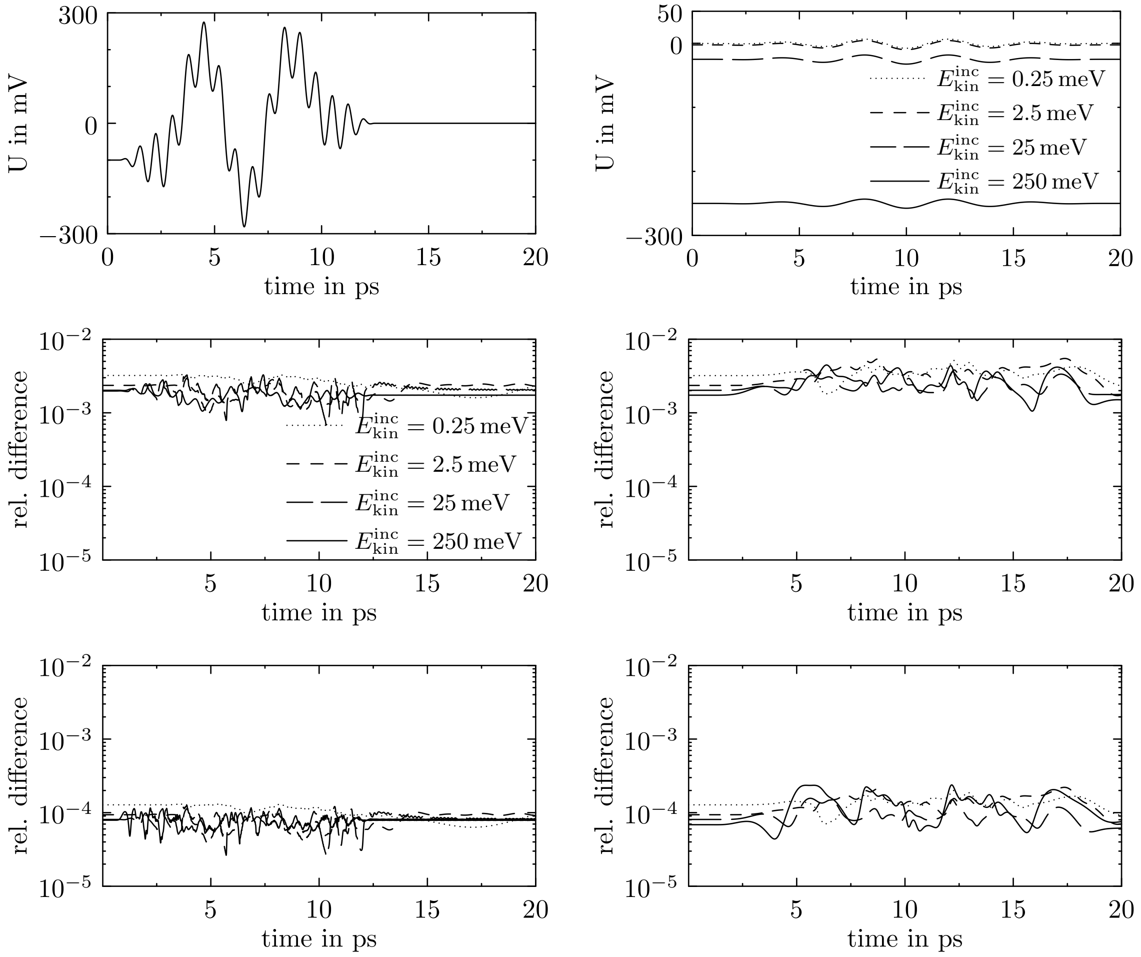

Figure 4.8: Top left: Applied voltage U as function of time corresponding to the simulation depicted in Figure 4.7. Center left: Relative differences between the solutions computed using DTBC and PML for $\triangle x = 0.5\,\text{nm}$ and $\triangle t = 0.1\,\text{fs}$. The experiment is carried out four times corresponding to different values of the kinetic energy $E_{\text{kin}}^{\text{inc}} = 0.25\,\text{meV}$, $2.5\,\text{meV}$, $25\,\text{meV}$ and $250\,\text{meV}$. Bottom left: The same experiments as above but with decreased spatial mesh size $\triangle x = 0.1\,\text{nm}$. Right column: Similar experiments as shown in the left column. The applied voltage oscillates slowly around the critical values $U = -0.25\,\text{mV}$, $-2.5\,\text{mV}$, $-25\,\text{mV}$ and $-250\,\text{mV}$.

on the transversal coordinate only:

$$V(x_1,x_2) = \begin{cases} V_\ell(x_2) & \text{for } x_1 \le 0, \\ V_r(x_2) & \text{for } x_1 \ge L_1. \end{cases}$$

In general V_ℓ and V_r may be different, but to simplify the notation we assume $V_\ell(x_2) = V_r(x_2)$, $x_2 \in [0, L_2]$. As an example, we refer to the ring-shaped device described by the potential energy shown in Figure 4.9. We further assume that the wave function in the leads

$$\phi(x_1,x_2) = \sum_{m=0}^{\infty} c^{(m)}(x_1)\,\chi^{(m)}(x_2), \quad x_1 \le 0, \quad x_1 \ge L_1 \tag{4.41}$$

can be decomposed into transversal waveguide eigenstates

$$-\frac{\hbar^2}{2m^\star}\frac{\partial^2}{\partial x_2^2}\chi^{(m)}(x_2) + V(x_2)\chi^{(m)}(x_2) = E^{(m)}\chi^{(m)}(x_2),\ \chi^{(m)}(0) = 0,\ \chi^{(m)}(L_2) = 0,$$
$$\langle \chi^{(m)}, \chi^{(n)} \rangle = \int_0^{L_2} \chi^{(m)}(x_2)\,\overline{\chi^{(n)}(x_2)}\,dx_2 = \delta_{m,n} \tag{4.42}$$

where

$$c^{(m)}(x_1) = \langle \phi, \chi^{(m)} \rangle = \int_0^{L_2} \phi(x_1,x_2)\,\overline{\chi^{(m)}(x_2)}\,dx_2. \tag{4.43}$$

Inserting (4.41) into the two-dimensional stationary Schrödinger equation (4.40) reveals that each mode coefficient satisfies a one-dimensional stationary Schrödinger equation

$$-\frac{\hbar^2}{2m^\star}\frac{\partial^2}{\partial x_1^2}c^{(m)}(x_1) + E^{(m)}c^{(m)}(x_1) = Ec^{(m)}(x_1), \quad m \in \mathbb{N}_0. \tag{4.44}$$

In the following discussion we consider electrons injected at the left terminal traveling to the right. Let their wave vector be given by $(k,0,0)^\top$ with $k > 0$. At the time of the injection the electrons are assumed to be in the ground state with respect to the cross section of the waveguide potential in the left lead. Hence, the incoming electrons are represented by

$$\phi^{\text{inc}}(x_1,x_2) := \exp(ikx_1)\chi^{(0)}(x_2) \tag{4.45}$$

and their total energy amounts to $E = E_{\text{kin}}^{\text{inc}} + E^{(0)}$ where $E_{\text{kin}}^{\text{inc}} = \hbar^2k^2/(2m^\star)$.

The problem in the leads is effectively one-dimensional. For that reason transparent boundary conditions at $x_1 = 0$ and $x_1 = L_1$ could be derived using the results from Section 4.1. However, they need to be prescribed for each coefficient $c^{(m)}$ with $m \in \mathbb{N}_0$. In particular, we refer to the transparent boundary conditions (4.2).

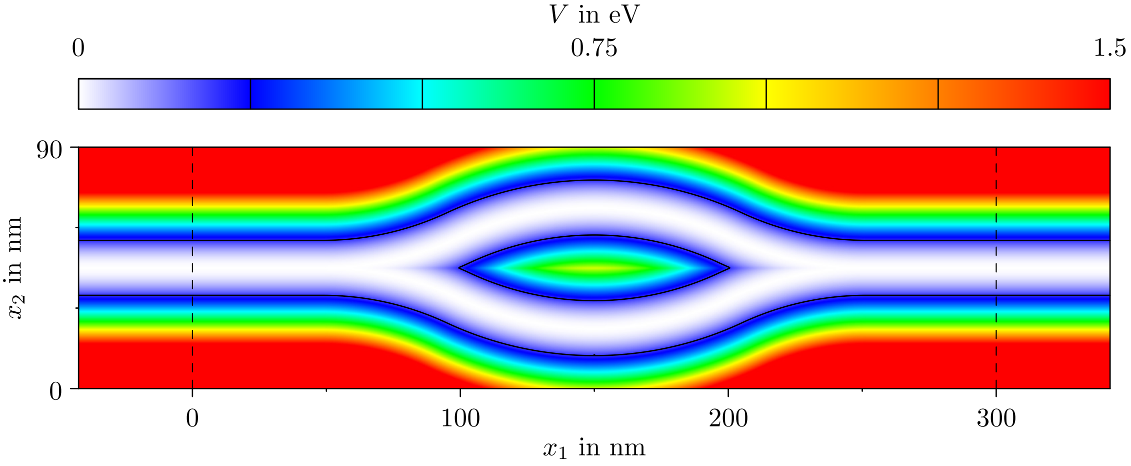

Figure 4.9: Potential energy of a ring shaped quantum waveguide device. The device domain extends from $x_1 = 0\,\text{nm}$ to $x_1 = 300\,\text{nm}$ and from $x_2 = 0\,\text{nm}$ to $x_2 = 90\,\text{nm}$. The black solid line correponds to the isovalue 200 meV.

Discrete transparent boundary conditions. Using symmetric second-order finite difference approximations of the spatial derivatives in (4.40) yields

$$-\frac{\hbar^2}{2m^\star}\left(\frac{\phi_{j_1-1,j_2} - 2\phi_{j_1,j_2} + \phi_{j_1+1,j_2}}{(\triangle x)^2} + \frac{\phi_{j_1,j_2-1} - 2\phi_{j_1,j_2} + \phi_{j_1,j_2+1}}{(\triangle x)^2}\right) + V_{j_1,j_2}\phi_{j_1,j_2} = E\phi_{j_1,j_2} \tag{4.46}$$

on the semi-infinite grid

$$\Omega_{\triangle x} := \{(j_1\triangle x, j_2\triangle x) : j_1 \in \mathbb{Z},\ j_2 = 0, ..., J_2,\ J_1\triangle x = L_1,\ J_2\triangle x = L_2\},$$

where $\phi_{j_1,0} = \phi_{j_1,J_2} = 0$ for all $j_1 \in \mathbb{Z}$.

In particular we seek for a solution of (4.46) restricted to the grid points of the device domain

$$\Omega_{\text{DTBC}} := \{(j_1\triangle x, j_2\triangle x) : j_1 = 0, ..., J_1,\ j_2 = 0, ..., J_2\},$$

where an incoming plane wave is prescribed at the left boundary. Disregarding open boundary conditions and the incoming plane wave we can state the problem in the following form:

$$S\phi = 0, \quad \phi_j = \phi_{j_1,j_2}, \quad j = j_1 J_2 + j_2, \quad j_1 = 0, ..., J_1, \quad j_2 = 0, ..., J_2. \tag{4.47}$$

Here S, denotes a sparse matrix $S := -\hbar^2/(2m^\star)\Delta^{\text{2nd}}_{x_1,x_2} + \text{diag}(d)$ with

$$\Delta^{\text{2nd}}_{x_1,x_2} := \left(D^{2,\text{2nd}}_{x_1} \otimes I_{J_2} + I_{J_1} \otimes D^{2,\text{2nd}}_{x_2}\right).$$

The vector d is given by $d_j = V_j - E,\ j = 0, ..., (J_1+1)(J_2+1) - 1$. Furthermore I_{J_1}, I_{J_2} are unit matrices of dimension J_1 and J_2, respectively. Finally, $D^{2,\text{2nd}}_{x_1}$ and

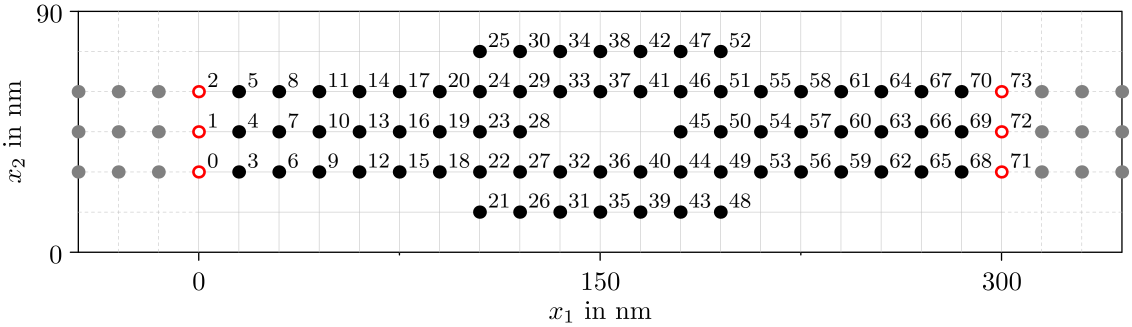

Figure 4.10: Reduced mesh of the ring shaped quantum device shown in Figure 4.9. For visualization purposes $\triangle x$ is chosen extremely large. Grid points where the wave function is practically zero have been eliminated. The computational domain is truncated using either DTBC or PML. In case of DTBC the reduced mesh is given by the grid points between $x_1 = 0\,\text{nm}$ and $x_1 = 300\,\text{nm}$. In case of PML the reduced mesh contains also the grey points. In both cases we prescribe an incoming plane wave at $x_1 = 0\,\text{nm}$.

$D^{2,2\text{nd}}_{x_2}$ are finite difference matrices defined according to (4.15a) with respect to the two spatial directions x_1 and x_2. The Kronecker product operation on matrices is denoted by $\otimes$.

In order to realize discrete open boundary conditions at the device terminals we need to replace the finite difference equations in (4.47) which correspond to grid points at the left and right boundary of Ω_{DTBC}. On the other hand, some of the finite difference equations in (4.47) need to be eliminated because ϕ_j is zero due to the homogeneous Dirichlet BCs imposed at the top and the bottom boundary of Ω_{DTBC}. In fact, we eliminate even more equations. In this regard it is noted that the wave function decreases exponentially within areas where the potential energy is greater than the total energy of the electron. Thus, at some distance from the center of the waveguide profile ϕ_j is zero (to numerical precision) and hence the corresponding finite difference equation may be eliminated. In the particular case of the ring-shaped quantum device depicted in Figure 4.9 we eliminate all rows $S[j,:]$ and colums $S[:,j]$ of S with $j \in \{j : V_j > 750\,\text{meV}\}$. Let $N \times N$ denote the new size of S. Through this elimination process we implicitly obtain a reduced mesh and a new numbering of the remaining free indices. An illustration is given in Figure 4.10.

We still need to replace the remaining rows of S corresponding to grid points at the device contacts (Figure 4.10, open red points). Let us consider the left terminal first. Since the potential energy in the exterior domain depends solely on the transversal coordinate, we temporarily define $V_{j_2} := V_{j_1,j_2}$ for $j_1 \leq 0$ and $j_2 = 0, ..., J_2$. Analogously to the continuous case the wave function in the lead can

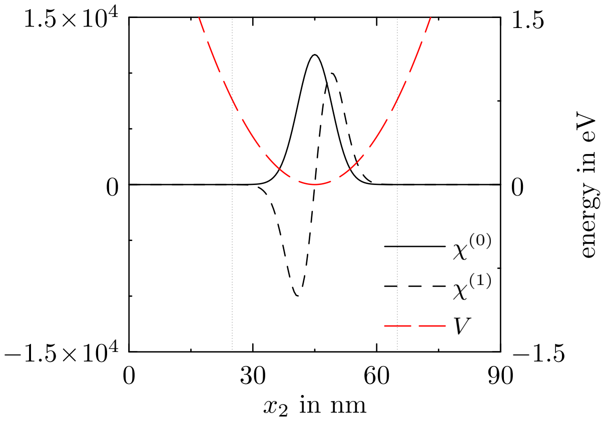

Figure 4.11: Ground state and first excited eigenstate corresponding to the cross-sectional potential energy in the left lead of the quantum waveguide depicted in Figure 4.9. The vertical dotted lines indicate the boundaries of the reduced mesh.

be decomposed into transversal waveguide eigenstates:

$$\phi_{j_1,j_2} = \sum_{m=0}^{M-1} c_{j_1}^{(m)} \chi_{j_2}^{(m)}, \quad j_1 \leq 0, \quad j_2 = j_{21}, ..., j_{22}.$$

The indices j_{21} and j_{22} depend on the elimination process described above. In the example of Figure 4.10 we have $j_{21} = 2$ and $j_{22} = 4$. Hence, the number of free indices along the x_2-direction in the left lead is given by $M = j_{22} - j_{21} + 1$. Further, $\chi^{(m)}$ denotes the m-th eigenstate of the discrete eigenvalue problem

$$-\frac{\hbar^2}{2m^\star} \frac{\chi_{j_2-1}^{(m)} - 2\chi_{j_2}^{(m)} + \chi_{j_2+1}^{(m)}}{(\triangle x)^2} + V_{j_2}\chi_{j_2}^{(m)} = E^{(m)}\chi_{j_2}^{(m)},\ j_2 = j_{21}, ..., j_{22},\ m = 0, ..., M-1,$$

where we impose homogeneous Dirichlet BCs at $x_2 = (j_{21} - 1)\triangle x$ and $x_2 = (j_{22} + 1)\triangle x$. We further ensure that all eigenstates are orthonormal with respect to the scalar product

$$\langle \chi^{(m)}, \chi^{(n)} \rangle = \triangle x \sum_{j_2=j_{21}}^{j_{22}} \chi_{j_2}^{(m)} \overline{\chi_{j_2}^{(n)}}. \tag{4.48}$$

The ground state ($m = 0$) and the first excited state ($m = 1$) are shown in Figure 4.11.

In the continuous case the coefficients $c^{(m)}$ solve (4.44) for all $m \in \mathbb{N}_0$. The discrete analogue of (4.44) reads

$$-\frac{\hbar^2}{2m^\star} \frac{c_{j_1-1}^{(m)} - 2c_{j_1}^{(m)} + c_{j_1+1}^{(m)}}{(\triangle x)^2} + E^{(m)} c_{j_1}^{(m)} = E c_{j_1}^{(m)}, \quad m = 0, ..., M-1, \tag{4.49}$$

which can be identified with the one-dimensional discrete stationary Schrödinger equation (4.3) if the potential energy is substituted by $E^{(m)}$. Thus, (4.49) admits two solutions of the form

$$c_{j_1}^{(m)} = \big(\alpha^{(m)}\big)^{j_1}, \quad \alpha^{(m)} = 1 - \frac{m^\star(E-E^{(m)})(\triangle x)^2}{\hbar^2} \\ \pm i\sqrt{\frac{2m^\star(E-E^{(m)})(\triangle x)^2}{\hbar^2} - \frac{(m^\star)^2(E-E^{(m)})^2(\triangle x)^4}{\hbar^4}},$$

where m denotes the mode index and $m^\star$ is the effective mass of the electron. Recall that we consider electrons which are injected at the left terminal travelling to the right. At the time of the injection the electrons are assumed to be in the ground state with respect to the waveguide profile. Thus, we have

$$c_{j_1}^{(0)} = A\big(\alpha^{(0)}\big)^{j_1} + B\big(\alpha^{(0)}\big)^{-j_1},$$

where A and B are the amplitudes of the incoming and the reflected wave projected to the ground state $\chi^{(0)}$. Writing the above equation for $j_1 = 0, 1$ and eliminating B yields

$$c_0^{(0)} - \alpha^{(0)} c_1^{(0)} = A\Big(1 - \big(\alpha^{(0)}\big)^2\Big), \tag{4.50}$$

which corresponds to equation (4.6) where we set $A = 1$. However, here we use $A = 1/\triangle x$ which gives a reasonable scaling of the final wave function. In other words, the final wave function will be of the same order as the transversal waveguide eigenstates. In case of the excited modes ($m > 0$) the amplitude of the incoming wave is zero. Thus, we have

$$c_0^{(m)} - \alpha^{(m)} c_1^{(m)} = 0, \quad m = 1, ..., M-1. \tag{4.51}$$

On the other hand, the mode coefficients are the projections of the wave function onto the transversal waveguide eigenstates. Using the scalar product (4.48) and the fact that all eigenstates are real-valued we can write the discrete analogue of (4.43) as

$$c_{j_1}^{(m)} = \triangle x \sum_{j_2=j_{21}}^{j_{22}} \phi_{j_1,j_2} \chi_{j_2}^{(m)}, \quad m = 0, ..., M-1. \tag{4.52}$$

The remaining free indices corresponding to the grid points at the left boundary of the ring-shaped quantum device are $0, ..., M-1$. The free indices of the adjacent grid points are $M, ..., 2M-1$ (see Figure 4.10). Thus, using (4.50), (4.51) and (4.52) DTBC at $x_1 = 0$ read:

$$\Big(\triangle x \sum_{j=0}^{M-1} \phi_j \chi_j^{(m)}\Big) - \alpha^{(m)}\Big(\triangle x \sum_{j=M}^{2M-1} \phi_j \chi_j^{(m)}\Big) = (1/\triangle x)\Big(1 - \big(\alpha^{(0)}\big)^2\Big)\delta_{m,0}, \\ m = 0, ..., M-1. \tag{4.53}$$

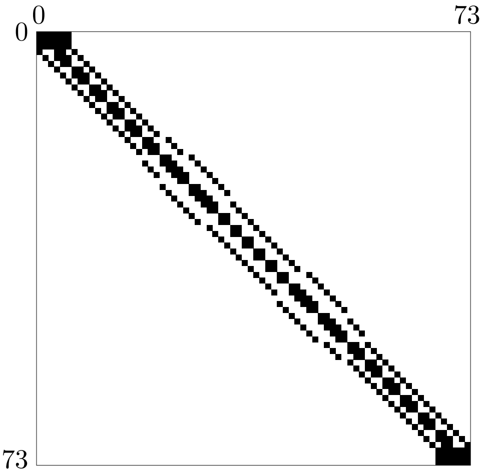

Figure 4.12: Sparsity pattern of S in equation (4.55) corresponding to the example considered in Figure 4.10.

Each of these M equations is used to replace one equation corresponding to a grid point at the left boundary of the reduced mesh. In other words, we replace the first M rows of S according to the left hand side of (4.53).

DTBC at $x_1 = L_1$ follow analogously. However, since we do not prescribe an incoming wave at the right contact, the inhomogeneity does not show up:

$$\Big(\triangle x \sum_{j=N-M}^{N-1} \phi_j \chi_j^{(m)}\Big) - \alpha^{(m)} \Big(\triangle x \sum_{j=N-2M}^{N-M-1} \phi_j \chi_j^{(m)}\Big) = 0, \quad m = 0, ..., M-1. \tag{4.54}$$

The last M rows of S are replaced according to (4.54) which finally yields

$$S\phi = b, \quad \phi = (\phi_0, ..., \phi_{N-1})^\top, \quad b = (b_0, ..., b_{N-1})^\top, \tag{4.55}$$

where $b_j = (1/\triangle x)\Big(1 - \big(\alpha^{(0)}\big)^2\Big)\delta_{j,0}$.

In some numerical experiments we noticed that the condition number of S is quite large. This problem can be easily overcome by scaling all equations (apart from the ones given in (4.53) and (4.54)) with $1/E$. The sparsity pattern of S is depicted in Figure 4.12. Obviously S contains two dense submatrices which are a direct consequence of the DTBC (4.53) and (4.54). For that reason the symmetry of S is lost and consequently many iterative methods can not be applied to solve (4.55). However, the simulations considered below can still be handled by direct solvers.

Perfectly Matched Layers. Similarly to the one-dimensional case we replace the Laplacian in the stationary Schrödinger equation with the Laplace-PML operator

$$\frac{\partial^2}{\partial x_1^2} + \frac{\partial^2}{\partial x_2^2} \to c(x_1)\frac{\partial}{\partial x_1} c(x_1)\frac{\partial}{\partial x_1} + \frac{\partial^2}{\partial x_2^2}, \tag{4.56}$$

which yields the stationary Schrödinger-PML equation:

$$-\frac{\hbar^2}{2m^\star}\left(c(x_1)\frac{\partial}{\partial x_1}c(x_1)\frac{\partial}{\partial x_1}+\frac{\partial^2}{\partial x_2^2}\right)\phi(x_1,x_2)+V(x_1,x_2)\phi(x_1,x_2) \\ = E\phi(x_1,x_2). \tag{4.57}$$

Consequently, outgoing waves decrease exponentially fast with their distance to the device boundaries at $x_1 = 0$ and $x_1 = L_1$. The complex valued function $c(x_1) = 1/(1 + \exp(i\pi/4)\sigma(x_1))$ is the same as in the one-dimensional setting defined in (4.10). We even choose the same cubic absorption function σ, i.e., the width of the PML is $d_{\text{PML}} = 40\,\text{nm}$ and the absorption strength factor is $\sigma_0 = 0.02$.

According to (4.13a) a 2nd-order finite difference discretization of (4.57) is given by

$$-\frac{\hbar^2}{2m^\star}\Bigg(c(x_{j_1})c'(x_{j_1})\frac{-\phi_{j_1-1,j_2}+\phi_{j_1+1,j_2}}{2\triangle x}+c^2(x_{j_1})\frac{\phi_{j_1-1,j_2}-2\phi_{j_1,j_2}+\phi_{j_1+1,j_2}}{(\triangle x)^2} \\ +\frac{\phi_{j_1,j_2-1}-2\phi_{j_1,j_2}+\phi_{j_1,j_2+1}}{(\triangle x)^2}\Bigg)+V_{j_1,j_2}\phi_{j_1,j_2}=E\phi_{j_1,j_2},\ j_1\in\mathbb{Z},\ j_2=0,...,J_2.$$

However, we seek for a solution restricted to the computational domain

$$\Omega_{\text{PML}} = \left\{(X_{j_1}^{\text{PML}}, j_2\triangle x) : j_1 = 0,...,J_1^{\text{PML}},\ j_2 = 0,...,J_2\right\},$$

where $X_{j_1}^{\text{PML}}$ denotes the j_1-th grid point of the one-dimensional grid X_{PML} defined in (4.16). Without taking into account a possible incoming plane wave we can state the problem in the following form:

$$S_{\text{PML}}\phi = 0, \quad \phi_j = \phi_{j_1,j_2}, \quad j = j_1J_2 + j_2, \quad j_1 = 0,...,J_1^{\text{PML}}. \quad j_2 = 0,...,J_2.$$

Here, S_{PML} is given by $S_{\text{PML}} := -\hbar^2/(2m^\star)\tilde{\Delta}_{x_1,x_2} + \text{diag}(d)$ where $\tilde{\Delta}_{x_1,x_2}$ denotes one of the sparse matrices

$$\tilde{\Delta}^{\text{2nd}}_{x_1,x_2} := \left(\tilde{D}^{2,\text{2nd}}_{x_1}\otimes I_{J_2} + I_{J_1^{\text{PML}}}\otimes D^{2,\text{2nd}}_{x_2}\right), \tag{4.58a}$$

$$\tilde{\Delta}^{\text{4th}}_{x_1,x_2} := \left(\tilde{D}^{2,\text{4th}}_{x_1}\otimes I_{J_2} + I_{J_1^{\text{PML}}}\otimes D^{2,\text{4th}}_{x_2}\right), \tag{4.58b}$$

$$\tilde{\Delta}^{\text{6th}}_{x_1,x_2} := \left(\tilde{D}^{2,\text{6th}}_{x_1}\otimes I_{J_2} + I_{J_1^{\text{PML}}}\otimes D^{2,\text{6th}}_{x_2}\right), \tag{4.58c}$$

corresponding to 2nd-, 4th- and 6th-order discretizations of the Laplace-PML operator (4.56). The finite difference matrices corresponding to the x_1-direction are defined via (4.13) and the finite difference matrices acting on the x_2-direction are given in (4.15). Finally, d is defined via $d_j = V_j - E,\ j = 0,...,(J_1^{\text{PML}}+1)(J_2+1)-1$.

Before we realize an incoming plane wave at the left terminal we eliminate all finite difference equations corresponding to grid points where the wave function is supposed to be zero. Like in the case of DTBC we eliminate all rows $S_{\text{PML}}[j,:]$ and colums $S_{\mathrm{PML}}[:, j]$ of S_{PML} with $j \in \{j : V_j > 750\,\mathrm{meV}\}$. Let $N_{\mathrm{PML}} \times N_{\mathrm{PML}}$ denote the new size of S_{PML}. The elimination process implicitly yields a reduced mesh which extends the reduced mesh considered in the case of DTBC (see Figure 4.10). The wave function in the left contact is a superposition of an incoming and a reflected wave $\phi_{j_1,j_2} = \phi^{\mathrm{inc}}_{j_1,j_2} + \phi^{\mathrm{refl}}_{j_1,j_2}$. The incoming wave

$$\phi^{\mathrm{inc}}_{j_1,j_2} = \chi^{(0)}_{j_2} \exp(ikj_1\triangle x), \quad j_1 \le 0, \quad j_2 = j_{21}, ..., j_{22}, \tag{4.59}$$

is a discrete representation of (4.45) wherein $\chi^{(0)}$ is a solution of

$$-\frac{\hbar^2}{2m^\star} D^2_{x_2} \chi^{(0)}_{j_2} + V_{j_2}\chi^{(0)}_{j_2} = E^{(0)}, \quad D^2_{x_2} \in \left(D^{2,\mathrm{2nd}}_{x_2}, D^{2,\mathrm{4th}}_{x_2}, D^{2,\mathrm{6th}}_{x_2}\right), \quad j_2 = j_{21}, ..., j_{22}.$$

Like in the case of DTBC we impose homogeneous Dirichlet BCs at $x_2 = (j_{21}-1)\triangle x$ and $x_2 = (j_{22}+1)\triangle x$. The wave number k is related to the kinetic energy $E^{\mathrm{inc}}_{\mathrm{kin}}$ according to the discrete E–k–relation given in (4.8). However, in case of the higher-order methods we simply use the continuous relation (4.7). Let again M denote the number of free indices along the x_2-direction in the left lead. Moreover, let $j_0, ..., j_0 + M - 1$ denote the free indices of the grid points at $x_1 = 0$ with respect to the reduced mesh (Figure 4.10, $j_0 = 9$). With these notations an incoming plane wave is realized in the same way as in the one-dimensional case. For the 2nd-order discretization we find

$$S_{\mathrm{PML}}\phi = b, \quad \phi = (\phi_0, ..., \phi_{N_{\mathrm{PML}}-1})^\top, \quad b = (b_0, ..., b_{N_{\mathrm{PML}}-1})^\top,$$

where

$$b_j = \begin{cases} -\left(\hbar^2/(2m^\star(\triangle x)^2)\right)\phi^{\mathrm{inc}}_{j+M} & \text{for } j = j_0 - M, ..., j_0 - 1, \\ +\left(\hbar^2/(2m^\star(\triangle x)^2)\right)\phi^{\mathrm{inc}}_{j-M} & \text{for } j = j_0, ..., j_0 + M - 1, \\ 0 & \text{else.} \end{cases}$$

In case of the higher-order discretizations b needs to be adapted accordingly.

Since S_{PML} does not contain dense submatrices it can be assembled more easily than the corresponding matrix in (4.55). On the other hand, depending on the ratio between the number of grid points needed to describe the device domain and the number of grid points needed to realize the PML, the size of S_{PML} may be significantly larger than the size of S in (4.55). Moreover, S_{PML} is not Hermitian. Thus, like in the case of DTBC many iterative methods can not be applied.

Simulations. Before we turn our attention to the ring-shaped quantum device introduced above let us first consider a straight waveguide with parabolic cross section, i.e.,

$$\begin{aligned} V(x_1, x_2) = 1/2\, m^\star\omega_*^2(x_2 - L_2/2)^2, \quad \omega_* = 0.5 \times 10^{14}\,\mathrm{s}^{-1}, \\ x_1 \in \mathbb{R}, \; x_2 \in [0, L_2]. \end{aligned} \tag{4.60}$$

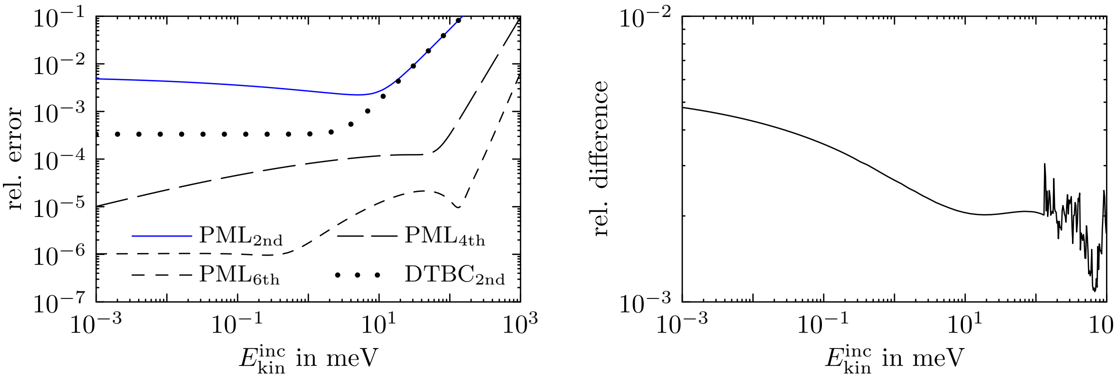

Figure 4.13: Left column: Relative errors as a function of $E_{\text{kin}}^{\text{inc}}$ in a numerical scattering state experiment. The electrons are injected at the left contact of a straight waveguide with parabolic cross section. Right column: Relative differences between the solutions of PML$_{\text{2nd}}$ and DTBC$_{\text{2nd}}$ as a function of $E_{\text{kin}}^{\text{inc}}$. The electrons are injected at the left contact of the ring-shaped waveguide shown in Figure 4.9. In all simulations a mesh size of $\triangle x = 0.5\,\text{nm}$ is used.

The cross-sectional eigenstates and eigenvalues read

$$\begin{aligned} \chi^{(n)}(x_2) &= \left(\frac{m^\star \omega_*}{\pi\hbar}\right)^{1/4} \frac{1}{\sqrt{2^n n!}} H_n\left(\sqrt{\frac{m^\star\omega_*}{\hbar}}(x_2 - L_2/2)\right) \\ &\qquad \times \exp\left(-\frac{1}{2}\frac{m^\star\omega_*}{\hbar}(x_2 - L_2/2)^2\right), \\ E^{(n)} &= \hbar\omega_*\left(n + \frac{1}{2}\right), \; n \in \mathbb{N}_0, \end{aligned} \tag{4.61}$$

where H_n denote the Hermite polynomials [29].

In this trivial example the solution of the scattering state problem outlined above is given by (4.45) wherein $\chi^{(0)}$ is substituted according to (4.61). We compare the exact solution with the results of the different numerical solvers. To this end we set $[0, L_1] \times [0, L_2] = [0, 120] \times [0, 60]\,\text{nm}^2$. The relative errors are depicted in the left column of Figure 4.13 for the energy range $E_{\text{inc}}^{\text{kin}} \in [10^{-3}, 10^{3}]\,\text{meV}$ and $\triangle x = 0.5\,\text{nm}$. As expected, the results resemble the results from the corresponding one-dimensional simulation (Figure 4.2, right column). However, while in the one-dimensional simulation the errors of DTBC$_{\text{2nd}}$ where decreasing continuously for decreasing $E_{\text{kin}}^{\text{inc}}$, they are now bounded from below. This lower bound results from the finite numerical resolution of the transversal waveguide eigenstate $\chi^{(0)}$.

We now consider the ring-shaped quantum device depicted in Figure 4.9. A scattering state solution according to PML$_{\text{2nd}}$ is shown in Figure 4.14 for $E_{\text{kin}}^{\text{inc}} = 21.5\,\text{meV}$. Here and in all subsequent figures, the wave function is scaled by the maximum of the transversal waveguide eigenstate $\chi^{(0)}$. As can be seen the electrons are transmitted almost perfectly through the device. Hence, the reflected wave in

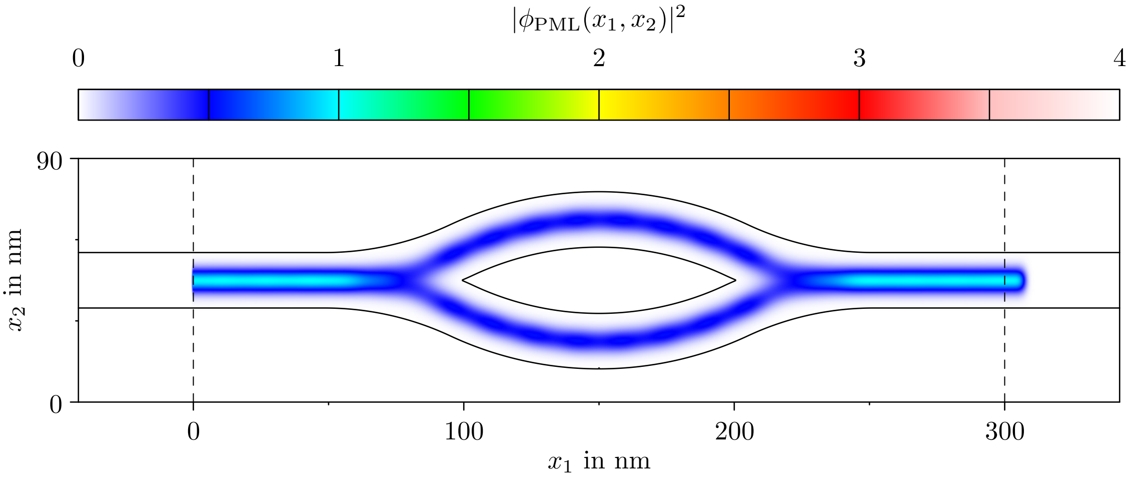

Figure 4.14: Scattering state in the ring-shaped quantum waveguide shown in Figure 4.9. The kinetic energy of the electrons injected at the left contact amounts to $E_{\mathrm{kin}}^{\mathrm{inc}} = 21.5\,\mathrm{meV}$. The black solid line indicates an isoline of the potential energy at 200 meV.

the left terminal is practically zero. Next, we compute scattering state solutions for the energy range $E_{\mathrm{kin}}^{\mathrm{inc}} \in [10^{-3}, 10^{3}]\,\mathrm{meV}$. Clearly, exact solutions are not available. Moreover, our solver using DTBC is restricted to 2nd-order accuracy. For that reason we only compare the solutions corresponding to $\mathrm{DTBC}_{\mathrm{2nd}}$ and $\mathrm{PML}_{\mathrm{2nd}}$. Their relative differences at a spatial resolution of $\triangle x = 0.5\,\mathrm{nm}$ are given in the right column of Figure 4.13. For energies up to approximately 100 meV the results are consistent with the results shown in the left column of Figure 4.13. For larger energies the small wavelength of the wave function can hardly be resolved with 2nd-order methods. Nonetheless, $\mathrm{DTBC}_{\mathrm{2nd}}$ and $\mathrm{PML}_{\mathrm{2nd}}$ yield approximately the same results, even though the relative differences vary almost chaotically.

Finally, we compute the transmission probability as a function of the kinetic energy of the incident electrons. The transmission probability is defined as the ratio between the transmitted and the incident probability current density [28]. In the given situation (provided $E_{\mathrm{kin}}^{\mathrm{inc}}$ is not too large) we have

$$j_{\mathrm{trans}}/j_{\mathrm{inc}} = |\langle \phi(L_1, \cdot), \chi^{(0)} \rangle|^2, \tag{4.62}$$

which is depicted in the left column of Figure 4.17.

4.2.2 Transient scattering states in quantum waveguides

To study the time-evolution of the wave function in a transient scattering state experiment we consider the time-dependent Schrödinger equation

$$i\hbar\partial_t\psi = \hat{H}\psi, \quad \hat{H} = -\hbar^2/2m^\star\Delta + V \tag{4.63}$$

on the infinite stripe $\Omega = \mathbb{R} \times (0, L_2)$. Like in the stationary case we prescribe homogeneous Dirichlet BCs at $x_2 = 0$ and $x_2 = L_2$. Moreover, we assume

$$V(x_1, x_2, t) = V(x_2), \quad x_1 \leq 0, \quad x_1 \geq L_1, \quad x_2 \in [0, L_2].$$

As an example, we refer again to the ring-shaped device described by the potential energy shown in Figure 4.9. In many applications the potentials in the left and right lead are not necessarily the same. Furthermore, they may depend on time via an applied voltage. A typical example is $V(x_1, x_2, t) = V(x_2) - eU(t)$. We note that these extensions could be easily included in the following discussion using the results from Section 4.1.

In a transient scattering state experiment the initial wave function is given by a scattering state solution of the stationary Schödinger equation for the potential energy $V(x_1, x_2, t = 0)$ and the total energy $E = E^{\text{inc}}_{\text{kin}} + E^{(0)}$ where $E^{\text{inc}}_{\text{kin}} = \hbar^2 k^2/(2m^\star)$.

Using time-dependent mode coefficients the wave function in the leads can be decomposed

$$\psi(x_1, x_2, t) = \sum_{m=0}^{\infty} d^{(m)}(x_1, t)\, \chi^{(m)}(x_2), \quad x_1 \leq 0, \quad x_1 \geq L_1 \tag{4.64}$$

into transversal waveguide eigenstates (4.42). Substituting (4.64) into (4.63) shows that each coefficient satisfies a one-dimensional time-dependent Schrödinger equation

$$i\hbar \frac{\partial}{\partial t} d^{(m)}(x_1, t) = -\frac{\hbar^2}{2m^\star} \frac{\partial^2}{\partial x_1^2} d^{(m)}(x_1, t) + E^{(m)} d^{(m)}(x_1, t), \quad t \geq 0, \quad m \in \mathbb{N}_0. \tag{4.65}$$

As an eigenstate of the Schrödinger equation the scattering state evolves in time according to $\exp(-i\omega t)$ with $\omega = E/\hbar$. Hence, the time-evolution of the scattering state in the leads is given by

$$\sum_{m=0}^{\infty} \exp(-iEt/\hbar)\, c^{(m)}(x_1)\, \chi^{(m)}(x_2), \quad x_1 \leq 0, \quad x_1 \geq L_1,$$

wherein

$$e^{(m)}(x_1, t) := \exp(-iEt/\hbar) c^{(m)}(x_1)$$

solves (4.65) as well. Consequently, $\exp(iE^{(m)}t/\hbar) d^{(m)}$ and $\exp(iE^{(m)}t/\hbar) e^{(m)}$ solve the free time-dependent one-dimensional Schrödinger equation and therefore transparent boundary conditions at $x_1 = 0$ and $x_1 = L_1$ could be derived by the application of (3.16a) and (3.16b) to

$$\exp(iE^{(m)}t/\hbar) d^{(m)} - \exp(iE^{(m)}t/\hbar) e^{(m)} \tag{4.66}$$

for each $m \in \mathbb{N}_0$.

Discrete transparent boundary conditions. Using the same grid Ω_{DTBC} as in the stationary case we can formulate the Crank-Nicolson scheme for the two-dimensional time-dependent Schrödinger equation (4.63) as follows:

$$\begin{gathered}
P\psi^{(n+1)} = Q\psi^{(n)}, \;\; \psi_j^{(n)} = \psi_{j_1,j_2}^{(n)}, \;\; j = j_1 J_2 + j_2, \\
j_1 = 0, ..., J_1, \;\; j_2 = 0, ..., J_2, \;\; n \in \mathbb{N}_0.
\end{gathered} \tag{4.67}$$

Here, P and Q are sparse matrices

$$\begin{aligned}
P &:= I - i\triangle t\hbar/(4m^\star)\Delta^{\mathrm{2nd}}_{x_1,x_2} + i\triangle t/(2\hbar)\,\mathrm{diag}\left(V^{(n+1/2)}\right), \\
Q &:= I + i\triangle t\hbar/(4m^\star)\Delta^{\mathrm{2nd}}_{x_1,x_2} - i\triangle t/(2\hbar)\,\mathrm{diag}\left(V^{(n+1/2)}\right),
\end{aligned}$$

and $V^{(n+1/2)}$ denotes the vector $\left(V_0^{(n+1/2)}, ..., V_{J_1 J_2 - 1}^{(n+1/2)}\right)^\top$. As outlined in Section 4.2.1 we eliminate all finite difference equations corresponding to grid points where the wave function is zero. Needless to say, we eliminate the same rows and columns of P and Q which have been eliminated in S (see Section 4.2.1). Let $N \times N$ denote the new size of P and Q. Using the same notations as in Section 4.2.1 the wave function in the leads of the reduced mesh reads

$$\psi_{j_1,j_2}^{(n)} = \sum_{m=0}^{M-1} d_{j_1}^{(m,n)} \chi_{j_2}^{(m)}, \quad j_1 \le 0, \quad j_1 \ge J_1, \quad j_2 = j_{21}, ..., j_{22}.$$

In order to derive DTBC at $x_1 = 0$ and $x_1 = L_1$ we employ the same strategy as in the continuous case considered above. The discrete analogue of (4.66) reads

$$\epsilon^{(m,n)} d_{j_1}^{(m,n)} - \gamma^{(m,n)} c_{j_1}^{(m)} \tag{4.68}$$

wherein the discrete gauge change terms

$$\begin{aligned}
\epsilon^{(m,n)} &= \exp\left(2in\arctan(\triangle t E^{(m)}/(2\hbar))\right) \approx \exp\left(iE^{(m)}t/\hbar\right), \\
\gamma^{(m,n)} &= \exp(2in(\arctan(\triangle t E^{(m)}/(2\hbar)) - \arctan(\triangle t E/(2\hbar)))) \\
&\approx \exp(iE^{(m)}t/\hbar)\exp(-iEt/\hbar), \quad m = 0, ..., M-1, \; n \in \mathbb{N}_0,
\end{aligned}$$

are slight modifications of (4.39). Applying (3.17a) and (3.17b) to (4.68) yields DTBC

$$\begin{aligned}
\epsilon^{(m,n+1)} d_1^{(m,n+1)} - s^{(0)}\epsilon^{(m,n+1)} d_0^{(m,n+1)} &= \sum_{\ell=1}^{n} s^{(n+1-\ell)} \left(\epsilon^{(m,\ell)} d_0^{(m,\ell)} - \gamma^{(m,\ell)} c_0^{(m)}\right) \\
- \left(\epsilon^{(m,n)} d_1^{(m,n)} - \gamma^{(m,n)} c_1^{(m)}\right) &+ \gamma^{(m,n+1)} c_1^{(m)} - s^{(0)}\gamma^{(m,n+1)} c_0^{(m)},
\end{aligned} \tag{4.69a}$$

$$\begin{aligned}
\epsilon^{(m,n+1)} d_{J_1-1}^{(m,n+1)} - s^{(0)}\epsilon^{(m,n+1)} d_{J_1}^{(m,n+1)} &= \sum_{\ell=1}^{n} s^{(n+1-\ell)} \left(\epsilon^{(m,\ell)} d_{J_1}^{(m,\ell)} - \gamma^{(m,\ell)} c_{J_1}^{(m)}\right) \\
- \left(\epsilon^{(m,n)} d_{J_1-1}^{(m,n)} - \gamma^{(m,n)} c_{J_1-1}^{(m)}\right) &+ \gamma^{(m,n+1)} c_{J_1-1}^{(m)} - s^{(0)}\gamma^{(m,n+1)} c_{J_1}^{(m)}
\end{aligned} \tag{4.69b}$$

at the left and right contact, respectively. The mode coefficients appearing on the left-hand side of (4.69) are implicitly given by the projection of the new wave function onto the transversal waveguide eigenstates

$$d_0^{(m,n+1)} = \triangle x \sum_{j=0}^{M-1} \psi_j^{(n+1)} \chi_j^{(m)}, \qquad d_1^{(m,n+1)} = \triangle x \sum_{j=M}^{2M-1} \psi_j^{(n+1)} \chi_j^{(m)},$$

$$d_{J_1-1}^{(m,n+1)} = \triangle x \sum_{j=N-2M}^{N-M-1} \psi_j^{(n+1)} \chi_j^{(m)}, \qquad d_{J_1}^{(m,n+1)} = \triangle x \sum_{j=N-M}^{N-1} \psi_j^{(n+1)} \chi_j^{(m)}.$$

Finally, all remaining equations in (4.67) which correspond to grid points at the left and right device contacts are replaced. In the particular example of the reduced mesh shown in Figure 4.10, the first M equations are replaced according to (4.69a) and the last M equations are replaced according to (4.69b). The left-hand sides of (4.69) cause dense submatrices in P which need to be updated in each time step. All quantities appearing on the right-hand side of (4.69) are already known (at the n-th time step) or can easily be computed. However, to be able to perform the next time step we need to store all values of $d_0^{(m,\ell)}$ and $d_{J_1}^{(m,\ell)}$ for $m = 0, ..., M-1$ and $\ell = 1, ..., n$. Hence, the storage requirements for the DTBC are in $\mathcal{O}(Mn_\star)$ where $n_\star$ denotes the total number of time steps. Furthermore, the computational time required for a single evaluation of the discrete convolutions in (4.69) increases linearly with n and thus the total time complexity is in $\mathcal{O}(Mn_\star^2)$.

Perfectly Matched Layers. Substituting the Laplacian in the time-dependent Schrödinger equation with the Laplace-PML operator (4.56) gives the time-dependent Schrödinger-PML equation:

$$\begin{aligned} i\hbar \frac{\partial}{\partial t}\psi(x_1,x_2,t) = -\frac{\hbar^2}{2m^\star}\left(c(x_1)\frac{\partial}{\partial x_1}c(x_1)\frac{\partial}{\partial x_1} + \frac{\partial^2}{\partial x_2^2}\right)\psi(x_1,x_2,t) \\ + V(x_1,x_2,t)\psi(x_1,x_2,t). \end{aligned}$$

The semi-discretized problem on Ω_{PML} reads

$$\begin{gathered} \frac{d}{dt}\psi_j(t) = i\frac{\hbar}{2m^\star}\tilde{\Delta}_{x_1,x_2}\psi_j(t) - \frac{i}{\hbar}V(t)\psi_j(t), \quad \psi_j(t) = \psi_{j_1,j_2}(t), \\ j = j_1 J_2 + j_2, \quad j_1 = 0, ..., J_1^{\text{PML}}, \quad j_2 = 0, ..., J_2, \end{gathered}$$

where $\tilde{\Delta}_{x_1,x_2}$ denotes one of the sparse matrices defined in (4.58) corresponding to 2nd-, 4th- and 6th-order spatial discretizations. For the time-integration method we employ the Crank-Nicolson or the classical Runge Kutta method given in (4.25) and (4.30), respectively. Like in the stationary case we eliminate all equations corresponding to grid points where the wave function is assumed to be zero. The incoming plane wave (4.59) used in the stationary problem becomes time-dependent according to the oscillation $\exp(-i\omega t)$. In case of the 2nd-order discretization ω is related to the total energy E according to (4.35). Otherwise we simply use $\omega = E/\hbar$. A time-dependent incoming wave can be included analogously to the one-dimensional case outlined in Section 4.1.3. In particular we refer to the modifications in (4.36). For the sake of brevity, we omit the details. The storage requirements for the PML are in $\mathcal{O}(MJ_1^\star)$ where $J_1^\star$ denotes the number of indices j_1 with $X_{j_1}^{\mathrm{PML}} < 0$ or $X_{j_1}^{\mathrm{PML}} > L_1$. Contrary to DTBC the computational time required to perform one time step is constant.

Simulations. In the simple example of the straight waveguide (4.60) the solution of the transient scattering state problem outlined above is given by

$$\psi(x_1, x_2, t) = \exp(ikx_1 - i\omega t)\chi^{(0)}(x_2),$$
$$\omega = E/\hbar, \;\; E = E_{\mathrm{kin}}^{\mathrm{inc}} + E^{(0)}, \;\; E_{\mathrm{kin}}^{\mathrm{inc}} = \hbar^2 k^2/(2m^\star),$$

in which $\chi^{(0)}$ and $E^{(0)}$ are substituted according to (4.61). We compare the exact solution with the results of the different numerical solvers. To this end we set $[0, L_1] \times [0, L_2] = [0, 120] \times [0, 60]\,\mathrm{nm}^2$. The kinetic energy of the incoming electrons amounts to $E_{\mathrm{kin}}^{\mathrm{inc}} = 21.5\,\mathrm{meV}$. For the time-integration we either employ the Crank-Nicolson method or the classical Runge-Kutta method. In case of the Crank-Nicolson method we use $\triangle x = 0.5\,\mathrm{nm}$ and $\triangle t = 0.25\,\mathrm{fs}$. We note that this choice is rather expensive since we need to solve a linear system of equations in each time step. In case of the Runge-Kutta method we use the same spatial mesh size but a time step size of $\triangle t \lesssim 0.05\,\mathrm{fs}$ is needed to ensure stability. However, despite of this small time step size the computation times are the shortest compared to the computation times of all other solvers. The relative errors are shown in the left column of Figure 4.15.

The numerical methods derived above can be easily modified to allow for simulations of wave packets in quantum waveguides. For instance, to simulate wave packets using the solver corresponding to DTBC we set $c_0^{(m)} = c_1^{(m)} = c_{J_1-1}^{(m)} = c_{J_1}^{(m)} = 0$ in (4.69) for all $m = 0, ..., M-1$. In case of PML we simply omit the incoming wave at the device contact. In the following experiment we consider the time-evolution of two superimposed wave packets in the straight waveguide with parabolic cross section. More precisely, we start the numerical calculations using the exact solution

$$\psi(x_1, x_2, t) := \xi(x_1, t)\exp(-iE^{(0)}t/\hbar)\chi^{(0)}(x_2) + \xi(x_1, t)\exp(-iE^{(1)}t/\hbar)\chi^{(1)}(x_2),$$

at $t = 0\,\mathrm{ps}$. The one-dimensional gaussian ξ is defined in (4.32). We use the same parameters except for $k = \sqrt{2m^\star\, 21.5\,\mathrm{meV}}/\hbar$. The transversal waveguide eigenstates and eigenvalues are given in (4.61). For the numerical simulation we set $[0, L_1] \times [0, L_2] = [0, 160 \times [0, 60]\,\mathrm{nm}^2$. The relative errors are depicted in the right column of Figure 4.15. As can be seen $\mathrm{DTBC}_{\mathrm{2nd}}^{\mathrm{CN}}$ and $\mathrm{PML}_{\mathrm{2nd}}^{\mathrm{CN}}$ yield very similar results which is in contrast to the one-dimensional results shown in Figure 4.5. However, in this simulation the wave packet is confined to a narrow channel. As a consequence the wave function does not only oscillate in the longitudinal direction but also in the vertical direction. For the given cross section of the waveguide (characterized by

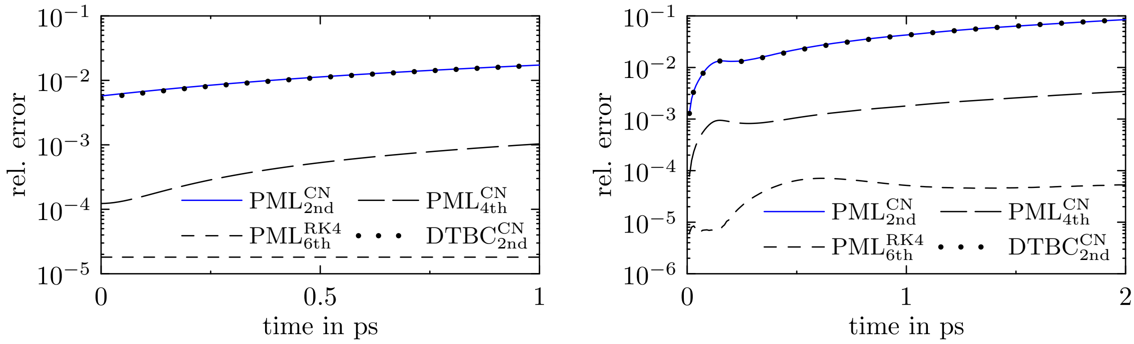

Figure 4.15: Left column: Relative errors of the numerical solutions as a function of time in a transient scattering state experiment. The device is a simple straight waveguide with parabolic cross section and the energy of the injected electrons amounts to $E^{\mathrm{inc}}_{\mathrm{kin}} = 21.5\,\mathrm{meV}$. Right column: Relative errors corresponding to the simulation of two superimposed wave packets in a straight waveguide with parabolic cross section. In all simulations a mesh size of $\triangle x = 0.5\,\mathrm{nm}$ is used. In case of the Crank-Nicolson time-integration method the time step size is given by $\triangle t = 0.25\,\mathrm{fs}$. In case of the Runge-Kutta time-stepping method we use $\triangle t = 0.05\,\mathrm{fs}$.

$\omega_* = 0.5 \times 10^{14}\,\mathrm{s}^{-1}$) we find $E^{(0)} \approx 16.45\,\mathrm{meV}$ and $E^{(1)} \approx 49.36\,\mathrm{meV}$. The oscillation corresponding to the 2nd energy can not easily be resolved by 2nd-order methods at the given spatio-temporal resolution. As a consequence the discretization of the boundary conditions plays a minor role and thus $\mathrm{DTBC}^{\mathrm{CN}}_{\mathrm{2nd}}$ and $\mathrm{PML}^{\mathrm{CN}}_{\mathrm{2nd}}$ yield approximately the same results. We note that for decreasing ω_* the confinement in the x_2-direction becomes less important. In such a case, the numerical results would indeed be similar to the numerical results of the one-dimensional calculations considered in Section 4.1.

4.2.3 Details of the implementation

All simulations of this article are realized in the *Python* programming language using the numerical tools available in *SciPy* [46]. One of the crucial steps is the assembling of the sparse matrices related to the solvers using DTBC. Since these matrices contain small but dense submatrices one needs to proceed carefully. However, using fast routines to convert dense to sparse matrices followed by a series of sparse `vstack`- and `hstack`-operations this task can be realized efficiently. Another crucial step is the computation of the discrete convolution terms in (4.69a) and (4.69b). To this end we employ parallelized *C*-functions which can be included easily in *Python* programs. All linear systems are solved using direct solvers for sparse matrices which is the most time-consuming part in the stationary and transient algorithms. We note that no linear system needs to be solved if the time evolution is computed using the explicit Runge-Kutta method. The timings reported below correspond to an Intel

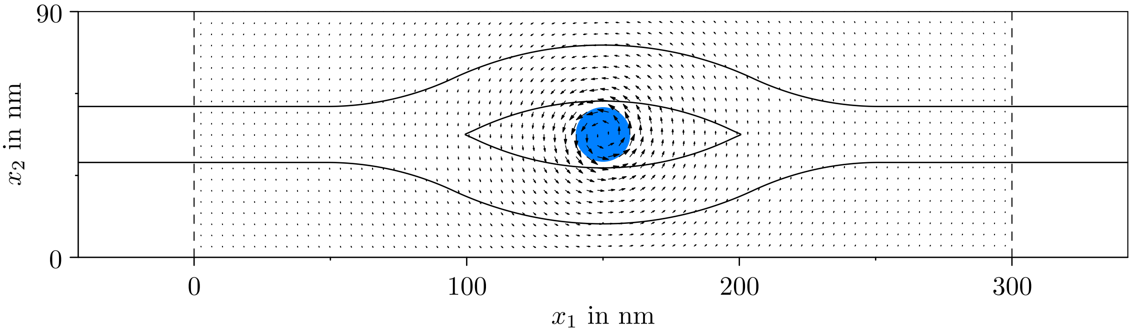

Figure 4.16: Vector potential (arrows) and magnetic field (blue disk) in the ring-shaped quantum waveguide device depicted in Figure 4.9. The black solid line indicates an isoline of the potential energy at 200 meV.

Core i7-4770K CPU @ 3.50GHz × 8.

4.3 The Aharonov-Bohm effect

We consider the ring-shaped quantum waveguide depicted in Figure 4.9, but now we additionally take into account a homogeneous magnetic field which is applied perpendicular to the x_1x_2-plane and which is assumed to vanish outside a circle of radius $r_0 = 10\,\mathrm{nm}$ centered at $(L_1/2, L_2/2)$. For a charged particle in an electromagnetic field the Hamiltonian of the Schrödinger equation reads

$$\hat{H} = \left(\hat{p} - qA\right)^2 \big/ (2m^\star) + q\Phi, \quad \hat{p} = -i\hbar\nabla, \tag{4.70}$$

wherein q is the charge of the particle and A, Φ denote the vector and scalar potential, respectively. The electric and magnetic fields can be expressed in terms of A and Φ via $E = -\partial_t A - \nabla\Phi$ and $B = \nabla \times A$. In the simulations below the vector potential is given by

$$A(x_1, x_2, x_2) := B_0\tilde{A}(x_1 - L_1/2, x_2 - L_2/2, x_3), \tag{4.71}$$

with

$$\tilde{A}(x_1, x_2, x_3) = \begin{cases} 1/2\,(-x_2, x_1, 0)^\top, & \text{if } \sqrt{x_1^2 + x_2^2} \le r_0, \\ r_0^2/(2(x_1^2 + x_2^2))\,(-x_2, x_1, 0)^\top, & \text{if } \sqrt{x_1^2 + x_2^2} > r_0. \end{cases}$$

Accordingly, the magnetic field reads

$$B = \begin{cases} (0, 0, B_0)^\top, & \text{if } \sqrt{(x_1 - L_1/2)^2 + (x_2 - L_2/2)^2} \le r_0, \\ (0, 0, 0), & \text{if } \sqrt{(x_1 - L_1/2)^2 + (x_2 - L_2/2)^2} > r_0. \end{cases}$$

An illustration of $\tilde{A}$ and B is given in Figure 4.16. The scalar potential Φ is defined via $V = -e\Phi$.

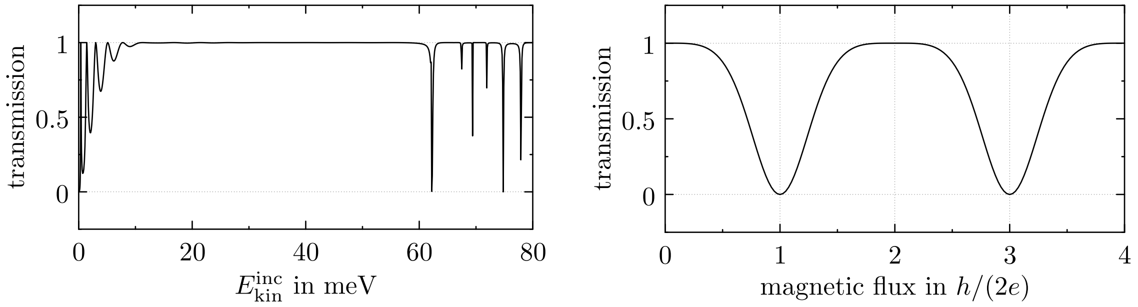

Figure 4.17: Left column: Transmission probability as a function of $E_{\mathrm{kin}}^{\mathrm{inc}}$ for electrons injected at the left terminal of the ring-shaped device shown in Figure 4.9. Right column: Transmission probability as a function of the magnetic flux in multiples of the flux quantum. The energy of the incoming electrons is fixed at $E_{\mathrm{kin}}^{\mathrm{inc}} = 21.5\,\mathrm{meV}$.

Our choice of A and Φ is by no means unique. Replacing A with $A + \nabla\Lambda$ and Φ with $\Phi - \partial_t\Lambda$ where $\Lambda = \Lambda(x,t)$ is a scalar function has no effect on E and B. Such a transformation is called a gauge transformation and a specific choice of A and Φ is called a gauge potential. In order to fix A and Φ one needs to impose a gauge condition. Here we have $\nabla \cdot A = 0$ which is also being referred to as the symmetric or Coulomb gauge. Using

$$(\hat{p} - qA)^2 = -\hbar^2\Delta + iq\hbar\,\nabla\cdot A + 2iq\hbar\,A\cdot\nabla + q^2A^2,$$

the gauge condition and the charge of the electron $q = -e$ the Hamiltonian in (4.70) becomes

$$\hat{H} = -\frac{\hbar^2}{2m^\star}\Delta - i\frac{e\hbar}{m^\star}A\cdot\nabla + \frac{e^2}{2m^\star}A^2 + V. \tag{4.72}$$

Thus, to include the magnetic field into the numerical methods developed in Section 4.2 we need to discretize two additional terms. The boundary conditions remain unchanged provided that the vector potential vanishes in the exterior domains. In the numerical simulations we set $A(x_1,x_2,x_3) = 0$ for $x_1 < \delta$ and $x_1 > L_1 - \delta$ ($\delta \approx 2.5\,\mathrm{nm}$) which is not consistent with (4.71). However, the development of DTBC in the presence of the vector potential (4.71), if at all possible, would be a challenging task. Here we simply choose L_1 such that $|A(x_1,x_2,x_3)|$ becomes small for $x_1 < \delta$ and $x_1 > L_1 - \delta$. As a result the modelling error becomes small too, which can be verified by further increasing L_1. The term $e^2/(2m^\star)A^2$ in (4.72) is discretized in the same way as the potential energy. Using the notations corresponding to the case of DTBC described in Section 4.2, the convection term $-ie\hbar/m^\star A\cdot\nabla$ is discretized as follows:

$$A\cdot\nabla \approx \mathrm{diag}(A_1)D_{x_1}^1 \otimes I_{J_2} + \mathrm{diag}(A_2)I_{J_1} \otimes D_{x_2}^1.$$

Here, $D_{x_1}^1$ and $D_{x_2}^1$ are defined according to (4.14) and A_1, A_2 denote the first and second component of the vector potential A, i.e., $(A_{1,2})_j = (A_{1,2})_{j_1,j_2}$, $j = j_1J_2 + j_2$,

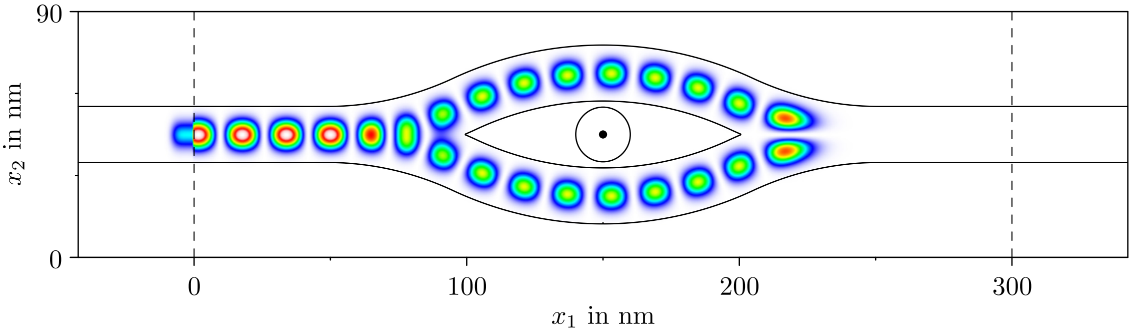

Figure 4.18: Scattering state solution in a ring-shaped quantum device using the same colormap as in Figure 4.14. The kinetic energy of the electrons injected at the left contact amounts to $E_{\text{kin}}^{\text{inc}} = 21.5\,\text{meV}$ and the magnetic flux through the encircled area is given by $\Phi_B = h/(2e)$. The black solid line indicates an isoline of the potential energy at 200 meV.

$j_1 = 0, ..., J_1$, $j_2 = 0, ..., J_2$. The new terms can be easily included into the stationary and transient methods outlined in Section 4.2.

Let us consider the stationary case first. In particular, we are interested in the transmission probability (4.62) as a function of the magnetic flux $\Phi_B = B_0 \pi r_0^2$ (not to be confused with the scalar potential Φ). To this end we compute scattering state solutions of the stationary Schrödinger equation using the Hamiltonian (4.72). Like in Section 4.2 we consider electrons injected at the left terminal travelling to the right. While the magnetic flux is increased in each calculation we keep the kinetic energy of the incoming electrons fixed at $E_{\text{kin}}^{\text{inc}} = 21.5\,\text{meV}$. The right column of Figure 4.17 shows the computed transmission probability as a function of the magnetic flux in multiples of the flux quantum $\Phi_0 = h/(2e)$ which is a fundamental constant in condensed matter physics. As can be seen the transmission probability oscillates almost perfectly with increasing values of the magnetic flux. These oscillations are a manifestation of the well-known Aharonov-Bohm effect [1]. In fact, quantum mechanics implies that electrons traveling along a Path P where $\nabla \times A = 0$ accumulate a phase shift $\varphi = -e/\hbar \int_P A \cdot dx$. Hence, using Stokes' theorem the phase difference between the beam of electrons taking the upper path P_1 and the beam of electrons taking the lower path P_2 (see Figure 4.16) is given by

$$\varphi_1 - \varphi_2 = -e/\hbar \left(\int_{P_1} A \cdot dx - \int_{P_2} A \cdot dx \right) = -(e/\hbar)\Phi_B.$$

Therefore, the interference of the two electron beams depends solely on the enclosed magnetic flux. The remarkable thing is that the electrons are affected by the vector potential even in regions where the magnetic field is zero which is in strong contrast to classical mechanics. As an example Figure 4.18 shows the scattering state solution for $\Phi_B = h/(2e)$ corresponding to the destructive interference condition $|\varphi_1 - \varphi_2| = \pi$. For the calculations we employed 2nd-order spatial discretizations with $\triangle x =$

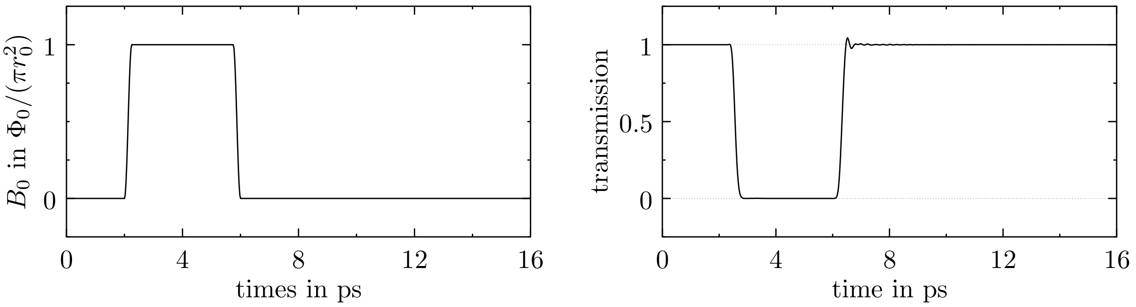

Figure 4.19: Magnetic field and transmission probability as a function of time.

0.5 nm which corresponds to linear systems of size $N_{\mathrm{DTBC}} = 66\,264$ and $N_{\mathrm{PML}} = 79\,694$. The relative difference between the solutions computed using DTBC and PML is approximately 2×10^{-3}. This value is almost independent from the magnetic flux.

We finally turn our attention to the Aharonov-Bohm effect in the transient regime. In particular we consider a transient scattering state experiment with a time-dependent vector potential (4.71). More precisely, we let B_0 change in time as depicted in the left column of Figure 4.19. Like in the stationary case we keep the kinetic energy of the incoming electrons fixed at $E_{\mathrm{kin}}^{\mathrm{inc}} = 21.5\,\mathrm{meV}$. Initially the magnetic field is switched off and thus the initial wave function corresponds to the scattering state shown in Figure 4.14. The time evolution of the wave function is illustrated in Figure 4.20. Simultaneously we consider the transmission probability as a function of time in the right column of Figure 4.19. Between $t = 2\,\mathrm{ps}$ and $t = 2.25\,\mathrm{ps}$ the magnetic field is increased to a value of $B_0 = \Phi_0/(\pi r_0^2)$ which corresponds to the destructive interference condition considered in the stationary case. The effect on the wave function becomes apparent with a short delay (Fig. 4.20, $t = 2.5\,\mathrm{ps}$) and, as expected, the transmission probability decreases. Another 1.5 ps later the wave function has effectively adopted the scattering state corresponding to the destructive interference condition (Fig. 4.20, $t = 4\,\mathrm{ps}$). During the period from $t = 6\,\mathrm{ps}$ to $t = 6.25\,\mathrm{ps}$ the magnetic field is turned off. Again the wave function starts to evolve in a rather wild manner (Fig. 4.20, $t = 6.25\,\mathrm{ps}$). Only a short time later the transmission probability recovers its old value. However, the wave function does not return to its initial state. Instead, we observe strong oscillations restricted to the interior part of the waveguide. Even after another 9.75 ps these oscillations are still present (Fig. 4.20, $t = 16\,\mathrm{ps}$) and in fact they will persist for all time. This can be demonstrated by decreasing the amplitude of the incoming wave after the second switching operation (which is realized easily in case of PML). A short time later we are left with an oscillating wave packet which is bound to the region of the ring. The result of such a numerical simulation is depicted in Figure 4.20 ($t^\star = 16\,\mathrm{ps}$). In this particular example the amplitude of the incoming wave was multiplied by a factor of 0.999 before each time step with $t \geq 12\,\mathrm{ps}$. The remaining

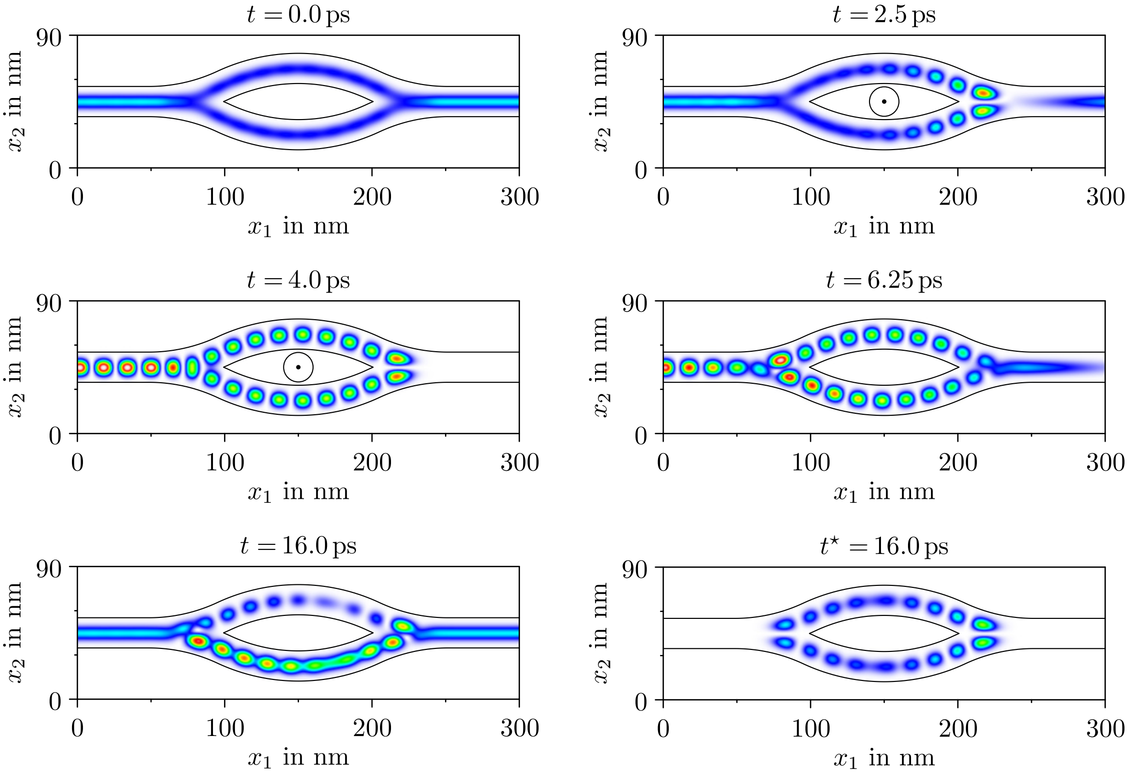

Figure 4.20: Time-evolution of the wave function (probability density) in a transient scattering state experiment with time-dependent magnetic field. The colormap is the same as in Figure 4.14.

wave packet is supposed to be a superposition of several eigenstate solutions to the stationary Schrödinger equation. We note that the probability density of a superposition of several eigenstates is time-dependent. Two eigenstates corresponding to the eigenvalues $E \approx 33.2\,\mathrm{meV}$ and $E \approx 52.8\,\mathrm{meV}$ are shown in Figure 4.21 but in fact there are many more eigenstates. The oscillations superimposed to the final wave function are caused by the fast variation of the magnetic field. In case where B_0 is varied quasi-adiabatically (on the time-scale of about $10\,\mathrm{ps}$) no bound states are excited and hence no oscillations emerge.

The simulation was carried out using the 2nd-order Crank-Nicolson scheme. Alternatively we used the Runge-Kutta time-integration method in combination with a 6th-order spatial discretization and PML. In case of the Crank-Nicolson scheme we employed a spatial resolution of $\triangle x = 1\,\mathrm{nm}$ and a time-step size of $\triangle t = 0.5\,\mathrm{fs}$. Compared to the simulations presented in the previous sections this discretization appears to be rather coarse but it should be noted that in the example presented above we have to solve 32 000 linear systems of size $N_{\mathrm{DTBC}} = 16\,536$ and $N_{\mathrm{PML}} = 20\,046$. If the time evolution is computed using the classical Runge-Kutta method no linear system needs to be solved at all (except for the initial scattering state). However,

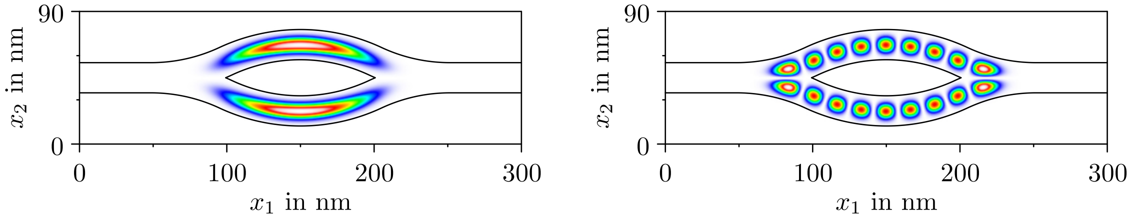

Figure 4.21: Eigenstate solutions to the stationary Schrödinger equation corresponding to the eigenvalues $E \approx 33.2\,\mathrm{meV}$ and $E \approx 52.8\,\mathrm{meV}$. The probability densities where scaled by their maximum values.

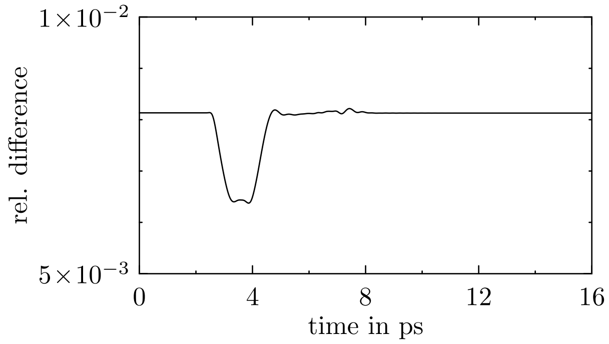

Figure 4.22: Relative difference between the numerical solutions of $\mathrm{DTBC}^{\mathrm{CN}}_{\mathrm{2nd}}$ and $\mathrm{PLM}^{\mathrm{CN}}_{\mathrm{2nd}}$ as a function of time for $\triangle x = 1\,\mathrm{nm}$ and $\triangle t = 0.5\,\mathrm{fs}$.

the resulting numerical scheme is only conditionally stable and hence we can not use the same time step size as in case of the Crank-Nicolson method. At a spatial resolution of $\triangle x = 1\,\mathrm{nm}$ we are forced to use a time step size no larger than $\triangle t = 0.25\,\mathrm{fs}$ which agrees well with condition (4.31).

Comparing the simulations on a reduced mesh (see Section 4.2) with the simulations using the full grid we found that the results are practically the same. Thus, we did not change the underlying physics by imposing artificial Dirichlet BCs at a distance too close to the center of the waveguides. Eliminating all finite difference equations corresponding to grid points where the wave function is effectively zero reduces the size of the linear systems by more than 40 percent and, as a consequence, the time needed to solve the linear systems decreases by more than 50 percent.

The relative difference between the numerical solutions of $\mathrm{DTBC}^{\mathrm{CN}}_{\mathrm{2nd}}$ and $\mathrm{PML}^{\mathrm{CN}}_{\mathrm{2nd}}$ is shown in Figure 4.22. Compared to the relative differences seen in the simulations of the previous sections, the difference of both numerical solutions is relatively large. This is due to the coarse spatial resolution of $\triangle x = 1\,\mathrm{nm}$ which is twice as large as the resolution employed before. Indeed, a spatial resolution of $\triangle x = 0.5\,\mathrm{nm}$ yields the same level of accuracy as in the previous sections but the simulation becomes extremely time-consuming.

We finally consider the computing times corresponding to the above mentioned

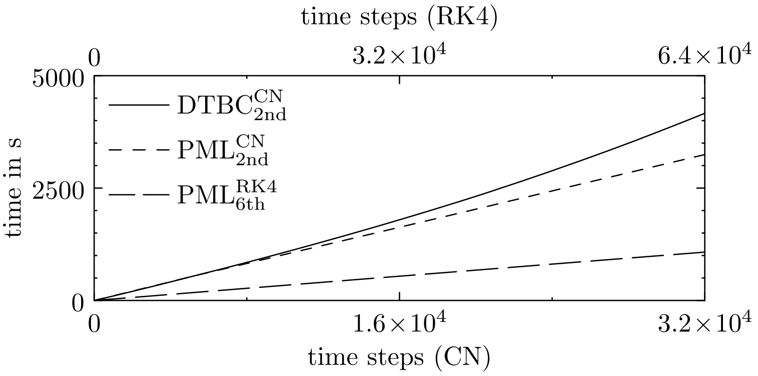

Figure 4.23: Computing times as a function of the number of time steps.

methods as depicted in Figure 4.23. Initially DTBC$^{\mathrm{CN}}_{\mathrm{2nd}}$ performs slightly better than PML$^{\mathrm{CN}}_{\mathrm{2nd}}$. However, the computing time of DTBC$^{\mathrm{CN}}_{\mathrm{2nd}}$ scales quadratically with the number of time steps and therefore simulations involving even more time steps become very expensive. We note that this problem could be overcome using the techniques discussed in Section 3.2.2. As expected, the computing times of the solvers using PML increase linearly. Interestingly, PML$^{\mathrm{RK4}}_{\mathrm{6th}}$ performs significantly faster than the other methods. At the same time, it is also the most accurate method and its implementation is relatively simple.

Bibliography

[1] Y. Aharonov and D. Bohm. Significance of electromagnetic potentials in the quantum theory. *Phys. Rev.*, 115:485–491, 1959.

[2] X. Antoine, A. Arnold, C. Besse, M. Ehrhardt, and A. Schädle. A review of transparent and artificial boundary conditions techniques for linear and nonlinear Schrödinger equations. *Commun. Comput. Phys.*, 4:729–796, 2008.

[3] X. Antoine and C. Besse. Unconditionally stable discretization schemes of nonreflecting boundary conditions for the one-dimensional Schrödinger equation. *J. Comput. Phys.*, 188:157–175, 2003.

[4] J. Appenzeller, Ch. Schroer, Th. Schäpers, A. v. d. Hart, A. Förster, B. Lengeler, and H. Lüth. Electron interference in a T-shaped quantum transistor based on Schottky-gate technology. *Phys. Rev. B*, 53:9959–9963, 1996.

[5] A. Arnold. Numerically absorbing boundary conditions for quantum evolution equations. *VLSI Design*, 6:313–319, 1998.

[6] A. Arnold. Mathematical concepts of open quantum boundary conditions. *Transport Theory and Statistical Physics*, 30:561–584, 2001.

[7] A. Arnold, M. Ehrhardt, M. Schulte, and I. Sofronov. Discrete transparent boundary conditions for the Schrödinger equation on circular domains. *Commun. Math. Sci.*, 10:889–916, 2012.

[8] A. Arnold, M. Ehrhardt, and I. Sofronov. Discrete transparent boundary conditions for the Schrödinger equation: Fast calculation, approximation, and stability. *Commun. Math. Sci.*, 1:501–556, 2003.

[9] A. Arnold and M. Schulte. Transparent boundary conditions for quantum-waveguide simulations. *Mathematics And Computers In Simulation*, 79:898–905, 2008.

[10] Anton Arnold. Mathematical properties of quantum evolution equations. In Naoufel Ben Abdallah and Giovanni Frosali, editors, *Quantum Transport*, volume 1946 of *Lecture Notes in Mathematics*, pages 45–109. Springer Berlin Heidelberg, 2008.

[11] W. Bao, S. Jin, and P. Markowich. On time-splitting spectral approximations for the Schrödinger equation in the semiclassical regime. *J. Comput. Phys.*, 175:487–524, 2002.

[12] V. A. Baskoakov and A. V. Popov. Implementation of transparent boundaries for numerical solution of the Schrödinger equation. *Wave Motion*, 14:123–128, 1991.

[13] H. Batelaan and A. Tonumura. The Aharonov-Bohm effects: Variations on a subtle theme. *Phys. Today*, 62:38–43, 2009.

[14] N. Ben Abdallah, P. Degond, and P. A. Markowich. On a one-dimensional Schrödinger-Poisson scattering model. *Z. Angew. Math. Phys.*, 48:135–155, 1997.

[15] Naoufel Ben Abdallah and Ali Faraj. An improved transient algorithm for resonant tunneling. *Preprint arXiv:1005.0444*, May 2010.

[16] Naoufel Ben Abdallah and Olivier Pinaud. Multiscale simulation of transport in an open quantum system: Resonances and WKB interpolation. *J. Comput. Phys.*, 213:288–310, 2006.

[17] J. P. Bérenger. A perfectly matched layer for the absorption of electromagnetic waves. *J. Comput. Phys.*, 114:185–200, 1994.

[18] Alfredo Bermúdez, L. Hervella-Nieto, A. Prieto, and R. Rodríguez. An exact bounded PML for the Helmholtz equation. *Comptes Rendus Mathematique*, 339(11):803–808, 2004.

[19] Bryan A. Biegel. Wigner function simulation of intrinsic oscillations, hysteresis, and bistability in resonant tunneling structures. *Proc. SPIE*, 3277:159–169, 1998.

[20] V. Bonnaillie-Noël, A. Faraj, and F. Nier. Simulation of resonant tunneling heterostructures: numerical comparison of a complete Schrödinger-Poisson system and a reduced nonlinear model. *J. Comput. Electr.*, 8:11–18, 2009.

[21] E. Brown, J. Söderström, C. Parker, L. Mahoney, K. Molvar, and T. McGill. Oscillations up to 712 GHz in InAs/AlSb resonant-tunneling diodes. *Appl. Phys. Lett.*, 58:2291–2293, 1991.

[22] L. Burgnies, O. Vanbésien, and D. Lippens. An analysis of wave patterns in multiport quantum waveguide structures. *J. Phys. D: Appl. Phys.*, 32:706–712, 1999.

[23] R. M. Caplan and R. Carretero-González. Numerical stability of explicit Runge-Kutta finite-difference schemes for the nonlinear Schrödinger equation. *Applied Numerical Mathematics*, 71:24–40, 2013.

[24] C. Cheng, J.-H. Lee, K. H. Lim, H. Z. Massoud, and Q.-H. Liu. 3D quantum transport solver based on perfectly matched layer and spectral element methods for the simulation of semiconductor nanodevices. *J. Comput. Phys.*, 227:455–471, 2007.

[25] W. Chew and W. Weedon. A 3D perfectly matched medium from modified Maxwell's equations with stretched coordinates. *Microwave and Optical Technology Lett.*, 7:599–604, 1994.

[26] S. Datta. A simple kinetic equation for steady-state quantum transport. *J. Phys.: Condens. Matter*, 2:8023–8052, 1990.

[27] S. Datta. Nanoscale device modeling: the Green's function method. *Superlattices and Microstructures*, 28:253–278, 2000.

[28] John H. Davies. *The Physics of Low-dimensional Semiconductors: An Introduction.* Cambridge University Press, 1998.

[29] W. Demtröder. *Experimentalphysik 3: Atome, Moleküle und Festkörper.* Experimentalphysik / Wolfgang Demtröder. Springer, 2005.

[30] P. Dollfus, D. Querlioz, J. Saint-Martin, V.-N. Do, and A. Bournel. Wigner monte carlo approach to quantum transport in nanodevices. In *Simulation of Semiconductor Processes and Devices, 2008. SISPAD 2008. International Conference on*, pages 277–280, 2008.

[31] M. Ehrhardt and A. Arnold. Discrete transparent boundary conditions for the Schrödinger equation. *Riv. Mat. Univ. Parma*, 6:57–108, 2001.

[32] M. V. Fischetti. Theory of electron transport in small semiconductor devices using the Pauli master equation. *J. Appl. Phys.*, 83:270–291, 1998.

[33] W. Frensley. Effect of inelastic processes on the self-consistent potential in the resonant-tunneling diode. *Solid-State Electronics*, 32:1235–1239, 1989.

[34] Matteo Frigo and Steven G. Johnson. The design and implementation of FFTW3. *Proceedings of the IEEE*, 93(2):216–231, 2005. Special issue on "Program Generation, Optimization, and Platform Adaptation".

[35] C. Gardner. The quantum hydrodynamic model for semiconductor devices. *SIAM J. Appl. Math.*, 54:409–427, 1994.

[36] J.-P. Gazeau. *Coherent States in Quantum Physics.* Wiley, 2009.

[37] J.-Y. Ge and J. Zhang. Use of negative complex potential as absorbing potential. *J. Chem Phys.*, 108:1429–1433, 1998.

[38] Gaël Guennebaud, Benoît Jacob, et al. Eigen v3. `http://eigen.tuxfamily.org`, 2010.

[39] H. Gummel. A self-consistent iterative scheme for one-dimensional steady state transistor calculations. *IEEE Trans. Electron Dev.*, 11:455–465, 1964.

[40] H. Han, D. Yin, and Z. Huang. Numerical solutions of Schrödinger equations in $\mathbb{R}^3$. *Numer. Meth. Part. Diff. Eqs.*, 23:511–533, 2007.

[41] E. K. Heller and F. C. Jain. Simulation of one-dimensional ring quantum interference transistors using the time-dependent finite-difference beam propagation method. *Journal of Applied Physics*, 87:8080–8087, 2000.

[42] X. Hu, S.-Q. Tang, and M. Leroux. Stationary and transient simulations for a one-dimensional resonant tunneling diode. *Commun. Comput. Phys.*, 4:1034–1050, 2008.

[43] A. N. Hussain and G. Roberts. Procedure for absorbing time-dependent wave functions at low kinetic energies and large bandwidths. *Phys. Rev. A*, 63:012703, 2000.

[44] T. Jahnke and C. Lubich. Error bounds for exponential operator splittings. *BIT*, 40:735–744, 2000.

[45] Fredrik Johansson et al. mpmath: a Python library for arbitrary-precision floating-point arithmetic (version 0.14). `http://code.google.com/p/mpmath/`, February 2010.

[46] Eric Jones, Travis Oliphant, Pearu Peterson, et al. SciPy: Open source scientific tools for Python. `http://www.scipy.org/`, 2001–.

[47] A. Jüngel, D. Matthes, and J.-P. Milišič. Derivation of new quantum hydrodynamic equations using entropy minimization. *SIAM J. Appl. Math.*, 67:46–68, 2006.

[48] A. Jüngel and J.-F. Mennemann. Time-dependent simulations of quantum waveguides using a time-splitting spectral method. *Math. Comput. Simul.*, 81:883–898, 2010.

[49] A. Khan, P. K. Mahapatra, and C. L. Roy. Lifetime of resonant tunnelling states in multibarrier systems. *Physics Letters A*, 249:512–516, 1998.

[50] Gerhard Klimeck, Roger Lake, R. Chris Bowen, William R. Frensley, and Ted S. Moise. Quantum device simulation with a generalized tunneling formula. *Applied Physics Letters*, 67(17):2539–2541, 1995.

[51] N. C. Kluksdahl, A. M. Kriman, D. K. Ferry, and C. Ringhofer. Self-consistent study of the resonant-tunneling diode. *Phys. Rev. B*, 39:7720–7735, 1989.

[52] Nikhil M. Kriplani, Stephen Bowyer, Jennifer Huckaby, and Michael B. Steer. Modelling of an Esaki tunnel diode in a circuit simulator. *Active and Passive Electronic Components*, 2011.

[53] C. Leforestier and R. Wyatt. Optical potential for laser induced dissociation. *J. Chem. Phys.*, 78:2334–2344, 1983.

[54] C. Lent and D. Kirkner. The quantum transmitting boundary method. *J. Appl. Phys*, 67:6353–6359, 1990.

[55] W.-R. Liou, J.-C. Lin, and M.-L. Yeh. Simulation and analysis of a high-frequency resonant tunneling diode oscillator. *Solid-State Electr.*, 39:833–839, 1996.

[56] S. Mahapatra and N. Sathyamurthy. Negative imaginary potentials in time-dependent molecular scattering. *J. Chem. Soc., Faraday Trans.*, 93:773–779, 1997.

[57] J.-F. Mennemann, A. Jüngel, and H. Kosina. Transient Schrödinger-Poisson simulations of a high-frequency resonant tunneling diode oscillator. *J. Comput. Phys.*, 239:187–205, 2013.

[58] N. Muramatsu, H. Okazaki, and T. Waho. A novel oscillation circuit using a resonant-tunneling diode. *IEEE Intern. Symposium Circuits Sys.*, 3:2341–2344, 2005.

[59] M. Nedjalkov, D. Vasileska, E. Atanassov, and V. Palankovski. Ultrafast Wigner transport in quantum wires. *J. Comput. Electron.*, 6:235–238, 2007.

[60] D. Neuhauser and M. Baer. The time-dependent Schrödinger equation: Application of absorbing boundary conditions. *J. Chem. Phys.*, 90:4351–4355, 1989.

[61] A. Nissen and G. Kreiss. An optimized perfectly matched layer for the Schrödinger equation. *Commun. Comput. Phys.*, 9:147–179, 2011.

[62] Persistence of Vision Pty. Ltd. (2004). Persistence of vision raytracer (version 3.6). `http://www.povray.org/download/`.

[63] Gang Pang, Lei Bian, and Shaoqiang Tang. Almost exact boundary condition for one-dimensional Schrödinger equations. *Phys. Rev. E*, 86:066709, Dec 2012.

[64] D. Pathria and J. Morris. Pseudo-spectral solution of nonlinear Schrödinger equations. *J. Comput. Phys.*, 87:108–125, 1990.

[65] M. Paulsson. Non equilibrium Green's functions for dummies: Introduction to the one particle NEGF equations. *Preprint arXiv:cond-mat/0210519*, October 2002.

[66] O. Pinaud. Transient simulations of a resonant tunneling diode. *J. Appl. Phys.*, 92:1987–1994, 2002.

[67] E. Polizzi and N. Ben Abdallah. Subband decomposition approach for the simulation of quantum electron transport in nanostructures. *J. Comput. Phys.*, 202:150–180, 2005.

[68] M. Schulte and A. Arnold. Discrete transparent boundary conditions for the Schrödinger equation – a compact higher order scheme. *Kinetic and Related Models*, 1:101–125, 2008.

[69] L. Shifren, C. Ringhofer, and D.K. Ferry. A Wigner function-based quantum ensemble Monte Carlo study of a resonant tunneling diode. *Electron Devices, IEEE Transactions on*, 50(3):769–773, 2003.

[70] M. Shin. Three-dimensional quantum simulations of multigate nanowire field effect transistors. *Math. Comput. Simul.*, 79:1060–1070, 2008.

[71] I. Singer and E. Turkel. A perfectly matched layer for the Helmholtz equation in a semi-infinite strip. *J. Comput. Phys.*, 201:439–465, 2004.

[72] A. Soffer and C. Stucchio. Open boundaries for the nonlinear Schrödinger equation. *J. Comput. Phys.*, 225:1218–1232, 2007.

[73] Fernando Sols, M. Macucci, U. Ravaioli, and Karl Hess. Theory for a quantum modulated transistor. *Journal of Applied Physics*, 66(8):3892–3906, 1989.

[74] A. Svizhenko, M. P. Anantram, T. R. Govindan, B. Biegel, and R. Venugopal. Two-dimensional quantum mechanical modeling of nanotransistors. *J. Appl. Phys.*, 91:2343–2354, 2002.

[75] M. A. Talebian and W. Pötz. Open boundary conditions for a time-dependent analysis of the resonant tunneling structure. *Appl. Phys. Lett.*, 69:1148–1150, 1996.

[76] H. Tsuchiya, M. Ogawa, and T. Miyoshi. Wigner function formulation of quantum transport in electron waveguides and its application. *Japan. J. Appl. Phys.*, 30:3853–3858, 1991.

[77] N. Tsukada, A. D. Wieck, and K. Ploog. Proposal of novel electron wave coupled devices. *Applied Physics Letters*, 56(25):2527–2529, 1990.

[78] R. Venugopal, Z. Ran, S. Datta, M. Lundstrom, and D. Jovanovic. Simulating quantum transport in nanoscale transistors: Real versus mode-space approaches. *J. Appl. Phys.*, 92:3730–3739, 2002.

[79] P. Vogel and T. Kubis. The non-equilibrium Green's function method: an introduction. *J. Comput. Electron.*, 9:237–242, 2010.

[80] C. Zheng. A perfectly matched layer approach to the nonlinear Schrödinger wave equations. *J. Comput. Phys.*, 227:537–556, 2007.

Acknowledgements

I would like to express my gratitude to all those who helped me writing this thesis. First of all, I want to thank Professor Ansgar Jüngel for his supervision, professional support and the pleasant working atmosphere. I would also like to thank Professor Hans Kosina for several fruitful discussions which greatly improved the simulations presented in Chapter 3. Many thanks go to my colleagues and friends for answering questions, providing feedback and serving cakes. Furthermore, I would like to thank the Vienna University of Technology and the Austrian Science Fund FWF for financing the projects I was working on. Special thanks go to my family and especially to my parents Ulrike and Karl for their constant support through the years. Without them, this thesis would not have been possible.

Curriculum vitae

Personal information

Name	Jan-Frederik Mennemann
Address	Obermüllnerstr. 2c, 1020 Vienna, Austria
Date of birth	August 18th, 1980
Place of birth	Wiesbaden, Germany
Parents	Ulrike and Karl Mennemann

Education

since 11/2008	Project assistant and PhD-student, '*Graduate school on partial differential equations in technical systems*', Institute for Analysis and Scientific Computing, Vienna University of Technology, Austria
07/2008	Diploma in mathematics, *'with distinction'*
04/2002 – 07-2008	Studies of mathematics with minor subject physics and emphasis on computer science, Johannes Gutenberg Universität Mainz, Germany
05/2004	Intermediate diploma in mathematics, '*very good'*
10/2003	Intermediate examination in physics, '*very good'*
10/2001 – 03/2002	Studies of physics, Johannes Gutenberg Universität Mainz, Germany
06/2000	Abitur, Gesamtschule Obere Aar, Taunusstein, Germany

Civilian service

10/2000 – 05/2001	Caritas-Sozialstation, Taunusstein, Germany

Publications

1 J.-F. Mennemann, A. Jüngel, and H. Kosina. *Transient Schrödinger-Poisson simulations of a high-frequency resonant tunneling diode oscillator*. J. Comput. Phys., Vol. 239, p. 187–205, 2013

2 A. Jüngel and J.-F. Mennemann. *Time-dependent simulations of quantum waveguides using a time-splitting spectral method.* Math. Comput. Simul., Vol. 81, p. 883–898, 2010

Talks

1 *Transient simulations of a resonant tunneling diode with applications to a high frequency oscillator*, The 17th European Conference on Mathematics for Industry 2012, Lund, Sweden, July 23-27, 2012

2 *Numerical simulations of the time-dependent Schrödinger equation with open boundary conditions*, The 16th European Conference on Mathematics for Industry July 26-30, 2010 Wuppertal, Germany

3 *Nanoscale semiconductor device simulations: recent progress and open problems*, Workshop CompMat'09, Stadtschlaining, Austria, October 01-02, 2009

Teaching

Spring 2012	Teaching assistant *Konversatorium zur Mathematik für Technische Physik*
Spring 2004, 2006	Teaching assistant *Mathematischer Vorkurs für Naturwissenschaftler*

Programming languages

Python, Matlab, C/C++, Java, HTML/CSS, Latex/Asymptote, Povray

Interests

Computational physics, visualization, free software, piano/improvisation